

Laser generated magneto-plasmonic Fe-Au Nanoparticles: Formation, Real Structure and Properties

Inaugural Dissertation

by

Anna (Tymoczko) Piatek

born in Bielawa, Poland

for the degree of
Doctor of Natural Science
- Dr. rer. nat. -

Faculty of Chemistry
University Duisburg-Essen
Germany

Essen, 2020

The present thesis was conducted from March 2016 to April 2020 in the research group of Prof. Dr.-Ing. Stephan Barcikowski at the Institute for Technical Chemistry of the University of Duisburg Essen.

Disputation date: 02.07.2020

Referees: Prof. Dr.-Ing. Stephan Barcikowski, UDE

Prof. Dr. Lorenz Kienle, CAU

Chairman: Prof. Dr. Mathias Ropohl, UDE

DuEPublico

Duisburg-Essen Publications online

UNIVERSITÄT
DUISBURG
ESSEN

Offen im Denken

ub

universitäts
bibliothek

Diese Dissertation wird über DuEPublico, dem Dokumenten- und Publikationsserver der Universität Duisburg-Essen, zur Verfügung gestellt und liegt auch als Print-Version vor.

DOI: 10.17185/duepublico/72682

URN: urn:nbn:de:hbz:464-20200917-085729-3

Alle Rechte vorbehalten.

For My Parents,
Alicji and Marka Tymoczko

“Ora et Labora“ - *Bóg jest Miłością*

Abstract

Gold-iron binary alloy nanoparticles delivering next to magneto-plasmonic properties, surface available for the bio-conjugation. The combination of noble and less expensive metal such as nickel, iron or cobalt, is a widespread tool for a biomedical application like MRI/optical-dual imaging or photothermal therapy. For this purpose, the laser-generated nanoparticle is advantageous due to control over the atomic composition and alloying degree. Nevertheless, properties of such nanomaterials are morphology dependent. Hence, synthesis of various structures such as alloy, Core-Shell, multi core-shell is possible, yet the design over the ultrastructure is still challenging, due to a lack of a fundamental understanding of the synthesis process. A recent intensively studied concept is a mechanistic model, created based on the combination of experimental and theoretical approaches.

In this study, the nanoscale phase diagram for binary AuFe alloy system synthesized via laser ablation was designed based on a combination of experimental data and the thermodynamic calculations. In this regard, various nanoparticle compositions were considered. In the second part, an experimental approach was used, due to the lack of a theoretical model considering the complexity of the liquid environment and kinetically controlled processes. In this regard, the influence of laser parameters, such as target composition, liquid environment and pulse duration on the final ultrastructure was investigated. In this context, ideal conditions regarding the synthesis of iron-gold Core-Shell nanoparticles were determined.

At last based on data gathered from the experimental approach combined with thermodynamic calculations, a mechanistic model for nanoparticle formation mechanism was summarized. Finally, proposed models' transferability was successfully confirmed by another magneto-plasmonic binary system, in this case, AuCo.

Kurzzusammenfassung

Nanopartikel aus einer binären Gold-Eisen-Legierung, die neben den magnetoplasmaischen Eigenschaften auch eine für die Biokonjugation verfügbare Oberfläche bieten. Die Kombination von Edel- und preiswerten Metallen, wie Nickel, Eisen oder Kobalt, sind ein weit verbreitetes Werkzeug für biomedizinische Anwendungen wie MRI/optisch-duale Bildgebung oder photothermische Therapie. Zu diesem Zweck sind lasergenerierte Nanopartikel aufgrund der Kontrolle der atomaren Zusammensetzung und den Legierungsgrad vorteilhaft. Dennoch sind die Eigenschaften solcher Nanomaterialien morphologieabhängig. Daher ist die Synthese verschiedener Strukturen wie Legierung Nanopartikeln, Kern-Schale Nanopartikeln, Multi-Kern-Schale Nanopartikeln möglich. Das Design der Ultrastruktur stellt jedoch immer noch eine Herausforderung dar, da es an einem grundlegenden Verständnis des Syntheseprozesses mangelt. Ein kürzlich intensiv untersuchtes Konzept ist ein mechanistisches Modell, das auf der Kombination von experimentellen und theoretischen Ansätzen beruht.

In dieser Studie wurde ein nanoskaliges Phasendiagramm für ein binäres AuFe-Legierungssystem, das mittels Laserablation synthetisiert wurde. Das Phasendiagramm wurde auf der Grundlage experimenteller Daten mit ergänzenden thermodynamischen Berechnungen erstellt. Dabei wurden verschiedene Nanopartikel-Zusammensetzungen berücksichtigt. Im zweiten Teil wurde ein experimenteller Ansatz verwendet, da es kein theoretisches Modell gibt, das die Komplexität der flüssigen Umgebung oder den Prozess der kinetisch kontrollierten Laserablation in Flüssigkeiten berücksichtigt. In diesem Zusammenhang wurde der Einfluss von Laserparametern, wie Zusammensetzung, Flüssigkeitsumgebung und Pulsdauer auf die endgültige Ultrastruktur untersucht. In diesem Zusammenhang wurden ideale Bedingungen für die Synthese von Eisen-Gold-Kern-Schale-Nanopartikeln ermittelt.

Schließlich wurden für alle gegebenen Ultrastrukturen detaillierte Charakterisierung durchgeführt. Basierend auf den Daten, die aus dem experimentellen Ansatz in Kombination mit thermodynamischen Berechnungen gewonnen wurde, wurde ein Modell für den Mechanismus der Nanopartikelbildung zusammengefasst. Schließlich wurde die Übertragbarkeit der vorgeschlagenen Modelle durch ein weiteres Legierungssystem, in diesem Fall AuCo, erfolgreich bestätigt.

Table of Contents

1. Introduction	1
2. State of Art.....	6
2.1 The AuFe alloy system	6
2.2 Nanoparticles properties	8
2.3 Colloidal Synthesis of alloy nanoparticles	12
2.3.1 Chemical synthesis	12
2.3.2 Laser ablation in liquids	13
2.4 Nanoparticle formation – modeling	18
3. Objectives	21
4. Results and Discussion	24
4.1 Nanoscale phase diagram for AuFe generated via laser ablation in liquids.....	24
4.1.1 Nanoparticle and target composition	24
4.1.2 Nanoparticle ultrastructure	27
4.1.3 How Crystal Structure and Phase Segregation of Au-Fe Alloy Nanoparticles is ruled by Molar Fraction and Size	28
4.1.3.1 Au ₅₀ Fe ₅₀ core-shell ultrastructure verification	34
4.2 Impact of target, pulse duration and liquid environment on the final Au-Fe NPs structure.....	37
4.2.1 High yield one step laser synthesis of core-shell Au-Fe nanoparticles- the influence of pulse length and target structure.....	37
4.2.1.1 Theoretical model for AuFe NPs	53
4.2.2 Ultrastructure, colloidal stability and size distribution of core-shell Au-Fe LAL generated NPs tuned by the liquid environment.....	57
4.3. Characterization of the AuFe ultrastructure	69
4.3.1 Chemical stability of Au-Fe NPs	69
4.3.2 Thermal stability of AuFe NPs	73
4.4 Formation mechanism proposal for AuFe system.	76
4.4.1 High core-shell formation – transferability to AuCo system	82
5. Summary	88
6. Outlook	93
7. Appendix.....	94
7.1 Reference	94
7.2 Supporting information.....	105
7.3 Material and Methods	131
7.3.1 Nanoparticles synthesis and characterization	131

7.3.2 Pulsed laser ablation in liquids (LAL)	131
7.3.3 Single pulse laser ablation.....	132
7.3.4 UV-Vis Spectroscopy (UV-Vis)	133
7.3.5 High-angle annular dark-field scanning transmission electron microscopy (STEM-HAADF) and EDX analysis	133
7.3.6 Selected area diffraction (SEAD).....	135
7.3.7 X-Ray Diffraction (XRD)	135
7.4 Curriculum Vitae	136
7.5 List of Authored and Co-author Publications	138
7.6 Declarations.....	140
7.7 Acknowledgment	143

1. Introduction

The combination of two or more elements in one **alloy**[1] **nanoparticle (NP)**, is beneficial in numerous applications[2, 3] e.g. in sensing devices[4, 5], composite materials[6, 7], catalysts[8-11], solar cells[12], data storage devices[13], biomedical applications[14, 15] and many more[1, 16], where optical, magnetic and electrical properties can be combined. The design of the multifunctional binary alloy nanomaterial is still **limited due to the elusive fundamental understanding of the laser ablation process**. In particular, the full utilization of the properties is hindered by the generation of various ultrastructures. Thus, a combination of experimental and theoretical approaches may represent a new strategy to overcome those problems, by rationalization of the result through a **nanoscale phase-diagram enriched by the nanoparticle formation mechanism model**. Here the experimental exploration of the morphology and phase stability is supported with the thermodynamic calculations. The model has a potential to unravel the understanding of **the nanoparticle formation mechanism** during laser ablation in liquids (LAL). Furthermore, it constitutes a solution for the generation of various morphologies in controllable manner, even for immiscible or partially miscible alloy systems.

One example of a thermodynamically forbidden composition would be AuFe alloy NP, which is not accessible by conventional synthesis technique. The successful formation of the bimetallic AuFe alloy NPs was reported in the literature with LAL method, synthesized even from a fully separated layered target configuration[17]. Laser ablation in liquids is a simple but sophisticated method, which allows the generation of ligand-free electrostatically stabilized NPs. This method was first described in 1993 by Fojtik and Henglein and focused on the generation of the NPs from the bulk target, where no purification is required[18]. For the synthesis, metal /metal oxide/ alloy targets are required, placed in **the liquid of choice** (e.g. in cuvette), where the laser beam is focused on the target surface[10, 19]. To successfully perform the ablation only a few Watt laser power input is necessary yet, the **ablation threshold must be reached or exceeded**[20]. Due to interaction between the laser beam and the surface, where massive power density is focused in a small region, absorption of photons results in ejection of ablated mater (solid fragments, highly excited species, atoms, droplets

cluster, and ions), with the majority of them captured directly within the laser-induced cavitation bubble. Variation of the final product can be adjusted by the exchange of the target (formation of alloys from alloy targets) or liquid (formation of oxide in water from oxidation sensitive metals, reversed core-shell configuration with an oxide shell)[21, 22]. For once, alloy NPs synthesized by LAL can play an important role in catalysis. Not only do they fulfill the requirements for 12 principles of “ **green chemistry**” due to their pure and stable nature[22, 23] but they also allow to drastically reduce the amount of noble metal without sacrificing catalytic performance[24]. These include synthesis of homogenous AuFe nanoalloys with enhanced electrocatalytic properties towards oxygen evolution reaction[24]. The formation of nanoalloys with the content of Fe above the thermodynamic predictions (> 11%), can be formed due to fast kinetics of the nanoparticle formation during LAL[20].

Next to alloy NPs, nanoparticles arranged in a **Fe@Au core-shell (CS) morphology** are highly interesting. Here, a metallic iron core would allow harvesting **higher magnetic spin densities**[25] in contrast to iron oxide predominantly found in the nanoparticles. Furthermore, two additional properties are gained, mainly **surface plasmon resonance** from the gold shell[26, 27] as well as the possibility to functionalize the NPs surface[28, 29]. Systems composed of an iron core and a gold shell were shown to exhibit advanced photocatalytic activity in low-temperature oxidation of carbon monoxide[30], and showed controlled reactivity and magnetic recyclability for a reaction such as reduction of 4-nitrophenol[31] in comparison to pure element NPs. However, more recently, a growing interest was devoted to the biomedical application of AuFe NPs. In particular, nanotechnology is a new step in the direction of making targeted drug delivery[32, 33] and stem cell tracking[34] safer by **facilitation of bioconjugation via thiol-gold chemistry**[35]. Indeed, gold shell not only delivers surface available as a carrier, but also plasmonic properties along with biocompatible protection of an oxidation susceptible iron core, which can find its use e.g. during MRI /optical-dual imaging[36]. The most important factors for application in biomedicine as well as in catalysis are clean NPs. Unfortunately, Fe@Au core-shell nanoparticles are very tedious to produce using **chemical co-precipitation**[26] and **reversed micelle methods**[37] as **contaminations by precursors must be removed in an additional step**[38]. Furthermore, chemically synthesized Fe@Au nanoparticles were shown to be unstable as the iron core oxidizes with time[39].

Finally, considering economic aspects, laser-based synthesis is more cost-efficient than chemical reduction, in case high productivity is reached[40].

Despite the outstanding advantages of **LAL**, CS formation by **LAL is still limited, due to competitive processes**, yielding a second mode of particles with a different morphology namely **solid solution NPs**. Research activities have thus focus on the identifying the conditions during LAL, towards either alloy or CS morphology, which contributes towards particular properties. Hence previous work has identified the amount of Fe content required towards better control of optical and magnetic properties, with possible application in e.g. SERS[41]. By the variation of the **molar fraction in the target control over the final NPs composition was achieved**, yet only in case of Au rich targets (**Au 100 – 80 at. %**) and after the post-synthesis cleaning procedure. **The increase of iron** (up to 50 at %) in the material used for the ablation, inherently exhibits the formation of either alloy or **segregated structures** as reported by Wagener et. al.[42]. Nevertheless, previous experimental studies **were concentrated mostly on Au rich NPs**, with insufficient information about system with higher Fe contents; although an indication of higher phase segregation for NPs with Fe doping at 44% was observed[27, 41, 42]. Moreover, the impact of surrounding media on the final composition was examined, based on layered AuFe film targets[17]. The authors could conclusively prove that not only material in the target but also **liquid affects the mixing grade of formed alloy NPs for Au rich targets**. Moreover, the interaction between ablated species and the liquid environment was suggested as an important factor during NPs formation. This theory was further confirmed by Wagener et al., who showed that the interaction between the liquid environment and the surface of the nanoparticles contributed to the phase segregation and elemental distribution in laser-generated Fe@Au NPs[42]. The Fe@Au core-shell morphology was predominant in acetone, whereas in **water inverse Au core and Fe₃O₄ shell was generated**[42]. Indeed, according to Amendola et al. and Wagener et al. findings, alloy formation is expected for targets with high Au content, whereas for composition > 44% CS was an additional fraction[41, 42]. So far, no conclusive research was performed for target composition with high iron contents. Moreover, the pulse duration impact on CS formation was investigated only for composition Au₅₀Fe₅₀[42]. Nevertheless, to prepare outline nanoscale phase-diagram, next to experimental data, the thermodynamic model should be considered.

The interplay between **non-equilibrium and high-temperature conditions** as well as **fast quenching rate** during the ablation process and the thermodynamic preferences is far from trivial making the NPs ultrastructure/size control challenging[43]. A significant issue is **the investigation of kinetic or thermodynamic contribution during LAL**. For miscible elements, such as AuAg, monophasic alloy NPs with composition resembling alloy target can be achieved[44, 45]. Yet, large deviations were reported for noble metals doped with elements such as Cu or Fe. Chattopadhyay and Malviya proposed Cu-Ag molar ratio – morphology/size dependency model, where with means of Gibbs free energy of the elements and the wettability of the alloy either phase segregation core-shell or alloy formation can be predicted[46]. Here, Cu rich small NPs minimize their surface free energy by forming core-shell NPs, whereas bigger sizes with lower Cu content formed biphasic or single phase[46]. All things considered, this study suggests the thermodynamically controlled formation of AgCu NPs, indicating the slow formation of the NPs despite the fast nucleation process during LAL. Contrarily to this prediction, systems **with limited miscibility in bulk**, such as AuFe[47], PtRu[48], AuPt[49], and AgPt[50] form **metastable alloy NPs**, indicating a kinetically controlled process caused by fast cooling. Where by increasing the free surface energy for smaller NPs diameter formation of metastable alloy NPs was made possible[51]. To get a better understanding of kinetic or thermodynamic contribution during LAL, simple thermodynamic model proposed by Chattopadhyay et al.[46] will be employed to AuFe system. Moreover, the fabrication of the mechanistic formation model for iron-gold nanoparticles with the whole range of compositions will be addressed here, which was not reported in the literature so far.

The experimental studies presented in this thesis explore a way for more efficient control over the AuFe LAL-generated NPs. The present work combines experimental and theoretical approaches for the design of nanoscale phase-diagram. In this regard, the formation mechanism for AuFe NPs generated via LAL will be addressed. Until now, most of the studies, are limited with regard to the variability of the NPs design by evaluation of one parameter at the time. The aim of this thesis was to provide a systematic study addressing an entire formation process during LAL with possible morphologies and stability of various phases. In this context, the influence from the target composition, liquid environment, and pulse duration on the CS NPs formation

was clarified. The focus was laid on the investigation of kinetic or thermodynamic contribution during LAL. For this purpose, the thermal and chemical stability of various phases was investigated. The formation mechanism, as well as nanoscale phase-diagram, may contribute towards improved control over ultrastructure of the AuFe alloy generated, with possible transferability towards another binary alloy systems, generated via laser ablation in liquids. Moreover, the data gathered within this work may contribute to the knowledge of fundamental understanding of the laser ablation in liquid.

2. State of Art

In the following chapter alloy nanoparticles properties, synthesis route, as well as formation mechanism during laser ablation in liquids, will be summarized for AuFe binary alloy system.

2.1 The AuFe alloy system

The desire to design multifunctional nanomaterials[3, 7, 16, 52, 53], especially for immiscible or partially miscible alloy nanoparticles has stimulated huge interest for the generation of NPs via laser ablation in liquids[54-56]. Nevertheless, the combination of iron and gold into one single particle is far from trivial. In general, the phase diagram and their thermodynamic information can be helpful towards alloy morphology control. Due to the fact, that the transformation from bulk alloy to nanoalloys is manifested e.g by changes in melting temperature, crystal order, superparamagnetism, surface plasmon resonance, etc[1, 52], a nanophase diagram would contribute towards a better understanding of the nanomaterial at the nanoscale. For this reason, based on the experimental and theoretical approaches, a model of the nanoscale phase-diagram will be proposed in this work. Nevertheless, before the nanoscale system can be summarized, the AuFe bulk phase diagram has to be considered (Figure 1). The transformation occurring for a gold-iron system will be explained with two representative configurations; Au₁₅Fe₈₅ and Au₈₅Fe₁₅. In both cases at higher temperatures (1600°C), both gold and iron are in a liquid state. Au has a lower melting point, therefore it would stay longer in this state (Au 1064°C/ Fe 1538°C). In this regard, at the liquidus line interface, solid iron would be surrounded by gold in a liquid phase. The solidification of the primary phase and peritectic reaction $[(\gamma\text{-Fe}) + \text{liquid} \rightarrow (\text{Au})]$ play important role in the alloying process and occurs for iron-rich materials (with Au 8-43 at. %) at 1173°C. Here, two solid phases are present, with the same FCC structures. The miscibility gap occurs between the temperature of the peritectic reaction and the temperature of eutectoid transformation at 868°C $(\gamma\text{-Fe}) \leftrightarrow (\text{Au}) + (\alpha\text{-Fe})$. Similarly, as for iron-rich, gold-rich configuration Au₈₅Fe₁₅ contains 2 phases, both in FCC configuration.

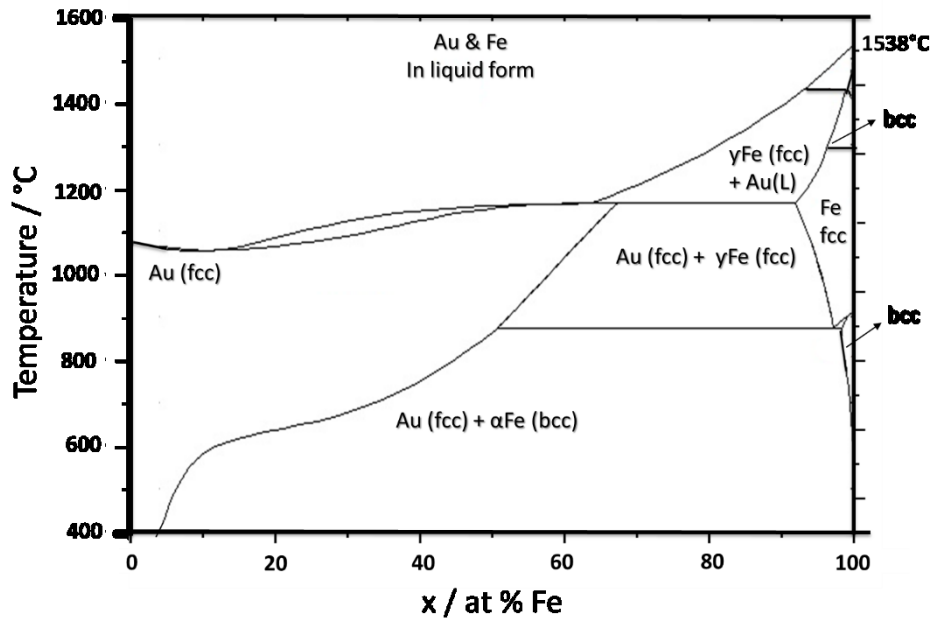


Figure 1: Au-Fe bulk phase-diagram redrawn from ref [115].

Upon further cooling below 600°C, next to FCC gold, FCC iron will transfer into BCC phase. Additionally, the gold-rich FCC phase substituted with Fe will be present. Interestingly, the solubility of iron in gold, as well as gold in iron, will constantly decrease below the eutectoid temperature, which results in the precipitation of α -Fe. It was suggested by Bosco et al., that the competition between precipitation of γ -Fe and α -Fe in the Au matrix occurs constantly[57]. Contrarily to the metastable FCC phase, BCC phase is considered a stable phase[56]. Yet, FCC phase has a lower driving force required for the nucleation due to the same FCC matrix for both Au and Fe[56].

To conclude, based on the bulk phase diagram, iron core (BCC) surrounded by gold shell (FCC) nanoparticle would be expected as the most thermodynamically stable morphology at room temperature[56]. In accordance with the Hume-Rothery Rule[58], the miscibility of Au and Fe defines the system as immiscible because of differences in the lattice parameter (Au 0,4 nm; Fe 0,28 nm) and in the surface energies (Au 1,5 Jm⁻²; Fe 2.4 Jm⁻²)[56]. Therefore, the second rule proposed by Guisbiers et al. can be applied[59], where gold segregates to the surface as its surface energy is smaller than for Fe. Alloy formation is possible only by the application of the kinetically controlled method, allowing the formation of a metastable alloy (FCC Au and FCC iron), as predicted by the miscibility gap.

2.2 Nanoparticles properties

A combination of two or more elements in one alloy was already used by early civilization e.g in ancient Egypt. “Electrum” gold-silver coins were employed by Lydians, due to its low mining and processing requirements[59]. Also, gold-copper “Tumbaga” alloys were used by pre-Columbian civilization mostly in jewelry and decoration field[60]. Nowadays, high interest for nanoalloy remains as the physical and chemical properties can be controlled based on the nanoparticle size, composition, degree of chemical ordering[61], and segregation degree^[46]. Additionally, the surface to volume ratio in comparison to bulk increases drastically allowing new properties to be harvested[62]. The exploitation of Au-Fe or Au-Co nanostructures are particularly interesting due to their physical and chemical properties[32, 37, 63]. This includes a high surface to volume ratio, relevant for catalysis[62], and the possibility to form of multifunctional plasmono-magnetic alloy nanoparticles. Indeed, the gold shell delivers a combination of advantages, surface available for bioconjugation, plasmonic properties but also biocompatible protection of iron/cobalt core against oxidation. Such properties found its use e.g. during MRI /optical-dual imaging[36], photothermal therapy[64], light-induced vapor generation[65], photoacoustic imaging[66] and many more. In the case of Au, plasmonic nanoparticles play a fundamental role in everyday technology. The optical properties are correlated with surface plasmon resonance (SPR)[67], which is formed after dipole is built. In the interaction of incident electromagnetic radiation (light) with a nanoparticle, the electrons in the conduction band of the nanoparticle can be excited to vibration/oscillation. In principal SPR is a collective oscillation of conduction band electrons at the metal interface[68]. This process is schematically proposed in Figure 2. Due to the interaction with the electric field, there is a distortion of the electron cloud relative to the atomic nucleus. The Coulomb interaction provides a restoring force that causes the electron cloud to return to its original position[69, 70].

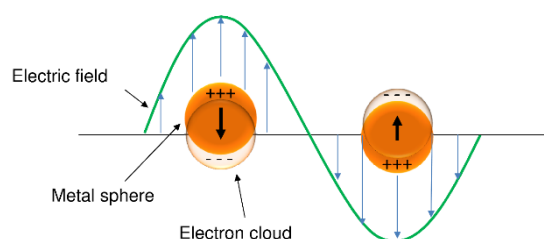


Figure 2: Schematic proposal for Surface Plasmon resonance[71].

By a renewed interaction with the electric field of light, the electron cloud is distorted again. This repetitive process causes an oscillation of the surface electrons, also called plasmons[72]. LSPR (localized surface plasmon resonance) is characteristic for materials such as Au, Ag and Ti[73]. The phenomenon of surface plasmon resonance is responsible for the fact that colloidal gold in the form of nanoparticles no longer appears golden but red[74]. Hence, SPR is strongly dependent on the material, size, structure, surface functionalization[75]. Consequently, Au NPs with a diameter around 90 nm, would appear in purple color instead of red observed for 30 nm Au NPs, this results from the SPR peak shift into the red range[76]. Additionally, increase of the absorbance in the near infrared (IR) range of the spectrum or broadening of the SPR peak, indicating a greater scattering of the particle, meaning that the NPs size increased e.g due to agglomeration or aggregation or deformation[73]. Nanoparticles containing a non-spherical shape also differ in their extinction spectrum[71]. In particular, for a nanorods, with a structure long in one dimension, a second peak corresponding to the longitudinal shape appears in the NIR range in addition to the SPR peak, which is widened and shifted into the red region[77]. Moreover, in the case of alloys, dampening of the SPR can be observed, which was previously reported by Zhang et.al, for gold-iron core-shell structures[78]. Remarkably, the iron gold core-shell system showed more pronounced red-shifted SPR in comparison to iron oxide core surrounded by a gold shell[79]. This difference may arise from the difference in particle size and shell thickness. The optical properties of AuFe NPs were further investigated by Amendola et al. He could conclusively prove that the plasmon band was damped due to the iron atom present in the gold lattice for Au₈₉Fe₁₁ configuration[27]. In fact, an iron particle does not have plasmon resonance in the visible range. Nevertheless, non-linear dependency from the iron doping on the damping was established, which can be correlated to the impact from the iron d state on the relaxation frequency of the conduction electrons[27].

On the other side, magnetic particles with properties, like superparamagnetic, high coactivity and high magnetic susceptibility of iron/cobalt nanoparticles[80, 81] have great importance for e.g data storage[13], biomedical application[82], and catalysis[83]. Contrary to metal oxides, metallic NPs have larger magnetization. Yet, metal NPs are exposed to the oxidation[84] in the air, resulting in the loss or fluctuations of the magnetic properties. By the combination of the biocompatible

gold[85] shell, protection of the magnetism can be achieved. The iron/cobalt is ferromagnetic and has a high magnetic moment density (220 emu/g) due to four unpaired electrons in 3d orbitals[81, 86]. Classification of the magnetism is based on its response to the applied magnetic field and the presence of unpaired electrons[13]. The materials which have no unpaired electrons, and are unaffected by a magnetic field are called diamagnetic. To some extent all materials reveal response towards the magnetic field, such materials are called paramagnets[82]. Paramagnets have one or more unpaired electrons and can be attracted by a magnet. In the case of the paramagnetic state, magnetic moments are random therefore its net magnetic moments cancel each other out and are equal zero[87]. Whereas, ferromagnetic and antiferromagnetic are considered magnetic ordered materials. For ferromagnetic, all atomic magnetic moments are aligned in parallel order, those elements contain permanent magnetic properties, and are not dependent on the magnetic field[87]. High magnetism can be obtained only when nanoparticle contains high crystallinity and core-shell phase[78]. Interestingly for NPs with a diameter below 20 nm, due to the limited size of the domain, superparamagnetic behavior is observed[88]. Superparamagnetism occurs in small ferromagnetic or ferromagnetic NPs. Commonly, Ferro- and ferri- magnetic NPs can undergo their transition to a paramagnetic state above Curie temperature, whereas superparamagnetic transition occurs below this temperature (called blocking temperature)[87]. Moreover, superparamagnetic NPs are single domain. The magnetization in superparamagnetic NPs undergoes constant fluctuations (oscillation), which is thermally driven. Each oscillation has various periods to complete, which is called Neel relaxation time[89]. Such fluctuation is possible for the small crystal sizes, as then the thermal energy kT (where k is Boltzmann's constant and T is the absolute temperature), would be sufficient to cause the changes of the magnetization direction. Magnetic behavior is only present under the application of the magnetic field[86]. Once the magnetic field is eliminated, NPs lose their magnetism at the temperature above the blocking temperature[90]. This enables the NPs to avoid the aggregation and lead to better colloidal stability[91].

Several groups reported the synthesis of magnetic core encapsulated with gold shell[31, 92], with their surface been functionalized with various drugs and molecules towards biomedical application[93, 94]. Magnetic properties of the NPs are dependent on the core size and ultrastructure (single and multicore), chemical composition (oxidation

degree), whereas plasmonic properties are mainly defined by the size and the shape[79]. High magnetism reported by Zhang et al. for iron-gold core-shell NPs, showed its dependency from the crystal phase and particle interface[78]. Mass magnetization per iron content of 210 emu/g was detected, corresponding to 96% of the value reported for the bulk iron (220 emu/g)[78]. These results can be contributed to the highly crystalline iron core. Additionally, magnetic measurements performed by Wagener et al. confirmed, magnetic properties of Au₅₀Fe₅₀ CS NPs with the magnetization of only 10.3 emu/g[42]. Nevertheless, the presence of coexisting magneto-plasmonic properties in gold shell surrounding iron core was proved. The complexity of adjustment of the plasmonic-magnetic properties will be described with a schematic model shown in Figure 3. By the alternation of the ultrastructure either in the iron core – gold satellite (A.) or by iron core – gold shell (B.) configuration with spherical and non-spherical shape (C.), various properties may be more pronounced[79].

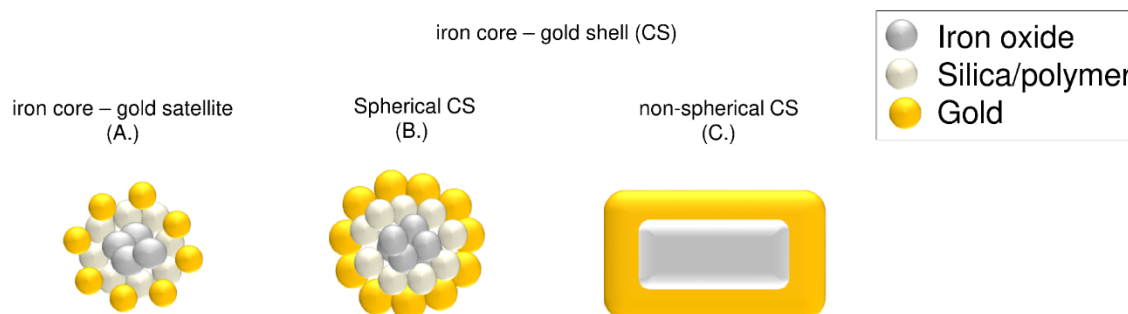


Figure 3: Schematic model of possible ultrastructure of gold-iron system with the iron core, surrounded by gold in form of satellites (A.), and two representative core-shell morphologies with spherical and non-spherical shape, redraw from ref [62]. All proposed nanoparticles were synthesized chemically as described elsewhere[79].

For example, by the ultrastructure A, higher magnetization is present with a high gold specific area, furthermore, functionalization of uncovered Fe is possible. Whereas, ultrastructure B, provides good colloidal stability as well as biocompatibility of the NPs in aqueous media, yet lowest magnetization. Moreover, different optical properties may occur in dependency from the NPs shape (spherical or nonspherical) e.g. ultrastructure C. Even though magnetism decrease can be observed, the iron core is inert from the oxidation, which may alter the magnetic properties of unprotected iron[79].

To summarize the most optimal ultrastructure would be an iron core with gold shell, to harvest plasmonic and magnetic properties, with surface available for the functionalization.

2.3 Colloidal Synthesis of alloy nanoparticles

Synthesis of the colloidal metal nanoparticles can occur via chemical synthesis with help of atomic precursors e.g from the reduction of metal salts (bottom-up approach) or by breaking down the bulk material (top-down) via milling or combination of both e.g via laser ablation (top-down and bottom-up)[20]. The art of the synthesis may determine AuFe NPs ultrastructure and consequently, it may influence their properties. Thus, the following sub-sections give an overview of the following methods, with a focus on their advantages and disadvantages, pointing out the parameters, which may affect the AuFe morphology.

2.3.1 Chemical synthesis

The first reported gold colloid was prepared by M. Faraday in 1857, who synthesized Au NPs by treating aqueous HAuCl_4 with phosphorus dissolved in CS_2 in a two-phase system[95]. Furthermore, Turkevich et al. discovered in 1951 a method to synthesize monodispersed spherical gold NPs in the aqueous phase by reducing chloroauric acid with trisodium citrate[96]. In his procedure citrate anions are used both for reduction as well as stabilization purposes. The synthesis of monodisperse alloy NPs is more challenging. During chemical synthesis, additional stabilizing agents are required to control the NPs growth as well as hinder the agglomeration process[39]. The size, shape, and composition of chemically synthesized NPs are the most important aspects of the solution based colloid synthesis as they are a key feature for most NPs application[94]. During chemical synthesis, generally few consecutive steps such as nucleation, controlled or uncontrolled growth and precipitation of saturated particles are required[97]. The biggest challenge is to stop the reaction at the most convenient time. For example, injection of the salt at the wrong time may lead to polydispersed size distribution[98]. In the case of Au-Fe synthesis, one example would be the reduction of Au salt and decomposition of Fe where sequential ion implantation of iron in gold nanoparticle embedded in a silica matrix occurs[99]. To overcome the

difference in the redox potential of iron and gold, this procedure is performed in two steps. Therefore, in the first step, the iron salt (a mixture of Fe^{3+} and Fe^{2+}) is first reduced with an excess NaBH_4 solution, generating a high yield precursor iron complex. In the second step, gold salt is mixed with the Fe precursor and capping ligands and reduced with NaBH_4 , generating ligand stable Au-Fe NPs[99]. Simultaneous co-precipitation of noble and transition metal precursors is, however, challenging due to the difference in the redox potentials. A second common method for Au-Fe particle synthesis is the reverse micelle method. Where the inner core of the particle act as a nanoreactor and the growth can be controlled by water molecules inside the hydrophilic core. The aqueous core of reverse micelle leads to homogenous nucleation, during which the micellar diffusion would control the particle growth[39]. Gold iron core-shell nanoparticles are very tedious to produce using chemical co-precipitation and reversed micelle methods as contaminations by precursors have to be removed in an additional step. Furthermore, chemically-synthesized Fe@Au nanoparticles were shown to be unstable as the iron core oxidizes with time.

2.3.2 Laser ablation in liquids

Well established laser ablation in a liquid technique has a huge advantage over other methods as it excludes the use of toxic species or by-products adsorbing on the nanoparticle surface[100]. Nanoparticles, which are covered with ligands are mostly undesired for application in e.g heterogeneous catalysis as the adsorption efficiency and catalytic activity is reduced, or biomedical application, as the ligands are blocking the available spots for drugs, protein, etc binding. By using the laser ablation method, we can optimize the size[100] and the composition[22] of the generated nanoparticles for various materials by e.g changing the target, laser parameter and/or the liquid environment[20, 21, 101]. In Figure 4, the principle of laser ablation is explained in a schematic way. During laser ablation in the chosen liquid incident laser pulse penetrates the surface of the starting bulk material (metal, metal oxide, ceramics, semiconductors)[102]. The interaction of a laser beam with bulk target surface results in the absorption of photons, where massive power density is focused in a small region(Figure 3 a)[20]. The electrons of the ablated target absorb photons from the laser beams. The absorption process is material and pulse duration dependent, which

may lead to different ablation mechanism[22]. In the case of short ns pulse, main interactions are based on the thermal processes; and are as follow; vaporization, boiling and melting[103]. Here, the rapid heating to the critical temperature of the solid target leads to detachment of the ablated matter by explosive boiling mechanism[104]. On the other side, short pulse duration (ps and fs) undergo photoionization, in which material is ablated in a similar range to the electron-lattice thermalization speed[104]. Plasma plume is formed as a result of the ionization of the matter within the ablation process (Figure 3 b)[22].

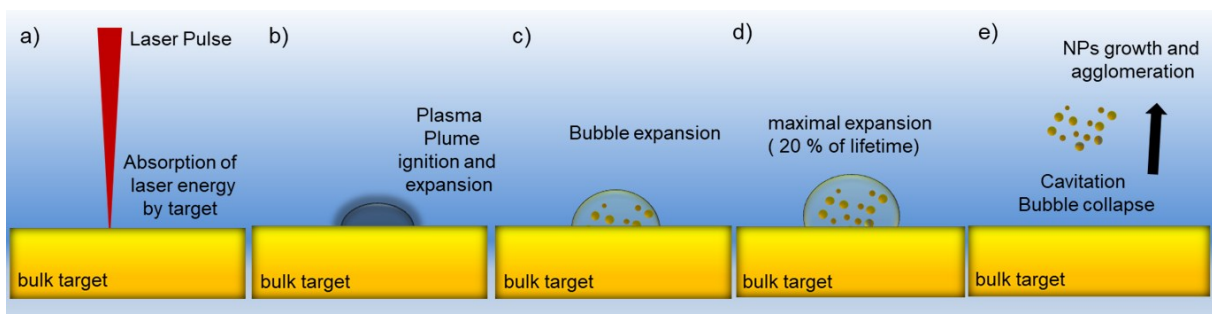


Figure 4: Schematic model illustrating the fundamental process during laser ablation in liquids, with a) initial phase in which laser is absorbed by the bulk target, b) followed by the plasma plume ignition and expansion. The transfer from plasma plume occurs through vaporization of liquid in contact with hot plasma c) The expansion of the cavitation bubble occurs until it reaches its maximum at 20 % of a lifetime, followed by shrinking and collapse resulting in the release of particle into the liquid. Schematic representation with key points during laser ablation redrawn from ref [106].

The liquid pushes laser-induced plasma into a thermodynamic state of higher temperature, pressure and higher density (about 10^{20} cm^{-3} depending on the laser pulse energy[105]). The temperature of the plasma can reach up to thousands of kelvins, whereas the pressure hundreds of pascals[106]. This may favor the formation of metastable phases, which are in high temperature, a high-pressure region on their thermodynamic equilibrium phase diagram, due to fast cooling rates[27]. The lifetime of the plasma can be increased based on the laser parameters (e.g by increasing the laser energy)[107] and surrounding liquid (e.g by addition of salt)[108], generally, the duration of the plasma lies between tens of ns to few μs [109] for each laser pulse. Sakka et al., as well as Lam et al., indicated that the chemical reactions between the species inside the plasma last for several μs [109, 110]. However, a detailed study from Tamura et al. has shown, that plasma and cavitation bubble coexist in the early stage, indicating that the ablated species such as atoms, clusters, and ions most likely interact with the liquid[111]. The transfer from the plasma to the cavitation bubble occurs via the vaporization of liquid in contact with hot plasma plume, and it is dependent on the

pulse energy (Figure 3 c). In the initial cavitation bubble stage, embryonic particles grow by attracting atoms, clusters, and droplets, however, this process is diffusion-limited[112]. Furthermore, clusters can be formed by coalescence of individual growing particles[19, 113]. Nanoparticles may grow after LAL synthesis even up to several days[114]. Expansion of the cavitation bubble occurs until it reaches its maximal height, at around 20% lifetime, followed by hemispherical shrinking until its collapse with possible multi-rebound, where NPs are released into the surrounding liquid or redeposited on the target (Figure 3 d)[115, 116]. Furthermore, the cavitation bubble collapse (Figure 3 e) may lead to the mechanical ablation of the target, leading to the formation of additional NPs[107]. Dynamics of the cavitation bubble and its role during NPs formation was investigated by Plech et al. with means of X-ray small-angle scattering analysis[117], where the bimodal formation of smaller (<10 nm) primary and agglomerated bigger (>40 nm) secondary NPs was proposed. Here liquid-solid interface was proven to be a critical parameter for bubble motion, where secondary particles along with the solvent molecules are confined within the cavitation bubble, indicating the liquid-particles interaction before the cavitation bubble collapse. Whereas, primary NPs are most likely formed via nucleation and growth and are in direct contact with the surrounding liquid media before bubble collapse[118]. Additionally, plasma heated supercritical water phase, and cold bubble vapor may provide conditions for NPs crystallization[20]. Moreover, bimodality can be attributed to different regimes and corresponding thresholds, where 3 areas within the ablation beam can be distinguished: ablation area with the highest fluence in the center spot, annealing area with the lower fluence regime ring, and finally modification area with the outmost area[119]. Numerous investigations have been conducted regarding size control of LAL generated NPs, as with the size the physical and chemical properties can be modified. Particle size distribution varies depending on many parameters e.g. the material and liquid environment etc. For example, liquid surrounding not only impacts the colloidal stability (steric by addition of polymer or electrostatic stability via e.g adsorbates hydroxyl groups)[120], surface oxidation degree (depending on the redox potential)[121], but also influence crystal growth[42]. Hence, during laser fragmentation in acetonitrile hcp crystal structure was obtained for Ni, contrarily to fcc phase in water, most likely due to the specific heat of the organic liquids[122]. Moreover, liquid properties contribution towards cavitation bubble size, lifetime and

mobility during the ablation[123]. Additionally, control of the liquid thickness and liquid flow to maximize productivity and to avoid temporal and spatial concentration gradients respectively should be considered. Moreover, the size of the particles can be quenched by the addition of the additives. However, not all additives bring benefits, some may lead to an increase in viscosity[124] or due to degradation would lead to contaminations[125]. Higher liquid viscosity and density lead to plasma confinement and shorter lifetime of the cavitation bubble[126]. Viscosity changes the diffusion constant of the particle nuclei and their collision rate to form aggregates and bigger nanoparticles, as described by LSW theory[19]. Some efforts have focused on synthesizing NPs in the various liquid environment, yet constant parameter evaluation is extremely difficult. Hereby, the sophisticated but easy technique of LAL grants not only bare but also ligand modified surface, which contributes to higher colloidal stability and size control. In case a clean NPs surface is required, a small addition of micromolar salt concentration can also improve size quenching drastically and can contribute to a more narrow particle size distribution[127]. Moreover, re-irradiation of colloid causing particle fragmentation[128] or melting[129] may be used as a considerable technique for size control. Without the addition of external quenching additives, bimodality may still be observed. Consequently, additional centrifugation steps are often required to achieve clean size fraction[21].

The obvious aim of understanding the formation mechanism during LAL, emerges as depending on the NPs size and the structure, completely different applications may emerge. In this context, an elucidation of the decisive factors during LAL is particularly crucial. For this purpose review of e.g. bimetallic alloy NPs can contribute comprehensive insights into a mechanistic scenario during the laser ablation process.

Remarkably, stable alloy phases can be generated even for materials, which are immiscible or partially immiscible in bulk[54]. Precisely, alloy degree was shown to be controlled by adjusting the target composition (bulk alloy target or pressed mixture of metal powders)[22]. In this regard, alloys such as; AgPt, AuPt[45], AgCu[46], AuAg[44], AuFe, PtPb[130] and FeMn[131] were successfully synthesized[19, 55]. The alloy formation is facilitated due to an increased ratio between surface energy in regard to total free energy, resulted from the particle size decrease[16, 56]. Identifying the stoichiometry of the synthesized NPs revealed, the value nearly identical with the target used for the ablation[44, 132]. In the case of AgAu, perfect monophasic crystals were

produced, which can be correlated to the fact that these elements have no miscibility gap[44]. Yet, generation of the homogenous alloy is strictly material dependent, which may lead to nonstoichiometric alloy or to other phase segregated structures (core-shell, Janus like morphologies, etc) as shown in Figure 5[55]. Here, material resistance towards oxidation plays a crucial role, and more precisely the redox potential of the ablated material[78].

In addition, the morphology of the alloy nanoparticles' may be affected by the surrounding liquid environment during the early stages of laser ablation. Hence, depending on the target, for example, for the ablation of metal in water, a chemical reaction - oxidation may be more pronounced than e.g. thermodynamic preferences, leading to the formation of an oxide NPs[20, 21].

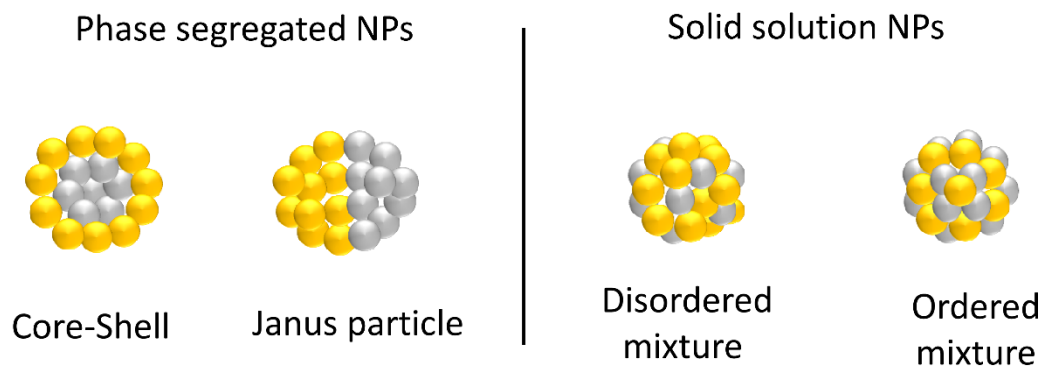


Figure 5: Schematic representation of possible alloy structures[55].

Lam et. al. demonstrated the formation of Al_2O_3 , based on molecular simulation of the nucleation phase, suggesting, that the ablated material interacts with the liquid molecules leading to oxide formation[133]. Additionally, the impact of surrounding media on the final composition was examined based on layered AuFe film targets[17]. The authors could conclusively prove that not only material in the target but also liquid affects the mixing grade of formed alloy NPs for Au rich targets. Moreover, the interaction between ablated species and the liquid environment was suggested as an important factor during NPs formation. This theory was further confirmed by Wagener et al., who showed that the interaction between the liquid environment and the surface of the nanoparticles contributed to the phase segregation and elemental distribution in laser-generated Fe@Au NPs[42]. The Fe@Au core-shell morphology was

predominant in acetone, whereas in water inverse Au core and Fe₃O₄ shell was generated[42]. Indeed, according to Amendola et al. and Wagener et al. findings, alloy formation is expected for targets with high Au content, whereas for composition > 44% CS was an additional fraction[42]. So far, no conclusive research was performed for targets composition with high iron contents. Moreover, the pulse duration impact on CS formation was investigated only for composition Au₅₀Fe₅₀. Nevertheless, to prepare outline nanoscale phase-diagram, next to experimental data, the thermodynamic model has to be included.

2.4 Nanoparticle formation – modeling

Models predicting composition and ultrastructure at certain synthesis conditions are now implemented at the bulk scale. Yet, the information on the temperature-dependent phases transformation is still limited for nanosystems. Classic bulk phase diagram cannot be applied for nanoalloy system, as the number of atoms as well as volume is much smaller[112, 134]. Furthermore, as the surface effects dominate, state function is no longer directly proportional to the number of atoms[104, 135]. Theoretical approach e.g Metropolis Monte Carlo, Density Functional Theory is still limited due to restriction of modeling, which is only suitable for a limited number of atoms. To overcome these challenges, many groups dedicate their work to determine nanoalloy phase diagrams by applying a combination of the experimental and computational approaches. In these studies, 3-dimensional phase diagrams; size, composition, and temperature were considered towards various ultrastructure formation[46]. With the help of thermodynamic calculation, Chattopadhyay et al. described how surface energy for different compositions and sizes would predict segregation or alloyed structure for Ag-Ni & Ag-Cu NPs generated via LAL[46, 136]. Thus, based on the proposed model the morphology transition of the NPs is composition dependent. In the case of AgCu, a transformation occurred from two-phase intraparticle structure to randomly segregated structure and finally to core-shell morphology. Their thermodynamic model was based on the free energy of mixing and the wettability of the alloy phase. As a result 3D model was established in which free surface energy was presented as a function of size and composition. Overall, the particle decrease leads the free energy increase, and therefore NPs with smaller sizes would prone to form core-shell structures. To that

end, the indication of the generation of a particle in thermodynamic equilibrium was proposed for LAL synthesis[46]. Moreover, the proposed model can be applied if certain assumptions can be fulfilled. For example, based on the Hume Rothery rule, if within the system crystal (e.g FCC), atomic radius and electronegativity would be similar solid solution can be predicted[58]. Whereas, in the case of a system with a substantial variation for given parameters, phase segregation should occur. Therefore, thermodynamic model may result in various ultrastructure characteristic for particular material. Next to thermodynamic calculation predicting morphology based on the size and particle composition, a intensive research was focused on the simulation of early stage during the ablation process.

In this context, issues such as bimodality, or alloying degree were addressed. In this regard, Zhigilei et al. offered a potential explanation for ultra and short pulse duration suggesting that the size of the LAL synthesized nanoparticle is explained based on 2 different mechanisms[137]. It is hypothesized, that larger particles form by the ejection of liquid droplets from a superheated metal molten layer, destabilized by Rayleigh Taylor instabilities and impaction from metal droplets from underlying layers. The smaller NPs, on the other hand, are believed to be formed by rapid nucleation of ejected atoms and smaller atom clusters[137]. Despite the formation mechanism is described for short pulse duration, an indication of target and liquid environment impact on the size distribution, and perhaps on the ultrastructure emerges. Moreover, a possible explanation of the ablation mechanism during laser ablation was summarized, in which during long ns pulse duration, melting and vaporization occurs[103] whereas ps short pulse duration can be described as almost instantaneous solid-vapor transition of the atoms of the target[138]. Due to the prolonged time inside the cavitation bubble under heated state (> 5000 K)[139, 140], prolonged cavitation bubble lifetime would arise, due to additional heating of the plasma, caused by the partial overlap of the pulse width and the duration of the existing plasma plume[103, 138]. The extended lifetime of the cavitation bubble by application of larger pulse energy was previously validated by Park et.al[108]. In this regard, the impact from the cooling rates, which in the gas phase is lower than in the liquid phase[108], may impact the final morphology of the particle. Finally, based on, Povarnitsyn et al. simulations, prediction of the origin from particle size can be given. In this context, smaller NPs, are predicted to be

formed in the liquid+gas phase region, whereas the larger are closer to the molten layer region as described by Zhigilei et al[19, 112, 141].

The relevance of the experimental and theoretical approaches was successfully demonstrated to be the most promising tool towards the description of nanoalloy systems. Therefore, in order to generate FeAu NPs with tunable properties via LAL, a combination of Chattopadhyay et al. model as well series of experiments were executed in this work[46]. Mainly, the impact from the liquid surrounding (chain length, heat capacity, and viscosity), availability of the material (Au:Fe ratio), as well as a condition during laser ablation (pulse duration impact), and the target type (bulk vs thin layered target) were evaluated.

3. Objectives

The aim of this work addresses significant shortcomings of the available information during **the nanoparticles formation process** of immiscible or partially miscible **alloy systems during LAL synthesis**. Expansion of the knowledge about the formation mechanism would give an opportunity towards better control of the corresponding ultrastructures, which is one of the current challenges of LAL. At the moment **nanoscale phase diagram for AuFe** system is not available, due to lack of the information of the physical and chemical processes involved during LAL synthesis. To govern such versatility, a combination of the **experimental and theoretical approaches** will be applied and will be summarized in form of the nanoscale phase diagram with a simplified formation mechanism proposal.

In this perspective, the following aspects will be considered:

- i. How does the **target composition** influence the ultrastructure of the nanoalloy NPs? How relevant is the equilibrium miscibility of final NPs formed under non-equilibrium conditions? (Figure 6 a)
- ii. Does the **laser pulse duration** influence the final NPs ultrastructure? How relevant are the conditions during LAL to the formation mechanism? (Figure 6 b)
- iii. How does the **liquid environment** impact the synthesized NP ultrastructure? Can a clear correlation between liquid property and ultrastructure be established? (Figure 6 b)
- iv. Is the NPs formation **kinetically or thermodynamically controlled**? What is the nature of LAL generated NPs, are they **metastable or thermodynamically stable ultrastructures**? (Figure 6 c.)
- v. Finally, **is the proposed model suitable for other** combinations of magneto-plasmonic binary systems with similar properties (**AuCo**)? What are the limitations of this approach? (Figure 6 d.)

Core-shell NPs with an iron core and a gold shell are of particular interest as they allow the combination of magneto-plasmonic properties in one material. To reach full potential of control over the NPs ultrastructure design, nanophase diagram based

on the experimental data enriched by the thermodynamic calculations will be proposed.

Furthermore, the focus would be laid on the systematical variation of the synthesis parameter such as the **liquid environment (alcohols, ketones, and oils), target (alloy, thin layer target), and laser parameters (pulse duration, short ps vs long ns pulse)** towards high **CS NPs yield** (Figure 6 b). The evaluation of the ultrastructure, size, and composition of the NPs, as well as thermal and chemical stability will be performed with the help of HAADF-STEM imaging, Selected area (electron) diffraction (SEAD) patterns, accompanied by Energy Dispersive X-Ray (EDX) spectroscopy. Finally, model describing formation mechanism of the laser-generated AuFe NPs will be addressed. Thus, the transferability of the model to another binary alloy system, in this case, AuCo will be evaluated.

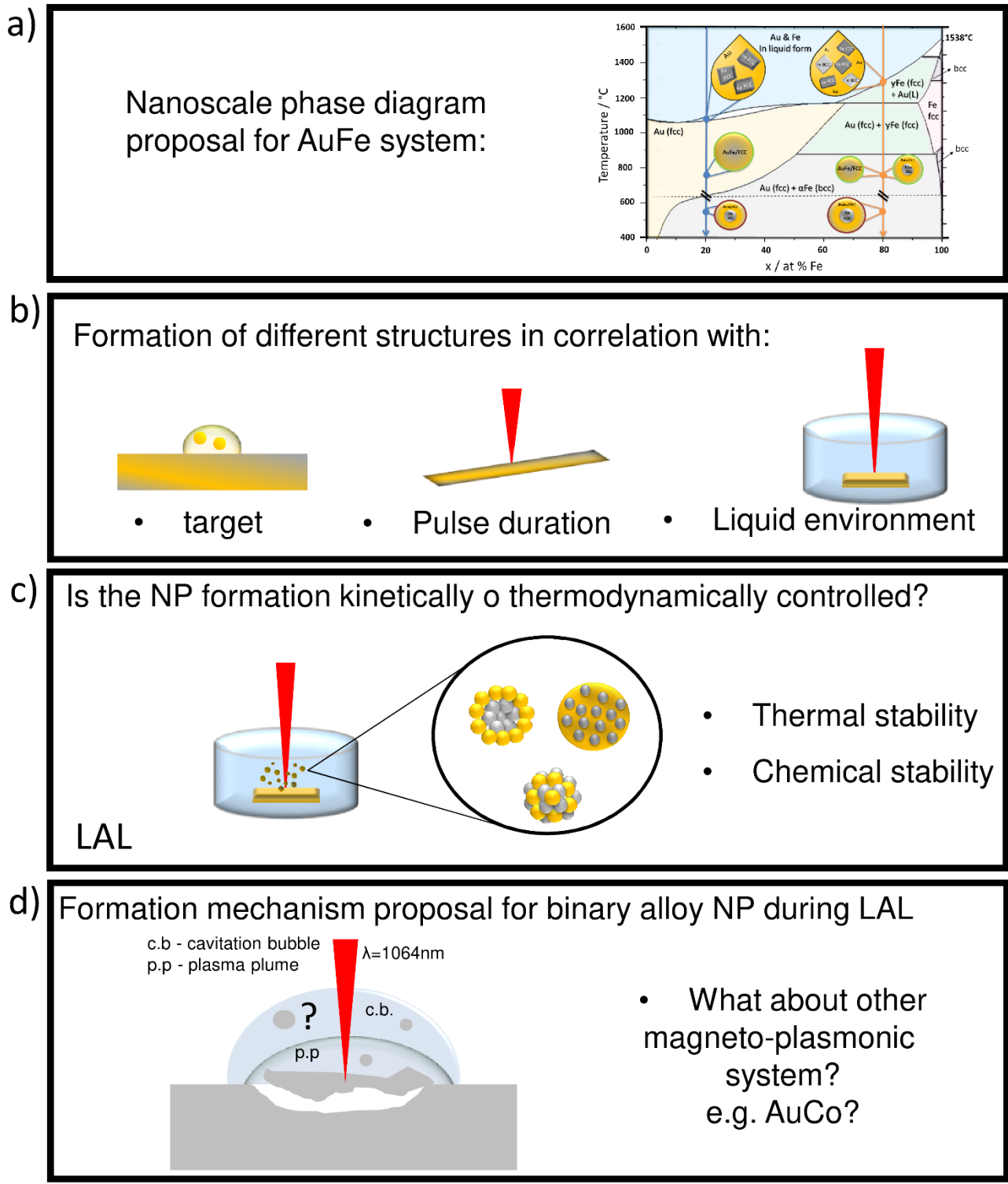


Figure 6: Schematic overview of main objectives in this thesis including a) Proposal of the nanoscale phase diagram for AuFe binary alloy system b) factors affecting high yield of AuFe CS NPs during LAL c) Thermal and chemical stability evaluation of the AuFe NPs d) Proposal of the NPs formation mechanism during LAL, followed by an application of the schematic model towards another binary systems (AuCo).

4. Results and Discussion

The following results and their discussion will be presented in four subchapters. In the first chapter based on the data collected from the experimental and theoretical approach, the proposed nanoscale phase diagram will be given. Here, different compositions of Au:Fe (Fe_{100} , $\text{Au}_5\text{Fe}_{95}$, $\text{Au}_{20}\text{Fe}_{80}$, $\text{Au}_{35}\text{Fe}_{65}$, $\text{Au}_{50}\text{Fe}_{50}$, $\text{Au}_{65}\text{Fe}_{35}$, $\text{Au}_{80}\text{Fe}_{20}$, $\text{Au}_{95}\text{Fe}_5$, Au_{100}) and NPs' diameter between 5 and 50 nm were considered. In the second part, the contribution towards high iron gold core-shell yield during laser ablation in liquids is characterized with regard to layered target (alloy, AuFe/glass, FeAu/glass, and AuFeAuFe/glass), liquid parameter (heat capacity, chain length, and viscosity) and pulse duration (short ps and long ns). This subchapter is enriched by the updated theoretical model, which considers the interface energy as the thermodynamic driving force towards element segregation. Thirdly, the evaluation of the various ultrastructure's thermal and chemical stability is performed. Finally, the fundamental NP formation mechanism of binary AuFe alloy via laser ablation in liquid is summarized. In addition, transferability to another magneto-plasmonic binary system will be evaluated. The results summarized in this dissertation point toward the importance of careful parameter choice during LAL NP synthesis and confirmed successful control of the ultrastructure for both analyzed systems (AuFe and AuCo).

4.1 Nanoscale phase diagram for AuFe generated via laser ablation in liquids

4.1.1 Nanoparticle and target composition

Gold-iron nanoparticles were analyzed by employing EDX analysis in order to obtain a comprehensive impression on their composition. The successful generation of the reproducible composition of the NPs with high colloidal stability is required before the evaluation of the parameter affecting the formation mechanism of AuFe NPs can be performed. To exclude the variation in the composition of the NPs generated via LAL in acetone, EDX analysis of targets used for the ablation and synthesized NPs was

performed. Apart from Au₃₅Fe₆₅, STEM-EDX analysis revealed the same composition of NPs in correlation to the ablated target. The composition of the NPs stayed within with a small error range (below 5 %) as shown in Figure 7 a. Representative STEM pictures for nanoparticles with composition Au₂₀Fe₈₀ and Au₅₀Fe₅₀ are shown in Figure 8b. Huge variation in the composition of Au₃₅Fe₆₅ can be correlated to a high abundance of impurities within the sample, therefore Au₃₅Fe₆₅ and Au₆₅Fe₃₅, were excluded from the study. Based on the observed trend it can be stated that the overall composition of the NPs, independent from its structure, (Figure 7 b and S1) can be controlled by the target elemental ratio. The results are in correlation with previously published reports, in which the composition of the AuFe alloy NPs, was adjusted with the target composition.

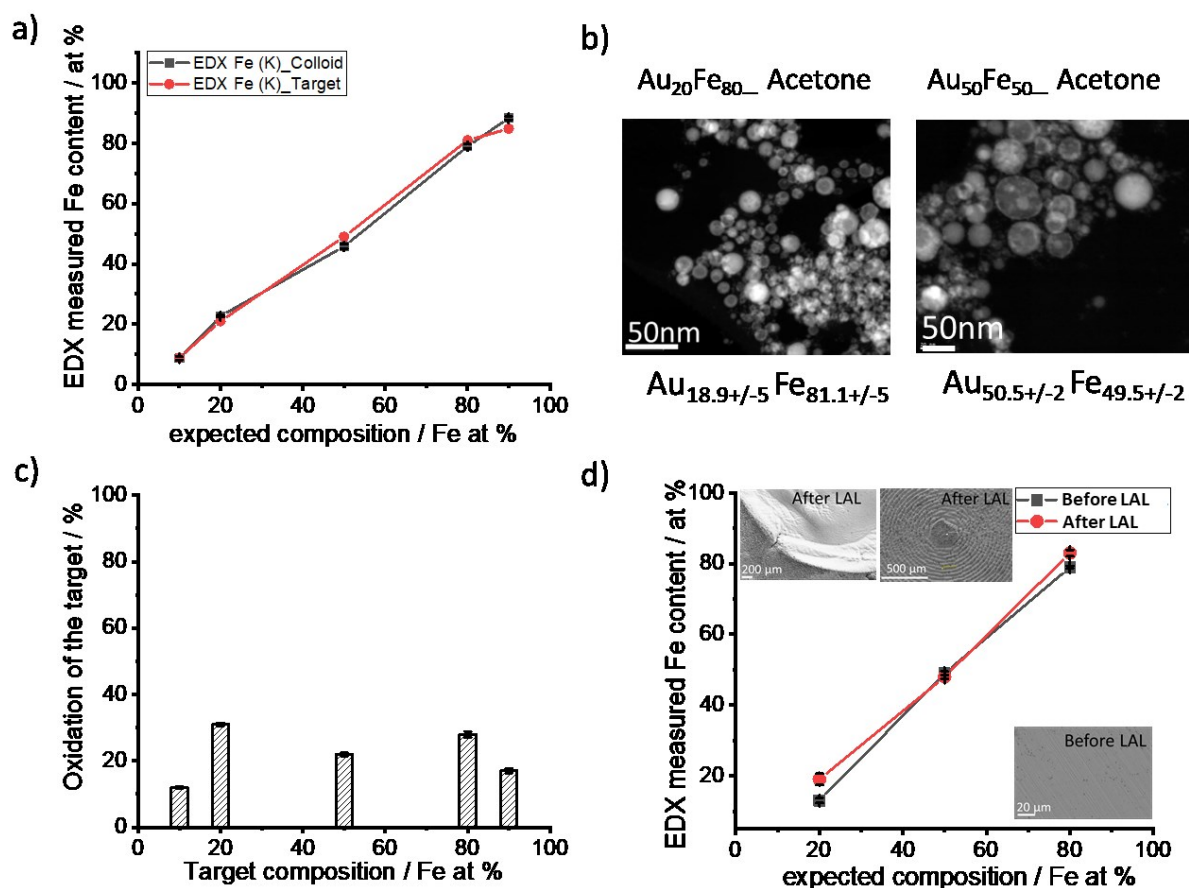


Figure 7: a) EDX evaluation of target and NPs composition b) with STEM images for representative compositions; Au₂₀Fe₈₀ and Au₅₀Fe₅₀ in acetone generated via ns laser (composition is based on EDX analysis presented in Figure S1) c) Oxidation degree in the target used for the ablation measure via EDX analysis d) EDX analysis of the AuFe colloids before and after ablation.

Nevertheless, when considering NPs composition, oxidation has to be taken into account. This assumption is reasonable due to the fact, that iron is highly sensitive to

oxidation, and therefore the formation of the iron oxide layer on the target surface may occur. According to literature, the formation of the oxide NPs is common, especially for iron in the oxidizing environment. Moreover, oxidation of the iron core may lead to NPs with lower magnetization and nonmetallic band structure. Therefore, in order to evaluate if the oxidation of the target would lead to a generation of oxidized NPs, EDX analysis of the NP and the target was applied. For the evaluation of the oxidation degree of the target, 6 representative targets compositions were chosen (with Fe content 10,20,50,80,90 at. %). As has been shown in Figure 7 c, the oxidation degree varies between 10-30 % and does not exceed 30%. Furthermore, to confirm the sufficiency of the ablation method, EDX analysis of representative core-shell NPs was performed, proving that no oxide was detected inside the NP (Figure S2). Nevertheless, the analysis clearly confirmed no oxide within the NP, indicating the preservation of the magnetic properties. Magnetic properties for LAL generated AuFe NPs were previously confirmed by Amendola et al., yet only for Au rich composition. The evaluation of the magnetic properties of iron-rich NPs will be addressed in chapter 4.2.1.

Since the NP composition can be controlled with the composition in the target used for the ablation, the clarification of the composition of the previously ablated target has to be evaluated. To identify, to which extent previously ablated surface may impact the composition of the synthesized NPs, both previously synthesized surface and unused surface were compared. For this purpose 3 representative compositions ($\text{Au}_{20}\text{Fe}_{80}$, $\text{Au}_{50}\text{Fe}_{50}$, $\text{Au}_{80}\text{Fe}_{20}$) were chosen. To this end, the ablation of the previously ablated surface was confirmed to have a negligible impact on the NPs composition. In fact, only 5 % error range in regard to NPs composition was validated as depicted in Figure 7 d between NPs synthesized from the unused surface (before LAL) and surface, which has been already ablated (after LAL). The small deviation may arise from the generation of various NPs ultrastructure, e.g alloy or CS configuration.

Overall, it was demonstrated that NPs composition can be tuned with the composition in the target used for the ablation. Moreover, oxidation of the target has a negligible impact on the NPs composition, the same as the surface previously used for the ablation.

4.1.2 Nanoparticle ultrastructure

During LAL synthesis various ultrastructure can be generated in dependency from the material, it is therefore mandatory to provide a classification of the possible ultrastructure. In this context, four ultrastructures were determined, alloy NPs with disordered solid solution (SS) mixture, core-shell (CS) NPs with iron core and gold shell; jellyfish structures with gold shell, iron core with extra gold core within as well as multi core-shell NPs (MC), with one or many cores (Figure 8 a). To simplify the analysis within this work, jellyfish ultrastructure will be considered as MC NPs. Whereas, CS, MC, and jellyfish are considered as one group of phase segregated (PS) NPs. Regarding, the composition of the respective NPs, EDX analysis was used to determine the element distribution within the NP for two representatives NP, SS, and jellyfish. (Figure 8 b). In this regard, EDX elemental mapping confirmed gold (green) and iron (yellow) regions within the NP. For SS, distinctive mixing can be observed, where both gold (green) and iron (yellow) are distributed within the whole NP, whereas, in case of jellyfish, gold (green) is distributed in the core and the shell, filled in between with iron (yellow).

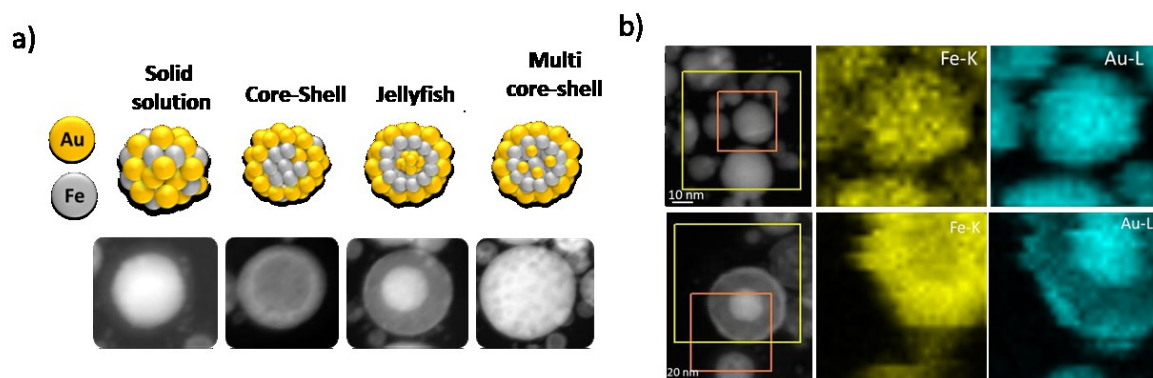


Figure 8: a) Classification of possible ultrastructure for iron-rich NPs generated via LAL in acetone b) EDX mapping of representing NPs; SS and jellyfish (iron –yellow, gold-green color)

A clear distinctive difference between the other structures can be evaluated with the STEM with HAADF detector, in which elemental distribution is investigated by Z-contrast imaging. This evaluation is based on the large difference in the atomic number between iron and gold, characterized in bright (gold) and dark (iron) areas visible in the STEM image. Here, next to SS and jellyfish, further two ultrastructures were determined, CS with a dark iron core and bright gold shell, and MC with gold distributed within the NP, enriched by multi iron cores.

4.1.3 How Crystal Structure and Phase Segregation of Au-Fe Alloy Nanoparticles is ruled by Molar Fraction and Size

Published in: "How Crystal Structure and Phase Segregation of Au-Fe Alloy Nanoparticles is ruled by Molar Fraction and Size" *Nanoscale*, 2018, 10, 16434-16437;

A.Tymoczko, M. Kamp, Oleg Prymak, Christoph Rehbock, Jurij Jakobi, Ulrich Schürmann, Lorenz Kienle and Stephan Barcikowski

The application for Au-Fe nanoalloy is determined by its internal phase structure. Our experimental and theoretical findings explain how the prevalence of either core-shell or solid solution structure is ruled by the target composition and the particle diameter. Furthermore, we found metastable phases not predefined by the bulk phase diagram.

Au-Fe nanomaterials with a defined internal structure[55] are beneficial for numerous possible applications[142]. One example would be in catalysis, where a solid solution structure improves electrocatalytic oxygen evolution[24]. In contrast, a core-shell structure with a metallic iron core and a gold shell could be applicable in biomedicine e.g during MRI/optical dual imaging[143]. Here the metallic iron core would allow to harvest higher magnetic spin densities in contrast to iron oxide predominantly found in nanoparticles (NPs) generated by conventional routes[25]. Additionally, the gold shell could provide surface plasmon resonance as well as the possibility to functionalize the NPs surface via Au-thiol chemistry[28]. As Fe@Au core-shell nanoparticles are very tedious to produce using chemical co-precipitation and reversed micelle methods due to contamination caused by the reactants Laser Ablation in Liquids (LAL)[19] is a viable alternative, producing ligand-free nanoparticles in gram scale[144]. Up to date intensive research in the area of laser-generated gold-rich Au-Fe alloy NPs has been conducted aiming at control over optical and magnetic properties of NPs in correlation with the composition and the surrounding media. Metastable alloys with different mixing grades[145] were synthesized, with clear dependency from the molar ratio[146] and surrounding liquids[42]. Even though the Au-Fe system has been subjected to a number of experimental investigations a deeper understanding of the complex formation mechanism in correlation to target composition and the particle diameter for the whole Au:Fe NPs range is still lacking. Herein we report that in Au-Fe NPs formed by LAL the emergence of a core-shell (CS)

structure is favored for NPs with diameter exceeding 10 nm, Fe molar fractions in the target > 35 % and deviating crystal structure (Au - face-centered cubic (FCC) & Fe – body-centered cubic (BCC)). On the other hand, disordered solid solution (SS) nanoparticles with Fe - FCC structure and number mean diameters < 10 nm always form independently from the Fe content. Au-Fe NPs were synthesized using LAL in acetone (see SI for details) from bulk targets with varied Fe: Au ratios. High-resolution imaging by scanning transmission electron microscopy (TEM) in combination with energy-dispersive X-ray spectroscopy (EDX) line scans revealed the formation of two clearly distinguishable internal phase structures, a disordered solid solution and a *FeAu@AuFe* core-shell structure (Fig. 9, Fig. S 3). In consecutive experiments, we aimed to elucidate to what extent the emergence of these structures was correlated with target composition, particle diameter and the overall crystal structure determined by X-ray powder diffraction (XRD).

Notably, for iron-rich NPs (Fe > 35%), 2 fractions of NPs with below and above 10 nm number mean diameter were detected (Fig. 10a, Fig. S4). Bimodal size distributions were expected as previously shown, based on different ablation mechanism[144]. In contrarily, from Au rich targets (Fe < 35%) particle size distribution with number mean diameter < 10 nm were generated. The overall decrease of larger particles in gold-rich alloy NPs, may be explained by size quenching caused by specific solvent-surface interactions between gold-rich surfaces and acetone[100]. These findings seem to indicate that next to the NPs diameter, target composition has an influence on the ultrastructure of Au-Fe NPs.

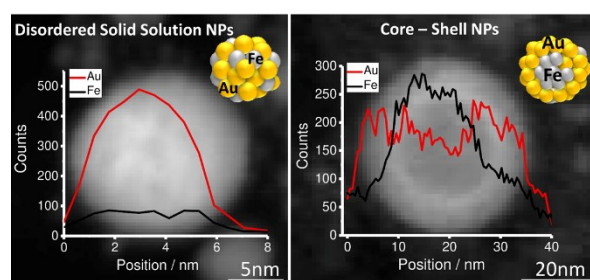


Figure 9: EDX composition analysis for Au-Fe LAL generated NPs in Acetone (disordered Solid solution SS [left] and core-shell CS [right]).

Based on this we deduced a clear particle diameter / Fe % – structure dependency. Our analysis revealed that all particles with a number NPs mean diameter < 10 nm had a disordered solid solution structure, while core-shell was only found for NPs > 10 nm.

This trend was quantified by determining the volume-weighted CS NPs yield (Fig. 10 a). It may be concluded that phase segregation (CS-formation) is only observed for NPs with diameters > 10 nm and Fe molar fractions > 35 %. Additionally, disordered SS forms independently of the target composition. The results clearly show that NPs with diameters < 7 nm would be thermodynamically more stable as SS NPs independently from Fe molar ratio.

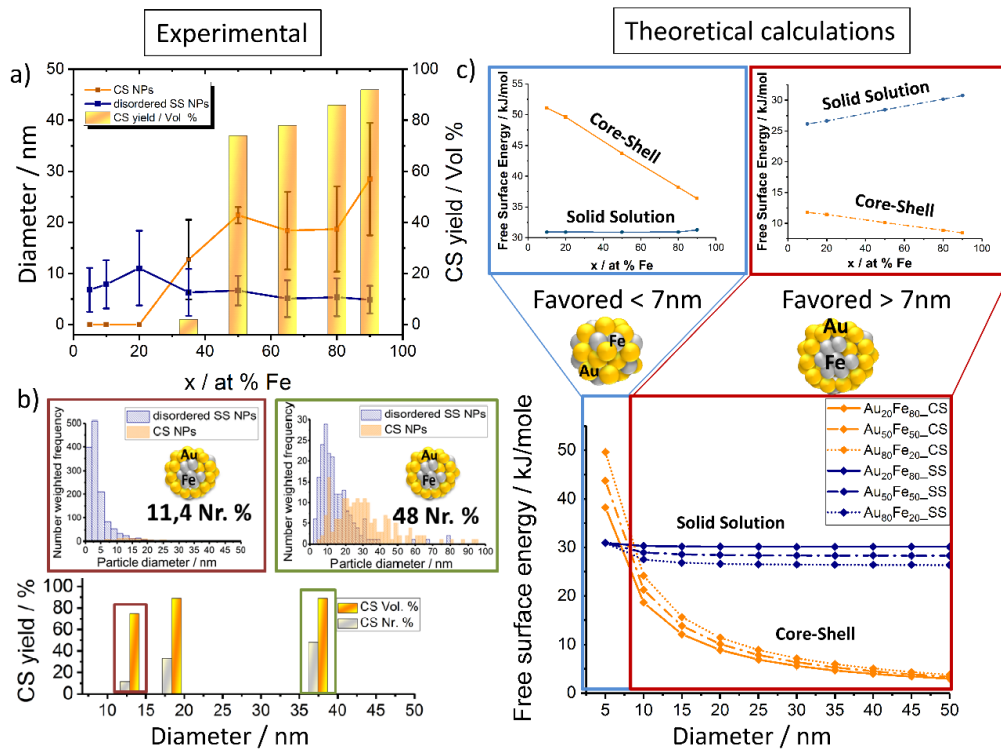


Figure 10: Factors determining the disordered solid solution versus core-shell yield; a) Nanoparticle size-target composition dependency (disordered SS & CS NPs) for Au-Fe NPs generated by LAL in Acetone. b) Influence on the CS yield % based on the average size of Au-Fe NPs for both Volume (Vol. %) and Number ratio (Nr. %) c) Theoretical calculations are based on the Chattopadhyay model.[136]

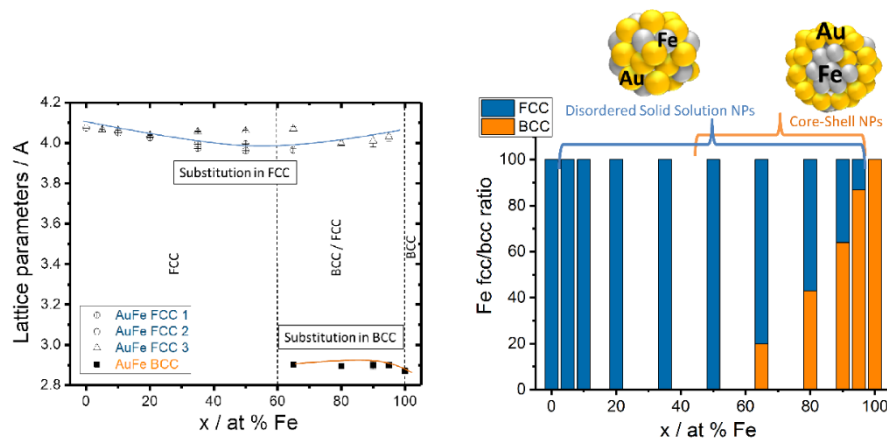


Figure 11: Au-Fe lattice parameters (FCC 1, FCC 2, FCC 3 represent alloy structures with different substitution grades) and weighted phase ratios between BCC/FCC structures measured by XRD.

In the case of NPs with diameters > 7 nm, phase segregation and hence the emergence of CS NPs should be preferred (Fig. 10 c). These calculations confirm our experimental findings, showing CS structures only for mean particle diameters > 10 nm (Fig. 10a). The correlation between diameter and CS yield was further verified by the investigation of two laser-generated colloids with deviating diameter distribution but identical target composition ($\text{Au}_{50}\text{Fe}_{50}$) (Fig. 10b). The results are fully consistent with our expectations, the number of generated CS increases with increasing NPs size. Even though CS yield increased with increasing Fe molar fraction and diameter, the disordered SS alloy NPs are always present independently from the target composition. This is surprising as in accordance to the Hume-Rothery Rule [58], miscibility of Au and Fe defines the system as mostly immiscible (bulk solubility at room temperature: 3% Au in Fe and 0.3% Au in Fe) [56] because of differences in the lattice parameters (Au_{FCC} 4.076 Å; Fe_{BCC} 2.866 Å) and in the surface energies (Au 1.5 Jm^{-2} ; Fe 2.4 Jm^{-2}) [147, 148]. Based on this, the segregated phase (CS) should be the only thermodynamically stable phase. To examine this phenomenon in more detail, we determined the crystal structure of the generated Au-Fe NPs by X-Ray powder diffraction (XRD) including Rietveld refinement and calculation of lattice parameters for FCC and BCC phases (Fig. 11 a, Fig. S5). The analysis revealed, that for target compositions > 65 % a BCC iron phase was dominant in the NPs, which basically coincides with the occurrence of CS phase structures in transmission electron microscopy (TEM). In this context, it should be noted that the lattice constants of this phase are slightly elevated compared to bulk Fe, which points at the partial substitution of iron with Au. In addition, an Au-Fe FCC structure is detectable over the whole composition range, which can be clearly attributed to the disordered SS NPs in gold-rich samples. In iron-rich samples, however, disordered SS NPs and gold-rich shells cannot be differentiated based on XRD. This Au-FCC phase exhibits a reduction in lattice parameters from 4.1 – 3.95 Å while increasing the iron molar fraction up to 65 %, which proves alloy formation and substitutions by iron atoms in the FCC-Au lattice. Thermodynamic calculations, described in more detail elsewhere by Chattopadhyay et al., [136] were employed to predict how the most favored ultrastructure (SS or CS NPs) depends on particle diameter (Fig. 10 c). In this model Gibbs free energies for CS and SS morphology at predefined diameter and composition are calculated, indicating thermodynamically most stable structure by minimum Gibbs energy, confirmed by

Wulff construction[149]. Even though a slight dependence of the free energy on the composition was observed the impact of the as substitutions are significantly higher than those predicted by the bulk phase diagram (Fig. 12), formation of a metastable phase is verified. For iron contents > 65, % the substitution by Fe within the FCC-Au decreases due to competition between BCC/FCC phase as predicted by Baricco [150]. In general, the FCC Au-Fe phase exhibits the strongest negative deviations from Vegard's law at composition around 50:50. Similar observations were also made in Ag-Au nanoparticles produced by the same method [151]. Finally, the mass fractions of FCC/BCC were calculated from the Rietveld refined peaks (Fig. 11b). Here we can clearly observe that an increase in the BCC fraction also goes along with a more pronounced CS formation (compare Fig. 10a). These data show, that next to the size restrictions, the NPs' crystal structure correlates with the phase segregation. However, one peculiarity was found for the Au₅₀Fe₅₀ as well as to a smaller extent for the Au₆₅Fe₃₅ composition. Here we clearly verified the formation of CS structures by TEM, while on the other hand no BCC iron was found. These findings may indicate that CS structures may also form based on two FCC alloy structures (gold-rich Au-Fe shell around iron-rich Fe-Au core) with distinguishable compositions. Here an AuFe@AuFe is formed. The presence of up to three distinguishable FCC structures in the XRD seems to point in this direction, however, this phenomenon cannot be comprehensively explained based on these data.

As we could clearly verify that the LAL-generated Au-Fe NPs are metastable structures with alloy cores and alloy shells, in this final paragraph we aim to elucidate their formation mechanism during LAL based on the bulk Au-Fe phase diagram (Fig. 12). At the first stage, both Au and Fe are rapidly cooled down from the liquid state. Gold would stay longer in this state as its melting temperature is lower (Au 1064°C; Fe 1538°C) [150]. Therefore, at the liquidus line interface, solid Fe would be surrounded by liquid Au. In the case of Fe rich systems, e.g Au₂₀Fe₈₀, Fe can crystallize as either BCC or FCC. Hence both structures will be present upon solidification of the entire phase and will shape the final structure, containing BCC iron-rich cores with minimal Au substitution as well as gold-rich FCC phases, either as isolated particles or as gold-rich alloy shells. Metastable states, in this case, are indicated by higher substitution of Fe in Au and Au in Fe in contrast to thermodynamically-favored phases at room temperature. On the other hand, for Au rich alloys e.g. Au₈₀Fe₂₀ only FCC iron can

form upon crystallization. As phase transformation from FCC to BCC may be kinetically hindered due to the fast cooling inherent to LAL process, therefore only FCC Au-Fe alloy NPs emerged, and no BCC iron is found.

In conclusion, the final internal phase structure (ultrastructure) of Au-Fe NPs generated by LAL in acetone is critically affected by the target composition and the particle diameter. The formation of CS is favored in iron-rich targets (Fe mol % > 35), for particles > 10 nm and results in BCC iron crystal structures. We could conclusively prove that LAL generates non-equilibrium alloy materials containing FeAu@AuFe core-shell structures where core and shell are both alloys. Next to the fundamental significance of this work in understanding the laser-based alloy formation process it may also give access to novel metastable Au-Fe alloy nanomaterials with potential future applicability in catalysis and biomedicine.

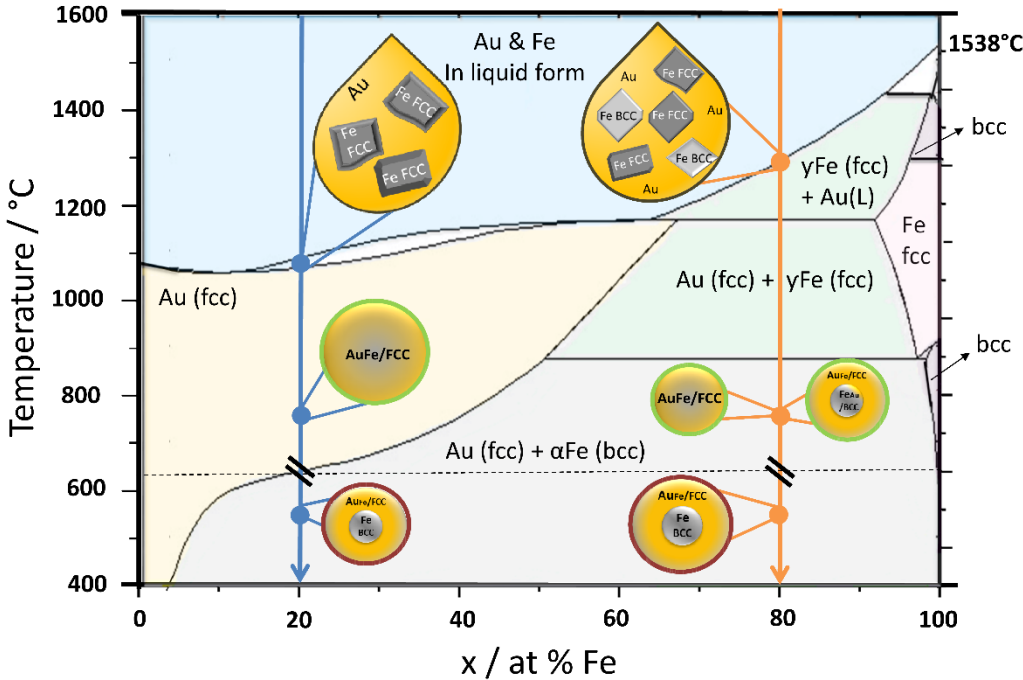


Figure 12: The formation mechanism for Au-Fe nanoparticles generated by LAL. Marked points represent the exemplary phases for Au₂₀Fe₈₀ (orange cool down arrow) and Au₈₀Fe₂₀ (blue cool down arrow) samples. Nanoparticles surrounded with green line represent the metastable phase, whereas red line thermodynamically stable phases. Au-Fe phase diagram redrawn from ref 115

4.1.3.1 Au₅₀Fe₅₀ core-shell ultrastructure verification

Based on the Au-Fe bulk phase diagram independently from the NPs' composition, completely phase segregated iron@gold core-shell morphology would be thermodynamically favored at room temperature (Figure 1)[61]. In other words, the iron core (BCC iron with minimal Au substitution) should be surrounded by Au shell. Nevertheless, in the paper presented in chapter 4.1.3, non-equilibrium alloy formation, with alloy shell and alloy core was reported[152]. For example, Au₂₀Fe₈₀, in which BCC core resembles higher Au substitution contrarily to thermodynamically favored phase, as well as Au rich FCC phase in the form of alloy shell or additional fraction of the NPs. This assumption was made based on XRD analysis, in which calculated lattice constants with elevated values in comparison to bulk Fe, indicated partial substitution of iron with Au (for BCC iron phase). To this end, the experimental data indicates that LAL process during AuFe NP formation is kinetically controlled, as schematically shown in nanoscale phase diagram depicted in Figure 12. Notably, NPs are kinetically hindered during transformation leading to formation of FCC gold shell and BCC iron core. Remarkably, although in the case of Au₅₀Fe₅₀ NPs no iron BCC phase was detected, next to a solid solution, CS fraction was found (Figure 11). From a theoretical point of view, the metastable iron FCC phase would be more easily implemented into gold FCC phase, due to the low driving force for the nucleation[57], leading to the formation of solid solution NPs. However, considering the proposed nanoscale phase diagram (Figure 13), it can be assumed, that similarly like for Au₂₀Fe₈₀, for Au₅₀Fe₅₀ composition iron BCC core with alloy shell should be observed (Figure 12 - green circle). Au₅₀Fe₅₀ composition undergoes a similar transformation path (Figure 13 - violet line) in comparison to another iron-rich composition (e.g Figure 12 - orange line). At very high temperatures (above 1538°C) both iron and gold are in liquid form, followed by rapid cooling up to the liquidus line interface, at which solidified iron would be surrounded by liquid gold. Notably, Fe crystalizes as either FCC or BCC (Figure 13 - green circle), which are considered as metastable phase, due to higher Au substitution into the Au matrix, contrarily to thermodynamically favored phase (Figure 13 - red circle). This complexity is already manifested in chapter 4.1.3. Admittedly, XRD analysis revealed only FCC iron phase, as it may undermine the signal coming from the poly-dispersed

sample, this can be, however, circumvented by the complementary SEAD analysis of individual CS NP.

Therefore, this study is an attempt to address the phenomena of $\text{Au}_{50}\text{Fe}_{50}$ CS formation when two FCC phase (for Au and Fe) are present. In this regard, by the combination of sophisticated STEM, EDX line measurements and SEAD analysis, quantitative composition and crystal structure of the individual components of the $\text{Au}_{50}\text{Fe}_{50}$ CS NP' ultrastructure were determined. (Figure 14 a).

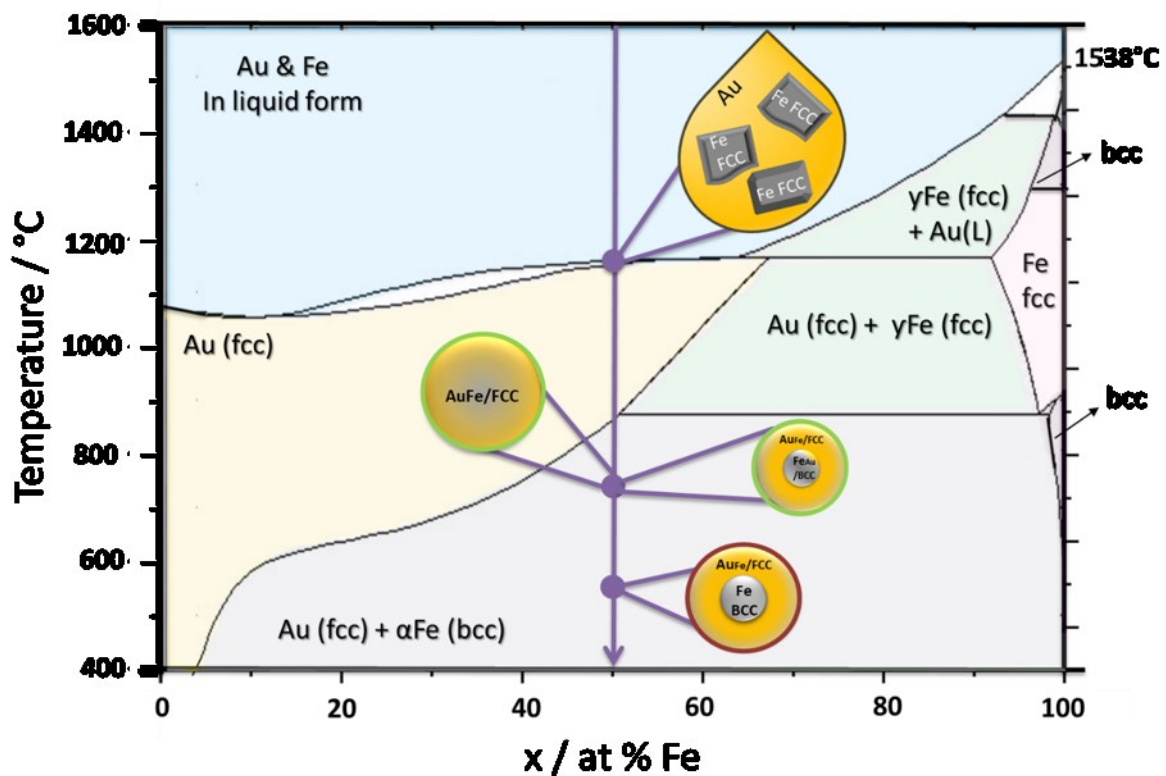


Figure 13: The nanoscale phase diagram proposal for iron-gold system generated via LAL. Marked points represent the exemplary phases for $\text{Au}_{50}\text{Fe}_{50}$ (violet cool down arrow). Nanoparticles surrounded with green line represent the metastable phase, whereas red line thermodynamically stable phases. Au-Fe phase diagram redrawn from ref 56.

Gold and iron elemental distribution of individual CS NP was identified by Z-contrast imaging. The large difference in an atomic number of iron and gold is reflected in the high contrast between dark core and bright shell layout as depicted in Figure 14 a. Substantial element segregation was confirmed by EDX line scan measurement as shown in Figure 14a. Au content decrease into the direction towards the core (between 6 and 10 nm), whereas the content of iron increases. Admittedly, the gold signal

doesn't decrease up to zero in the core part, due to overlapping signal coming from the shell. Based on this data, the core composition can not be fully distinguished, therefore additional evaluation with the help of SEAD patterns was employed.

In this approach, the experimental and simulated diffraction patterns comparison, allowed to exclude the presence of Fe FCC phases in the core, due to missing reflection 002 with 1.71 Å. The fitted pattern for an FCC Fe core does not fit to the experimental results due to wrong intensity distribution and the occurrence of an additional reflection. The intensity is distributed on concentric rings, which coincides with the intensities of Au-FCC and Fe-BCC phases (marked in Figure 14 b in red).

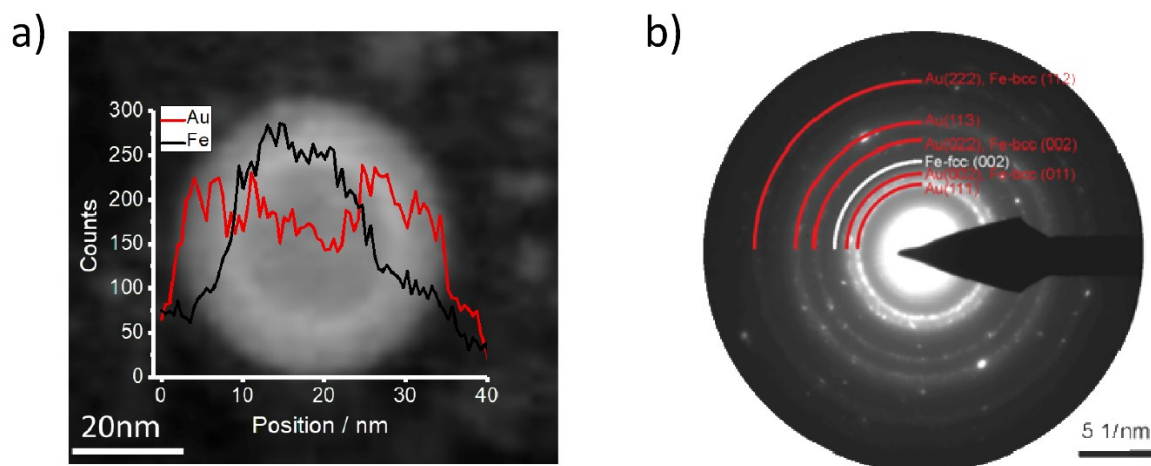


Figure 14: Evaluation of the composition and crystal phase for the representative iron-gold core-shell nanoparticle, evaluated with a) EDX line scan measurements (left) for Au₅₀Fe₅₀ NP, shown in STEM picture (STEM-HAADF detector) b) SAED pattern for Au₅₀Fe₅₀ with fitted simulated ED pattern of a core-shell ultrastructure with Au-rich alloy shell and bcc core (Figure S6).

The accordance with d-spacing and intensity of the fitted and measured diffraction patterns underline the crystal structure of the NPs. Even though, a reflection of BCC Fe and FCC Au overlap, the SEAD pattern confirmed that the lattice spacing of the representative phases fit with the one expected for BCC Fe and FCC Au (Figure 14 b). The results illustrate that core-shell can be formed if the Hume-Rothery rule is fulfilled. This rule states, that next to surface energy, the difference in the crystal phase will contribute towards the phase segregation of the AuFe system. As a results, core-shell structure with iron core (BCC) and gold shell (FCC) would be formed. This statement applies for target composition with Fe content > 50 at. %, where BCC iron phase was detected (Figure 11).

4.2 Impact of target, pulse duration and liquid environment on the final Au-Fe NPs structure

4.2.1 High yield one step laser synthesis of core-shell Au-Fe nanoparticles- the influence of pulse length and target structure

Assuming that the plasma plume ignition and expansion is dependent on the pulse duration, leading to either "hot" (ns) or "cold" (ps) ablation, we could expect changes either within the size or the ultrastructure of the generated NPs[22, 153]. Therefore, long and short pulse durations 8 ns [3,78 J/cm²; 15 kHz] and 10 ps [3,1 J/cm²; 100 kHz], respectively, were analyzed and compared in Figure 15 a-c. In Figure 15 a and b, bulk targets are compared, whereas in Figure 15 c thin layer target is depicted. Laser parameters were adjusted towards comparable fluence (pulse energy/area) and are in a range of approximately 3 J/cm². Based on STEM data, two parameters were considered; ultrastructure (solid solution vs. core-shell and multi core-shell NPs) and the corresponding diameter of the NP.

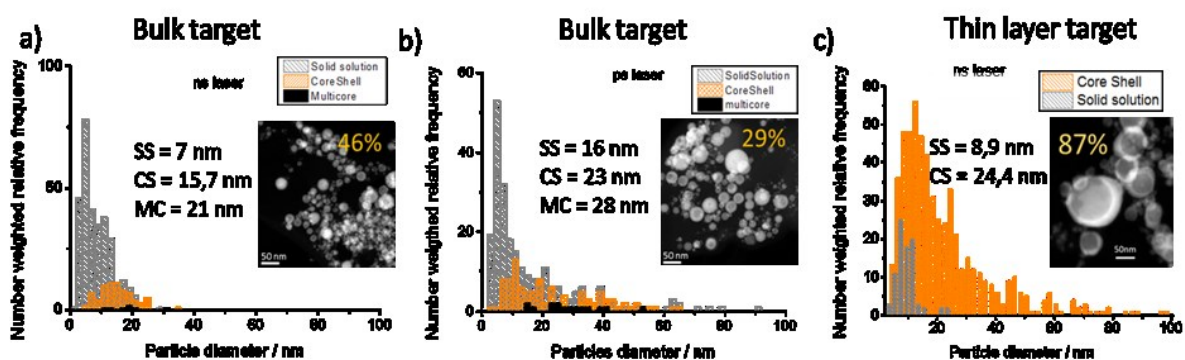


Figure 15: Ex situ histograms of scanning transmission microscopy with mean diameter for SS and CS (black number) nanoparticles, with PS Yield % [CS+MC NPs] (orange number). All results are number weighted. Electron microscopic pictures show representative fraction of core-shell and alloy nanoparticles for a) ablation of alloy bulk target with 8 ns [3,78 J/cm²; 15 kHz], b) alation of alloy bulk target via 10 ps [3,1 J/cm²; 100 kHz], c) ablation of thin layer target via 6 ns [3,1 J/cm², 100 kHz]. In all cases ablation was performed for alloy target configuration with Au₅₀Fe₅₀ composition in acetone.

Notably, for all samples generated via different pulse duration 3 fractions of NPs were detected, SS; CS and MC NPs. As expected from the theoretical calculation presented in chapter 4.1.3, SS resembled an average diameter below 10 nm for ns pulse duration, contrarily to ps short pulse in which SS NPs with 16 nm were found. In regard to phase segregated NPs, in both samples, diameter exceeded 10 nm (ns: 15,7 nm for CS and

21 nm for MC; ps: 23 nm for CS and 28 nm for MC). Interestingly, even though increase in average size was observed, decrease in PS yield occurred (from 46 % / per number & 91% / per volume for long ns pulse duration to 29 % / per number and 89 % / per volume for short ps pulse duration). Indicating, that if batch targets are compared, the short pulse duration may contribute to the formation of kinetically favored ultrastructures.

The reason for that can be found in the formation mechanism, which may be dependent on the pulse duration[117, 153]. A substantial difference by direct comparison between long ns and short ps pulse can be stated to the lifetime of the laser-induced plasma at the solid surface[20]. Remarkably, in case of ultrashort pulse duration – femtosecond pulse duration, ablation is considered to be caused by the almost instantaneous solid-vapor transition of the atoms of the target.[154] This assumption is made based on the fact, that the pulse width is much shorter than the electron cooling time, and therefore electron-lattice coupling time can be neglected[138]. This means that the ablation occurs before the lattice is thermally heated up by the electrons. Contrarily to, ns pulse duration, in which target lattice is heated[103]. Thus, during ns ablation, the pulse width is longer than the lattice cooling time, leading to partial overlap between the pulse and the plasma lifetime. In general, in the case of ns pulse duration, ablation occurs via melting and then vaporization, whereas a part of the energy from the laser is lost as a heat transfer into the target[20, 103]. Hence, for ps pulse duration, the intermediate between long and ultrashort pulse duration mechanism can be assumed, resembling characteristics of the ultrashort fs pulses if the width remains below 10 ps[155]. To summarized, a short pulse is characterized by a phase explosion, whereas long pulse with melting and vaporization, which may impact the diameter of the NP or/and its ultrastructure[20].

Many groups, e.g. Calvo [55], Belashchenko [61] tried to predict and explain by computational modeling, why either solid solution or phase segregation in bimetallic nanoparticles occurs. However, in complicated ultrafast non-equilibrium processes, e.g. laser ablation in liquids, modeling reaches its limitations, as many processes cannot be taken into account. The variation between thermodynamic and kinetic stabilities, along with modeling for systems with thousands of atoms is still challenging. Nevertheless, based on theoretical prediction summarized in chapter 4.1.3, a diameter of the NP, affect the ultrastructure of the NP. Besides, the properties of the NP are in

direct dependency from NPs' structure. One important issue in this context, therefore, is the size distribution. Especially, during ultrashort pulses, which frequently yields bimodal size distributions. The recent modeling approach proposed by Zhigilei's offered a potential explanation claiming that the size of the LAL synthesized nanoparticle is explained based on 2 different formation mechanisms[104, 137]. It is hypothesized, that larger particles form by the ejection of liquid droplets from a superheated metal molten layer, destabilized by Rayleigh Taylor instabilities and impaction from metal droplets from underlying layers. The smaller NP, on the other hand, are believed to be formed by rapid nucleation of ejected atoms and smaller atom clusters. This explanation, confirmed the observed results as shown in Figure 15. Short ps pulse duration, resemble a bigger diameter for PS NPs, yet with a lower fraction in comparison to SS NPs. Here, the smaller SS NPs may be formed by the rapid nucleation, whereas a small fraction of SS NPs by the ejection of liquid droplets, contributing to NPs with a diameter above 10 nm. CS NPs are most likely generated in the region closer to the molten layer as predicted by Povarnitsyn [141].

In the case of ns pulse duration, the formation mechanism simulation is still limited, as only the early stage of the LAL process can be considered[104]. Nevertheless, during long ns pulse duration, as the pulse width is longer than the lifetime of the plasma plume (few ns), additional energy is delivered from the laser pulse directly into the plasma, leading to prolong the lifetime of the plasma plume[103]. In consequence, an ablated matter within the plasma plume stays longer in a heated state ($>5000\text{K}$)[139, 140]. Moreover, prolong plasma plume results in the longer cavitation bubble lifetime, as the higher liquid volume is evaporated[139, 140]. It is worth to mention, that during ps ablation pulse width is too short and therefore, no overlapping with plasma plume and pulse duration will occur. Based on this, the assumption can be made, that ablated matter during ns pulse duration, not only undergoes different ablation mechanism (melting and vaporization), but also the time the ablated matter passes from the hot liquid state into the solid-state may be affected[20]. Owing to the experimental data, NPs generated via ns pulse duration are most likely generated with conditions close to the thermodynamic equilibrium, whereas NPs synthesized via ps pulse duration are kinetically trapped products.

Hence, by application of shorter pulse duration (10 ps) higher PS yield was not achieved, the geometry of the target, more precisely its thickness resembled a huge

advantage towards almost pure PS formation. Next to bulk Au₅₀Fe₅₀ alloy target ablated with 8 ns [3,78 J/cm²; 15 kHz], thin Au₅₀Fe₅₀ alloy target was ablated at comparable conditions with 6 ns [3,1 J/cm², 100 kHz]. As shown in Figure 15, PS yield for thin target with 80 nm thickness, represents 87 % of PS per number (99 % per volume) in comparison to bulk alloy target, where only 46 % of PS per number (91 % per volume) were synthesized as shown in Figure 15 c and a respectively. Next to the high PS formation, diameter increased drastically as well, which is in correlation with theoretical calculation (chapter 4.1.3), predicting phase segregation for bigger NPs (above 10 nm). Overall, the pulse duration can be used to tune the NPs diameter, while the changes of the ultrastructure are negligible. Remarkably, target geometry revealed a huge impact on the PS yield, where PS production doubled from 46 % to 90 % by simply decreasing target thickness to 80 nm.

These findings motivated us (cooperation with Dr. V. Amendola - University of Padova) to perform a series of experiments for thin multilayer targets for both long ns and short ps pulse duration. Previous works already confirmed a distinctive correlation between the size and the AuFe NPs composition (Chapter 4.1.3). Hereby, we aimed to elucidate to what extent the target geometry (bulk vs thin multilayered targets), and the pulse duration (short ps and long ns pulse) influence the yield of CS NPs.

Published in: „One-Step Synthesis of Fe-Au Core-Shell Magnetic-Plasmonic Nanoparticles Driven by Interface Energy Minimization”
Nanoscale Horiz., 2019,4, 1326-1332

Anna Tymoczko, Marius Kamp, Christoph Rehbock, Lorenz Kienle, Elti Cattaruzza,
Stephan Barcikowski, and Vincenzo Amendola

Directing the assembly of atoms into core-shell particles generally requires elegant but sophisticated procedures. Here we show how the thermodynamic driving force to a minimization of surface and interface energy can be exploited to produce colloidal Fe-Au core-shell nanoparticles in one step and with a yield approaching 99.7% in mass. This is obtained by laser ablation with nanosecond pulses of thin bimetallic films immersed in acetone. The Fe-Au core-shell nanoparticles show magnetic and plasmonic properties, and a surface available to bioconjugation and analytical assays. This laser-assisted synthetic method represents a step forward the facile preparation of core-shell nanospheres with multiple appealing functionalities.

One of the main challenges in nanochemistry is represented by the control of atomic assembly into bimetallic heterogeneous nanocrystals with complex structures, such as core-shell (CS) nanoparticles (NPs)[156, 157]. CS is of particular applicative interest because they allow the combination of different properties simultaneously in the same nanomaterial,[158-160] or the construction of new structures with appealing functions.[161] CS NPs are especially desirable for avoiding core degradation in a reactive environment, or for preventing leaching of harmful elements from the core to the surroundings.[147] Besides, organic molecules are easily grafted on transition metals or oxide NPs when these are coated with a noble metal shell.[162]

The unique magnetic, optical, electronic and chemical properties displayed by CS NPs, in comparison to single-phase NPs, come at the price of a more difficult synthesis.[156] To date, CS nanocrystals have been obtained with extraordinary precision in the composition, size, and morphology through elegant procedures,[162-164] especially consisting of stepwise seed-mediated growth in solution.[165] However, these examples often require multiple or complex steps, involving toxic or pollutant compounds, which can introduce impurities due to the many solutions and reagents

involved, or require surface capping agents that limit surface availability of CS NPs.
[166]

An alternative approach to achieve bimetallic crystals with the CS morphology relies on element segregation from a supersaturated solution, because of the minimization of surface and interface energy. In conditions close to thermodynamic equilibrium, this is possible when the CS structure is energetically favored compared to, either the mixed element (e.g. alloy) state in case of miscible elements or to the segregated heterostructure in case of two immiscible components.[166] The transition from a state where elements are homogeneously distributed, like a solid solution (SS), to a system where elements are segregated, like a CS, requires atomic diffusion,[156, 167] that is typically achieved by physical processes such as heating of thin films and consequent solid-state dewetting,[166] or by laser ablation of bulk alloys in liquid environment.[152] [42] However, in solid-state dewetting, CS NPs are obtained on a solid substrate and can be collected only by stripping procedures,[166] unless irreversibly embedded in a solid matrix.[147] This greatly limits the general exploitability of CS NPs such as surface conjugation with functional molecules.

In particular, element segregation from a supersaturated solution was demonstrated for Fe-Au CS, which possesses intriguing magnetic and plasmonic properties valuable for applications in data storage,[166] magneto-optics,[162] catalysis,[24] sensing,[168] and biomedical fields.[169] Notably, Fe-Au CS is rarely achieved in a liquid environment because of the easy oxidation of metallic Fe into iron oxides with lower magnetization and nonmetallic band structure.[156, 166] In case of laser ablation in liquid, Fe-Au NPs are obtained as a colloid, but yet with low CS yield compared to other synthetic methods, due to the production of an unavoidable fraction of SS alloy NPs.[152] Recently, laser melting in liquid (LML) was also applied to the generation of CS submicron spheres by irradiation of a mixture of gold and iron oxide NPs.[170] Although LML has high potential in the control of particle polydispersity,[171] in case of the Fe-Au CS the procedure was limited to a size range of several hundreds of nm and to iron oxide cores. Consequently, it is of great interest to obtain CS NPs by a simple, scalable and possibly green approach.

Here we show that laser ablation synthesis in solution (LASiS) allows the production of colloidal CS NPs in one step, and without the addition of toxic, pollutant or expensive

chemicals, simply starting from an equimolar Au-Fe alloy thin film supported on a soda-lime glass slide. Although LASiS is usually performed with bulk targets, the use of thin films can provide several advantages for laser ablation synthesis of bimetallic nanocrystals. Due to constant progress of Physical Vapour Deposition (PVD) techniques, in terms of quality and deposition rate, as required to meet the increasing demand of the industry, the surface area that can be deposited by a commercial PVD apparatus is usually 2 m² at a deposition rate of 10 nm/minute.[172, 173] Besides, the focal distance of the laser beam does not require continuous adjustment during LASiS with thin-film targets, contrary to what is required by bulk targets due to their consumption.[174]

Here, following the typical LASiS procedure, the metallic film was immersed in acetone, and 1064 nm (6 ns) laser pulses at 22.6 mJ/pulse (3.1 J/cm²) were used to transform the solid material in a colloidal solution of Fe-Au NPs (Figure 16A). Acetone was selected as the most favorable liquid environment for the formation of Fe-Au CS nanoparticles, according to our previous reports.[42, 175, 176] Besides, the colloids obtained in acetone exhibited excellent stability for several days, with only a slow tendency to sedimentation over several weeks (SI7). In the second part of this study, the results are compared to complementary experiments conducted in the same liquid environment and with the same wavelength of 1064 nm, but with 10 ps pulses at 0.08 mJ/pulse (4 J/cm²).

The colloid obtained by ns LASiS of the equimolar Fe-Au film in acetone was analyzed by scanning transmission electron microscopy (STEM) with the HAADF detector (Figure 16B) to investigate element distribution in the NPs by Z-contrast imaging. The Fe-Au system is favorable for the investigation of CS owing to the large difference between the atomic numbers of the two constituting elements.[177] From the dark-core/bright-shell NPs layout observed from Z-contrast STEM images, it is immediately evident that the sample is composed of CS NPs where the low Z element segregated in the core and the high Z element accumulated in the shell. In rare cases, multiple cores are embedded in the same shell. The CS morphology is robust enough to remain stable in the liquid as well as after deposition on the TEM grid, without the need for a protecting layer as in other reports.[147] The chemical composition of the NPs was analyzed by scanning transmission electron microscopy with energy-dispersive X-ray spectroscopy (EDXS) and resulted to be Fe 50 ± 5 at.% and Au 50 ± 5 at.%, i.e.

unchanged compared to the alloy target composition. EDXS unambiguously identified the distribution of Fe and Au atoms within individual CS (Figure 16C). EDXS line scan on a couple of CS NPs (Figure 16D) further substantiated element segregation into CS architecture.

Although the reflections of body centered cubic (bcc) Fe and face centered cubic (fcc) Au overlap, the selected area electron diffraction (SAED) pattern taken from CS NPs (Figure S8) shows that the lattice spacing of the respective phases agree with those expected for bcc Fe and fcc Au. Besides, the comparison of the SAED pattern with simulated patterns reported in Figure 16E allows to exclude the presence of fcc Fe phases. Joined with the CS structure evidenced by the Z-contrast images and EDXS analysis, this allows the conclusion that the CS NPs should be two components with different crystal structure Fe-bcc (core) and Au-fcc (shell). Besides, the optical absorption spectrum of the CS colloid (Figure S9) exhibits an absorption edge in agreement with previous reports about LASiS of CS Fe-Au NPs in acetone.[42]

The size distribution measured by TEM (Figure 16F) has the well-known LogNormal structure expected with LASiS, whose origin has been recently explained by molecular dynamics simulations of the ablation process.[178] From a detailed analysis of STEM images, it is found that a minority of homogeneous solid solution (SS) NPs exist and that this population is limited to relatively small sizes below 15 nm. Overall, in number-weighted particle size characterization, the fraction of CS accounts to the 87% of total, that reaches a remarkable value of 99% for sizes above 15 nm. It is worth to stress that a conservative approach was adopted for these statistics, because all NPs with size below 5 nm were counted as SS, due to the difficulty of a precise discrimination between the two morphologies in this size range from Z-contrast STEM images. However, for those applications where the surface is the reference parameter, such as catalysis[179] or realization of smart self-assembled plasmonic nanosystems coated with functional molecules,[161, 180] the CS NPs accounts for the 99% of the total available surface. The overwhelming weight of CS population becomes nearly unity (99.7%) when the volume-weighted distribution is considered. Despite the unavoidable fraction of small SS NPs, these values point to laser ablation in liquid as a highly efficient route to the generation of CS NPs relevant for surface or mass-weighted applications such as in magnetism, plasmonic and nanomedicine.

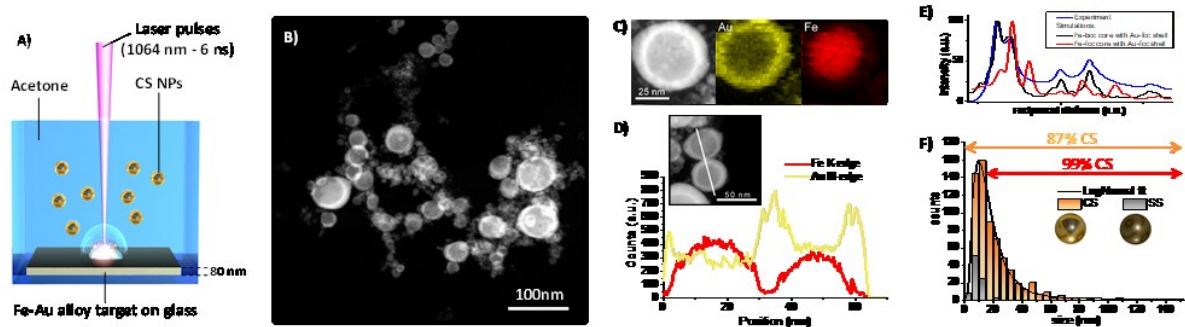


Figure 16: A) Sketch of synthetic approach based on laser ablation in liquid: laser pulses are focused on a Fe-Au alloy thin film supported on soda-lime glass and dipped in pure acetone, and NPs resulting from metal film ablation are collected as a colloid. B) Representative Z-contrast STEM image of NPs, showing core-shell structure. C) Bidimensional EDXS elemental maps of a representative CS NP, with Au shell in yellow (M-edge) and Fe core in red (K-edge). D) EDXS elemental line scan analysis on a couple of CS NPs further demonstrates Fe segregation in the core (red line) and formation of the Au shell (yellow line). E) Rotational average intensity profiles of the experiment (blue line) and the simulations for a CS NP with Au fcc shell and Fe-bcc (black line) and Fe-fcc (red line) core. The presence of Fe-fcc can be excluded by comparing the simulated diffraction intensities, overall indicating that the SAED pattern is compatible with a nanostructure containing Au-fcc and Fe-bcc. F) Size histogram of NPs is well fitted with a LogNormal function (black line), and is composed by 87% of CS NPs and 13% of SS NPs. The fraction of CS is 99% in the size range above 15 nm. Reproduced from Ref. with permission from The Royal Society of Chemistry

The Fe-Au CS NPs show a ready response to the external magnetic field and can be easily aligned on a substrate such as a glass microscope slide by approaching a permanent magnet (see Figure 17A). This is relevant for the realization of transparent coatings with improved conductivity.[181] Besides, given the presence of a plasmonic gold shell, these nanoparticles can be conjugated with thiolated molecules, purified by magnetic attraction, and exploited for surface enhanced Raman scattering (SERS) detection of compounds adsorbed on their surface, as demonstrated with an aromatic thiol (nitrothiophenol, Figure 17B). Effective surface functionalization is key to improve sample monodispersity after LASiS, that typically requires the addition of stabilizing ligands after the synthesis, followed by post-synthesis selective centrifugation approaches,[182] although this procedure is sometimes difficult in case of ferromagnetic NPs.

The ability of the CS NPs to act as nanoantennas was demonstrated further by SERS detection of a benchmark Raman reporter such as malachite green (4-[(4-dimethylaminophenyl)phenyl-methyl]-N,N-dimethylaniline), even at a concentration as low as 10^{-8} M, equivalent to 10 fmol of analyte added (Figure 17C). These values are comparable to those typically achieved with magnetic-plasmonic nanosystems, which

spans from 10^{-6} to 10^{-15} M depending on analyte type, volume of solution added, excitation wavelength and acquisition time.[183, 184] In fact, local electromagnetic field enhancement of up to a factor of 30 was estimated at a wavelength of 532 nm by numerical calculations on a representative dimer of coupled Fe-Au CS NPs, which corresponds to a SERS enhancement factor of 10^6 at the electromagnetic hot spot between the two NPs (Figure 17D). Local field enhancement is known to scale with the volume of the NPs,[185] and it is therefore very favorable in the present CS NPs because of their size in the range of tens of nanometers. For this reason, the calculation in Figure 2D refers to a dimer of CS NPs with relatively large size, compared to the TEM measured size distribution, because the strongest contribution to SERS signals comes from the tail of NPs with larger size.[185, 186] However, also if we consider a dimer of CS NPs with the average size (22.4 nm) and shell thickness (4.4 nm) extracted from TEM analysis, a SERS enhancement factor of 10^6 at the electromagnetic hot spot between the two NPs is observed (Figure S9).

The synergy of magnetic and plasmonic properties can greatly facilitate the SERS experiments, in terms of time, signal intensity and amount of material used because the CS NPs can be accumulated in a pre-determined point of the substrate prior to the analysis, by using a small permanent magnet.[183, 184] This is shown in Figure 26E, where a tiny amount of either CS NPs (0.7 μg , 10 $\mu\text{g}/\text{mL}$) or a SERS benchmark represented by commercial Au NPs (50 nm in diameter, 1.5 μg , 22 $\mu\text{g}/\text{mL}$) was mixed with 7.5 pmol of MG in water and drop casted on a glass substrate. Due to the stability of CS NPs, solvent evaporation without the presence of magnetic field does not leave any appreciable agglomerate that can be used for SERS analysis (left side of Figure 26E); in fact, the Raman spectra recorded on the area of deposition do not contain the spectral signature of the analyte. When the same colloid is evaporated by placing a small (2 mm in diameter) permanent magnet below the glass substrate, the CS NPs are accumulated in a single point, that can be easily identified by the naked eye and emits bright Raman signals coming from the analyte (center of Figure 17E). Even in case of the reference Au NPs sample, the deposit is rather homogeneously distributed on the glass substrate after solvent evaporation, but some aggregates can be observed thanks to the higher concentration and lower stability of the colloid (right side of Figure 17E). In this case, the spectral signature of MG is observed in some of the aggregates, although not in all of them, which forces the operator to a time-consuming

total thickness (Figure 18A) where the two elements are completely segregated in a bilayer (Fe/Au/glass or Au/Fe/glass) or in a quadrilayer (Au/Fe/Au/Fe/glass) that can be considered as an intermediate case between the bilayer and the single alloy layer. Previous experiments about laser ablation of Fe-Au multilayers in ethanol and water evidenced that the two elements are mixed during the process, resulting in bimetallic NPs.[176] Indeed, also in this case CS yield is lower with multilayer targets than with the alloy film (Figure 18B), although surface- or volume-weighted CS fractions with still good yield of 90% are measured in samples originated from laser ablation of the Fe/Au and the Au/Fe/Au/Fe films. The general trend suggests that the targets with a topmost layer of Au show the lowest CS yield, while the alloy film ablation provides the largest CS yield. This is a favorable point for CS synthesis because the production of a single homogeneous Fe-Au alloy film by various well-established large scale thin film deposition technologies is more convenient compared to multilayers.[187]

It should be noted that the best yield of CS by LASiS reported in literature to date (48% in number) was achieved with bulk Fe-Au alloy targets in acetone, using 1064 nm nanosecond laser pulses and 0.36 mJ/pulse (4 J/cm²).[152] This motivated a further laser ablation experiment with a lower pulse energy of 0.08 mJ/pulse (4 J/cm²), using 10 ps pulses at 1064 nm. The resulting CS yield is clearly lower than with ns pulses (Figure 18C), pointing to the importance of laser pulse parameters in the determination of NPs morphology.

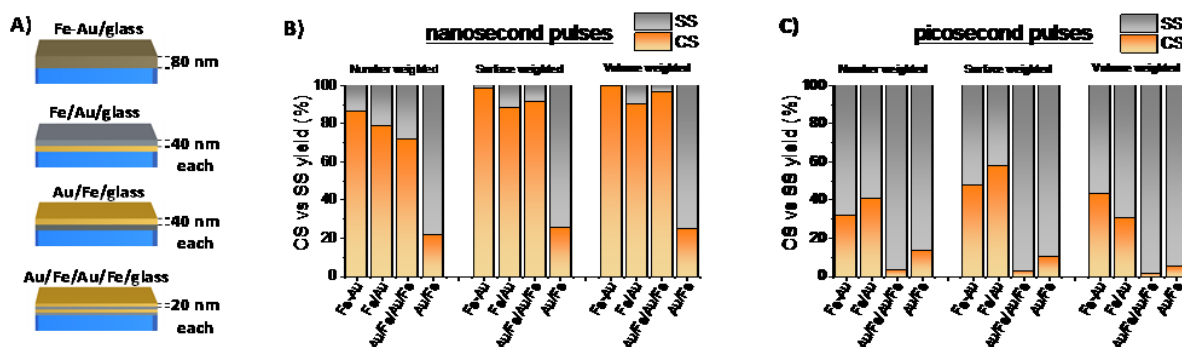


Figure 18: A) Different types of Fe-Au films tested for LASiS of Fe-Au NPs in acetone. B) CS versus SS yield measured for samples obtained by ns laser ablation of the different film types. C) Same as B) but for ps laser ablation.

In parallel, a difference in the size histograms of NPs is observed by changing film structure and laser pulse parameters (Figures S10 and S11), with a prevalence of small particles in samples obtained with ps pulses. On the other hand, as shown in Figure 19A, a clear correlation exists between average NPs size and CS yield, with higher CS yields found when mean diameters of the particles are higher, which prevalently occurs in nanoparticles from ns-pulse ablation. The plot of Figure 19A suggests that the fraction of CS NPs is negligible when NPs average size extracted from the LogNormal size distribution is below ca. 10 nm. In addition, Figure S12 shows that high CS yield occurs when the CS fraction has a larger mean diameter than the corresponding SS fraction.

To understand the structural behavior of Fe-Au NPs, one should consider that the thermodynamic driving force for element segregation relies on the reduction of interface energy.[157, 167, 188] It is known since the contribution of J. W. Gibbs in 1874,[189] that the morphology of a given material is such that the total surface energy is minimal, and the Fe-Au systems are characterized by a large difference in surface energies between Fe and Au (1.500 J m^{-2} for (111) Au compared to 2.417 J m^{-2} for (100) Fe).[177] Besides, the Fe-Au system supports several other features suitable for element segregation and formation of CS nanocrystals, which are the structural dissimilarity of body-centered cubic (bcc) iron and face-centered cubic (fcc) gold, and the large difference in lattice parameters (0.28665 nm for Fe cell and 0.40784 nm for Au cell).[147, 166, 177, 190] The different crystal structure of Fe and Au accounts also for the large miscibility gaps of the bimetallic system, with the solubility of Au in bcc Fe that is just 0.1 at.% even at 500 °C. [147, 177]

To illustrate how the balance between surface and interface energies determines the morphology of Fe-Au NPs, a thermodynamic model for interface segregation was applied (see ESI for details). Consistently with previous findings about laser-generated Fe-Au CS nanocrystals,[152] the thermodynamic model clearly shows that smaller nanoparticles have higher thermodynamic tendency to remain in a single phase (Figure 28B), whereas, above a size threshold of 10 nm for Fe(50)Au(50) nanocrystals, the thermodynamically stable phase is the CS structure. The reason is that quantities such as surface and interface energies scale with the fraction of interface atoms over the total, dominating the energetic balance for particles smaller than ca. 10 nm in diameter.[188] In the SS structure, the fraction of surface Fe atoms increases with the

total fraction of Fe, and Fe is characterized by the highest surface free energy contribution, therefore the size threshold for CS formation is lower for higher Fe content (see Figure S12 in ESI).

The results of Figure 19B are compatible with the trend of Figure 19A, when considering that NPs size distribution is LogNormal. In fact, the linear trend in Figure 19A is the consequence of the progressive shift of the LogNormal size distribution to smaller sizes and the concomitant decrease of the fraction of NPs exceeding the thermodynamic threshold for CS formation.

Overall, the energetic difference between CS and SS helps understanding how surface and interfacial energies affect the geometry of Fe-Au NPs. However, the correspondence between the thermodynamic model and our experimental results is not complete, given the presence of SS NPs larger than 10 nm in several samples. In LASiS, CS formation occurs as a consequence of nanoparticle cooling in conditions close to thermodynamic equilibrium from the melted state, where element distribution is homogeneous, to the solid state, where a thermodynamic driving force to element segregation is observed in the bulk Au-Fe alloy phase diagram.[152] At the nanoscale, the thermodynamic advantage in element segregation is partially balanced by the energy needed for the formation of new interfaces, which is larger for smaller nanoparticles, resulting in CS NPs only above a size threshold of ca. 10 nm for equimolar Fe-Au composition (Figure 19B). In practice, it should be noted that thermodynamic equilibrium models are not applicable for kinetically trapped products,[152, 157, 188] and Fe-Au alloys can exist in metastable state when atomic diffusivity is rapidly frozen.[152, 175, 191] For instance, the cooling rate of ablated matter with ps pulses has been simulated by Zhigilei et al. to reach $\sim 7 \times 10^{11}$ K/s.[178] Here, we found that 99.7 % in mass of CS nanoparticles is achieved by laser ablation with ns pulses of 80 nm thick Fe-Au alloy film in acetone, while LASiS with ps pulses gives low CS yield. According to molecular dynamics simulations and plasma diagnostics experiments, laser ablation mechanism is different when ns or ps pulses are used.[112, 178, 192, 193] In particular, with ns pulses, the laser beam partially overlaps in time with the plasma plume and contributes to heating the plasma.[192] With ps pulses, the overlap between laser beam and plasma plume only occurs for a negligible fraction of the plasma plume lifetime, that is on the timescale of hundreds of ns.[192] Therefore, although the exact formation mechanism of CS NPs in LASiS

deserves further investigation to be fully elucidated, we can hypothesize that, in LASiS with ns pulses and thin alloy films, the majority of nanoparticles pass from the hot liquid state to the solid state in a condition that is close to thermodynamic equilibrium, resulting in CS nanoparticles (as sketched on the right side of Figure 19C). With ps pulses, the largest fraction of NPs forms far from thermodynamic equilibrium (as sketched on the left side of Figure 19C). Another contributing factor is the size of NPs obtained with ns pulses, which was observed to exceed the size threshold for CS formation.

Besides, it is well known that a cavitation bubble (CB) occurs during later stages of NPs formation in LASiS, and that CB lifetime can play a role on particle formation because, during this stage, the NPs are immersed in the CB gas phase.[192, 193] CB lifetime increases with the laser pulse energy (in this case, it is 22.6 mJ for ns pulses and 0.08 mJ for ps pulses).[192] Because cooling rates in the gas phase are much lower than in the liquid phase, the particles formed in a longer-lasting CB have more time to reach thermodynamic equilibrium by element segregation, as required for CS formation. On the other hand, shorter CB lifetimes would mean the NPs are more quickly exposed to the cooling liquid, forming metastable structures before that element segregation occurs, as required for SS formation.

Therefore, both the differences in pulse duration and pulse energy are compatible with the experimental observation that, with ps pulses: *i*) nanoparticles have smaller average size, and *ii*) the nanoparticles prevalently consist in the metastable solid solution also when the size is above the thermodynamic threshold for element segregation into CS structure.

In the case of LASiS with ns pulses, a further advantage is represented by the use of a thin film target instead of a bulk one. In fact, previous experiments of LASiS with thin Au films evidenced that the average size of nanoparticles continuously decreases by increasing the thickness of the target from < 100 nm to > 100 nm.[194]

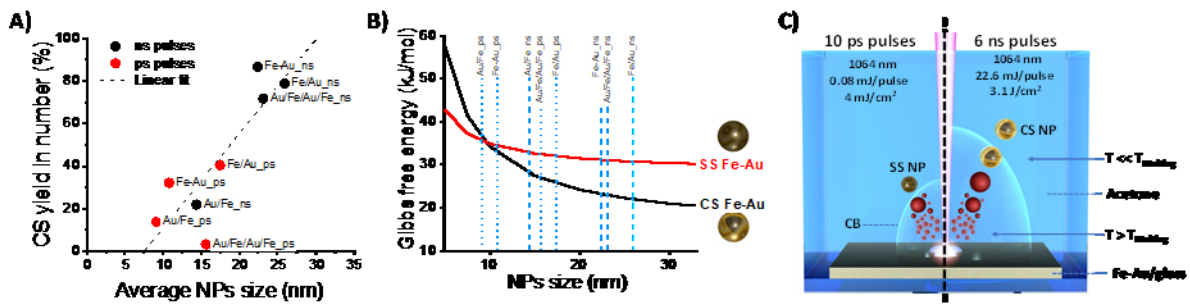


Figure 19: A) Plot of average Fe-Au NPs size versus CS yield for the samples obtained with ns (black dots) and ps (red dots) pulses from laser ablation of the four film types. Linear fit of experimental results is also reported (dashed line), indicating the absence of CS NPs for average size approaching 7.5 nm. B) Gibbs free energy calculated for SS (red line) and CS (black line) morphologies as a function of NPs size, for a composition of Fe:Au 1:1. C) Sketch of NPs formation during LASiS with the Au-Fe alloy target: with ns pulses (right), NPs form by cooling in conditions close to thermodynamic equilibrium, and with average size exceeding the thermodynamic threshold for element segregation into CS morphology; with ps pulses (left), NPs form by quick cooling in conditions far from thermodynamic equilibrium, and with average size not exceeding the thermodynamic threshold for element segregation into CS morphology, thus remaining in large part in a metastable SS phase.

In summary, we presented a facile synthetic strategy to produce colloidal Fe-Au magnetic plasmonic CS NPs in one step. The core-shell architecture, with Au atoms forming homogeneous layers around Fe cores, is achieved with yield of 87% in number and 99.7% in mass by the equilibrium segregation phenomenon, because of the reduction of the total interfacial energy in the system. The procedure, based on laser ablation of an alloy thin film in acetone, is simple, green and does not introduce chemical contaminants. We further showed that CS core-shell NPs yield versus solid solution NPs is tunable by adjusting the thin film structure and laser pulse parameters. The potential of this method is large, considering that it exploits widely implemented thin-film technologies and well-established laser ablation in liquid procedures to generate nanomaterials with complex structure and multiple functionalities of interest for forefront applications in catalysis, nanomedicine, photonics, and information technology.

4.2.1.1 Theoretical model for AuFe NPs

Herein in chapter 4.1.3 and 4.2.1 a significant discrepancy between the theoretical model and experimental data was observed. Hence, in previous calculation pure elemental gold shell and pure elemental iron core were considered, the EDX line scan supported by SEAD analysis confirmed alloy character of the shell (Figure 14). The thermodynamic calculations published by Chattopadhyay et al.[46] consider NPs composition and the NPs diameter and describe thermodynamic force to minimize the surface and interface energy, based on the size and the composition of the NPs. The limitations of this approach are, however, the application only of either fully segregated phase (CS) or fully mixed-phase (SS). In order to implement the complexity of additional possible ultrastructures, e.g alloy shell and pure iron core updated model are employed to the existing equation. All changes within the initial equation (Equation A) used to perform the theoretical calculations of the Au-Fe alloy shell and iron core system were described in chapter S5-1 (equation C) (Figure 20 e-3), with results shown in Figure 20 d.

Moreover, an additional discrepancy was found between experimental and theoretical models, as some of the NPs exceeded the 10 nm size restriction for the solid solution phase (chapter 4.2). Therefore, after a detailed evaluation of the model, an updated version of the equation was proposed. In the initial model (chapter 4.1.3) false assumption was taken, that diameter used for e.g calculation of the size-specific surface energy, the number of atoms on the surface of particle of particular diameter or another diameter dependent parameter is considered as an average nanoparticle diameter (equation A) and can be applied as one value for iron (D_{Fe}) and gold (D_{Au}). Nevertheless, an updated version is proposed, in which diameter for iron and gold are considered individually. In this context, in the adapted model (equation B), a diameter of the core and shell are considered separately as schematically shown in Figure 20 e-2. Updated calculations are described in detail in chapter S5, with resulted theoretical calculations depicted in Figure 20 c.

In this context, all calculations were performed for 3 representative compositions $Au_{15}Fe_{85}$, $Au_{50}Fe_{50}$, and $Au_{85}Fe_{15}$. At last, the threshold for phase-segregated ultrastructure was determined as cut off diameter as depicted in Figure 20 f for all equations (A, B and C).

In the following chapter, calculation toward the most favored equilibrium phase was evaluated. Thus, the most favored state would be if Gibbs free energy would have the lowest value, as the interface and surface energies should be minimized in order to formed phase in thermodynamic equilibrium[189]. The results obtained based on the Chattopadhyay's model[46] showed small variation in Gibbs free energy for representative $Au_{50}Fe_{50}$ SS NPs, where the values differ between 25-31 kJ/mol (Figure 20 a; S14). Notably, SS NPs with high Au content is characterized by lower Gibbs energy. On the other side, Gibb's free energy for CS NPs varies between few kJ/mol up to 50 kJ/mol. Contrarily to SS NPs, Fe rich, bigger NPs have smaller free surface energy. These results indicate that next to the NPs diameter, the composition may contribute to the thermodynamic equilibrium of the NPs. A similar trend has been observed for adapted equations B and C, as shown in Figure 20 c and d. Yet, the overall shift towards higher free Gibbs surface energies was observed. Concerning the competitive process between CS and SS NPs, the most relevant information is, however, obtaining the threshold Gibbs free energy for CS NPs. This complexity is already manifested in experimental data, in which synthesis of the pure CS fraction was not successful so far. A similar trend can be observed for equations B and C, in which NPs with a smaller diameter are more favoured for SS, whereas NPs with bigger diameter for phase segregated phase – CS. In order to address the impact from size threshold on the particular morphologies, cut off diameter towards CS phase was established and compared between results obtained from different equations (A, B and C). To that end cut off diameter, resembling diameter which needs to be reached to form CS in thermodynamic equilibrium is summarized in Figure 20 f. In the case of the first model (equation A), cut off diameter was around 9 nm for Au-rich NPs and 7 nm for iron-rich NPs. Independently from the equation modification similar trend was observed, where iron-rich NPs showed the smallest cut off diameter. For the second modification in equation B, cut off diameter increased up to 20 nm for Au rich NPs. On the other side, $Au_{50}Fe_{50}$ resembled a small deviation from the first equation (A) and is characteristics wit value 10 nm. Iron-rich NPs cut off diameter did not change. In the case of alloy shell and pure iron core NPs (Equation C), the trend remained in which Au rich NPs have the highest cut off diameter with value 23 nm. Whereas for $Au_{50}Fe_{50}$, increase up to 13 nm, and for iron-rich up to 8 nm was observed. Remarkably, an adaptation of the equation A, leads to CS-threshold shift from 10 nm to above 20 nm

for Au rich NPs (Figure 20 c, d, f). Indicating, that for systems where competition between SS and e.g. alloy-shell iron-core is considered,

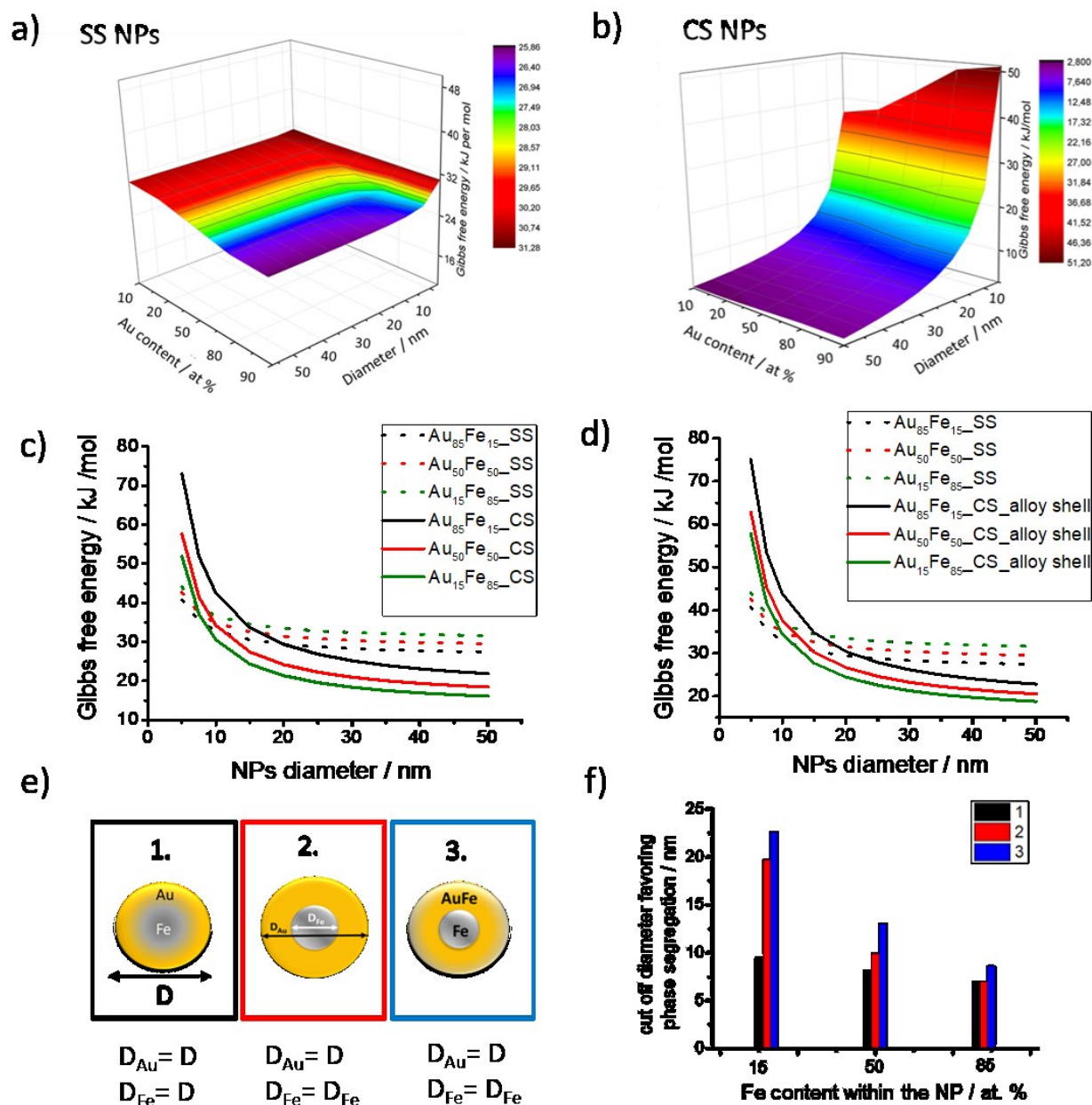


Figure 20: Theoretical evaluation of phase thermodynamic equilibrium characterized by calculated Gibbs free energy for a solid solution (SS) and core-shell (CS) particles based on the model described elsewhere¹⁶¹ and summarized in form of 3D graphic (a-b). Note, that the variation between the Gibbs free energy for SS resemble low deviation in contrast to CS particle. Moreover, phases in thermodynamic equilibrium were further evaluated for the model with adapted iron and gold diameters as schematically shown in e-1 and e-2, as well as evaluation of the CS with alloy shell and pure iron core (d, e-3). The calculation performed with the updated values is described in more detail in chapter S5 and S5-1. Threshold diameter favouring CS particle was determined as a function of particle composition (f).

SS with a bigger diameter would be possible. This validated the detection of few SS NPs with sizes above 10 nm. Nevertheless, this applies only for Au rich NPs, as in the case of Fe rich threshold for CS NPs don't exceed 13 nm, for all adapted equations (equation B and C).

The substantial difference between the threshold for CS phase applies only to the gold-rich system, where the threshold required for phase segregation formation shifted from 10 to 20 nm. This can explain the absence of phase segregated NPs for Au rich NPs (chapter 4.1.3) and the presence of few SS NPs which were bigger than 10 nm (chapter 4.2). Interestingly, for a system with Fe content above 50 at % the variation between threshold size for 3 evaluated equations, remained within a few nm ranges. This can be explained by the similarity in size between the iron diameter (D_{Fe}) and Au diameter (D_{Au}), excluding a remarkable impact of the updated value on the overall equation. In regard to alloy shell and pure iron core, threshold size for phase segregation show the highest values. For gold-rich systems, 22.5 nm were calculated, whereas for iron-rich system size below 10 nm, but still approximately 3 nm higher than the values for pure gold shell and the iron core. This can be explained, by the fact that alloy shell and iron core are not in thermodynamic equilibrium, therefore they require higher energy input to be formed.

To summarize, the thermodynamic model considering NPs composition and the size can be successfully implemented as an additional tool towards ultrastructure control. By this method NPs diameter threshold can be established for 3 various ultrastructures, SS, CS with pure elemental gold and iron and finally, CS with alloy shell and pure elemental iron. Nevertheless, despite NPs composition and NPs diameter can be considered in this model, aspects such as liquid environment nor pulse duration can be implemented into the equation. Therefore, the additional experimental approach would be useful to address the NP formation mechanism during LAL.

4.2.2 Ultrastructure, colloidal stability and size distribution of core-shell Au-Fe LAL generated NPs tuned by the liquid environment.

The nanoparticle formation during laser ablation is impacted through many factors, e.g target composition, laser parameter or even target geometry as demonstrated in previous chapters (4.1-4.2.1.1). Therefore, by adjusting the ablation approach and choosing the suitable parameter, control over the ultrastructure can be achieved. Nevertheless, the interaction between Au-Fe NPs and the liquid environment has not been addressed in the literature in a comprehensive way so far. The reason is the difficulty with the execution of a systematic parameter study, as even for one group of liquids many parameters such as viscosity, density, refractive index, etc. change at the same time. Since the systematic evaluation of specific parameters is not possible, a simplified overview of physical properties' impact on the nanoparticle's ultrastructure, size, and colloidal stability is assessed in this chapter. Therefore, chemical interaction between particles and liquid species will not be taken into account. In this regard selected parameters such as heat capacity, chain length and viscosity will be systematically evaluated. For this purpose, 3 groups of liquids were chosen, ketones, alcohols, and glycols with additional highly viscous PAO40 oil, respectively.

Wagener et al. presented, that LAL in ultra-pure water caused reversed CS ultrastructure with a gold core and iron oxide shell[42]. Oxide and hydroxide species are frequently found during LAL, as the dissolved oxygen and oxidizing species are formed from the plasma-induced decomposition of water, and those species will interact with the ablated matter[39, 105, 109]. Despite the higher solubility of oxygen in acetone in comparison to water, less oxidized NPs were found. This oxidation of the ablated material is predicted to occur at the early stages of the cavitation bubble lifetime[105]. So far Amendola et al. validated this theory by evaluating the impact of the upper layer on the final composition of the NPs within the liquid environment with oxidizing character [17]. The approach was based on the evaluation of the NPs generated from thin-film targets with either gold or iron in the outer layer ablated in water. Element in the upper layer, which was more sensitive to oxidation (iron), lead to formation of iron-rich alloy NPs. Briefly, this effect arises from the sacrificial layer of the outermost layer being oxidized, allowing lower layer form alloys with high abundance of iron. These results seem to indicate that the oxidation of the NPs occurs at the early

stages of the ablation. Nevertheless, thermodynamically driven oxidation may occur at later stages in the liquid for highly sensitive materials[195]. Therefore, the conclusion can be drawn that the stabilization effect of the liquid may have a more pronounced impact on the AuFe NPs than the chemical reaction between the ablated species and dissolved O₂. More precisely, the interaction of solvent or solvent residues and not only the oxidation by dissolved O₂ rules particle stabilization and ultrastructure. Another example of stability control of pure elements may be achieved with pH adjustment[20] or with low electrolyte concentration[108], as the surface charge density increases due to anion-specific adsorption on the NPs surface[196]. Highly charged surfaces contribute to the electrostatic stabilization of the particle. Alternatively, the addition of surfactants stabilizes NPs through steric effect[20]. Indeed, control can be won by the addition of surfactants or by adjusting pH (possible only in water), however, the main focus of this work lies on detailed analysis of the physical liquid parameter such as viscosity, heat capacity, surface tension, etc, and therefore additional stabilization techniques will not be evaluated.

To validate the theory, that the CS Au-Fe ultrastructure is stabilized by the surrounding liquid, the experimental approach was focused on the comparison between water and acetone. To illustrate the impact of the stability on the ultrastructure two references; acetone, water and one mixture of water and acetone (1:1) were analyzed for the Au₅₀Fe₅₀ system. One remarkable consequence of the acetone stabilization for Au would be the formation of the CS with an iron core and gold shell. The stabilization is expected to be provided by the formation of enolates and alcoholates. Therefore, a clear trend with an increase in diameter and CS yield should be observed by the addition of acetone in water. Owing to oxidation character of the water, based on Wagener et al. findings[42], it would be expected that reversed CS with iron oxide shell and gold core or alloy with oxidized iron will be found. This approach was evaluated based on the CS yield (in this case all phase segregated NPs present) and the NPs size. Results are summarized in Figure 21 a-c and e. CS yield increases from 6 % (in number) in water up to 50 % (in number) in acetone, while 50:50 Vol % water-acetone mixture still resembles 39 % (in number) of CS NPs. This trend goes along with a shift towards bigger diameters and broadening in size distribution for NPs ablated in pure water, which indicates low colloidal stability. Furthermore, the colloidal stability of the NPs was confirmed by UV-Vis spectroscopy measured at day 1 and day 30, confirming

that acetone provides better colloidal stability in comparison to water (Figure 21 d). In the case of water decrease of absorbance indicates NPs agglomeration after 30 days of storage. Remarkably, NPs in water reached 80 nm in size, whereas for acetone and acetone water mixture only 20 nm and 15 nm were observed, respectively. The previously validated statement about the size – CS formation dependency is not suitable for oxidized NPs. This observation shows that NPs in water is stabilized by hydroxides and favor bigger size as well as reverse CS with iron shell and gold core, indicating a more pronounced impact from the chemical reaction on the final NPs formation. By the addition of acetone to water, stabilization was improved and CS yield increased up to 39 %, confirming the more pronounced effect of the enolates/alcoholates stabilization over chemical reaction favored in pure water. Remarkably, is, however, that although very oxidizing condition, a representative fraction of 6 % (in number) of CS with an iron core and gold shell were generated.

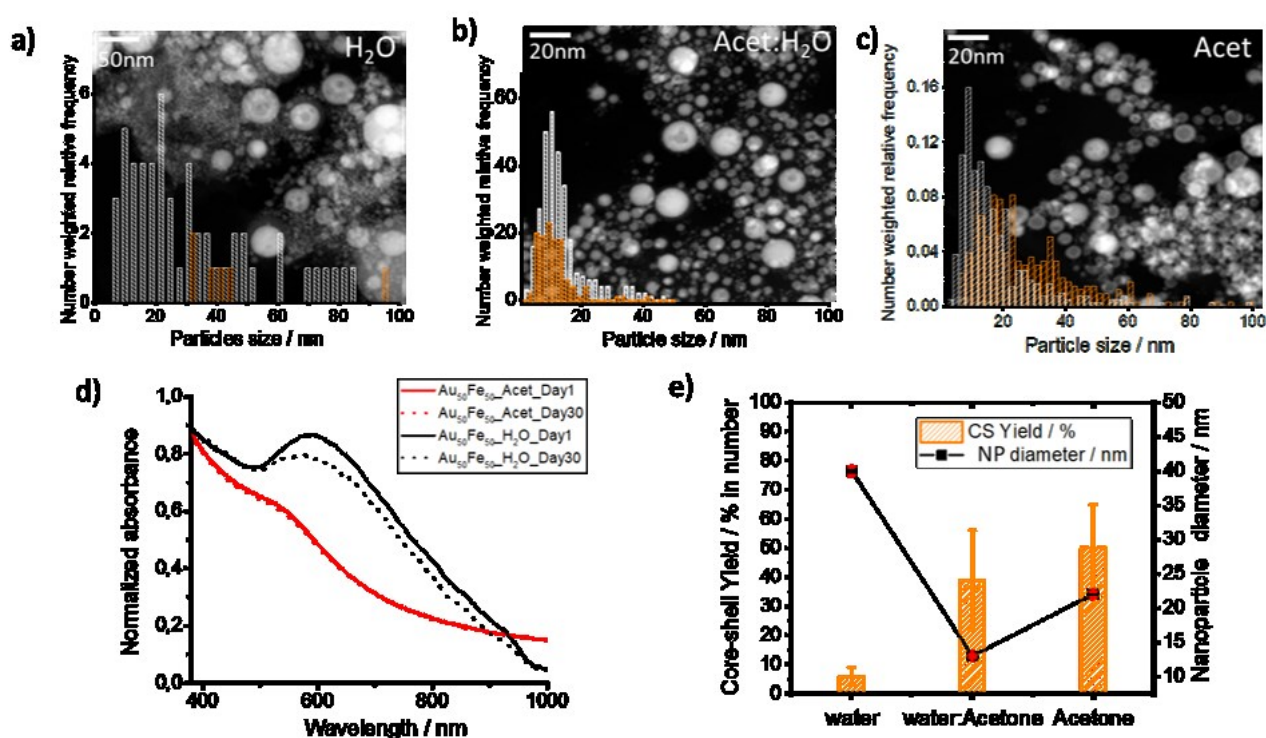


Figure 21: Influence of liquid environment on the Core-Shell yield with representative STEM pictures and number weighted size distribution for Au₅₀Fe₅₀ in a) water, b) water-acetone mixture (50:50%) and c) acetone (Number weighted size distribution for CS (orange bars) and SS (white bars) d) colloidal stability resembled via UV-Vis spectrum for Au₅₀Fe₅₀ in water (black line) and acetone (red line) 1 day after synthesis compared to 30th day e) core-shell yield and mean NP diameter was determined from log-normal function for water, water-acetone mixture, and acetone.

In the following section SS (grey bars), CS (orange bars) and MC (green bars) yield, as well as NPs diameter (SS – grey, CS – orange, MC- green) were summarized for various liquids as shown in Figure 22 a-b. Gold-iron nanoparticles were generated with the representative $Au_{20}Fe_{80}$ NPs by ns-pulse laser ablation in ketones, alcohols, and glycols. Furthermore, water will not be considered here due to highly oxidizing character observed for AuFe systems. In previous studies, in which CS was detected by synthesis via LAL, acetone was used, therefore acetone will be considered as reference. For the comparison reason, Fe rich targets were used owing to the high PS yield (52 % in number) to other AuFe composition as presented in chapter 4.1.3. Moreover, the relationship between the physical parameter of the liquid environment, the size and ultrastructure of the generated NPs were studied. Composition and the NPs size were evaluated with STEM, whereas stability was determined using UV-Vis spectroscopy. PS yield was established by counting > 500 NPs per sample from STEM

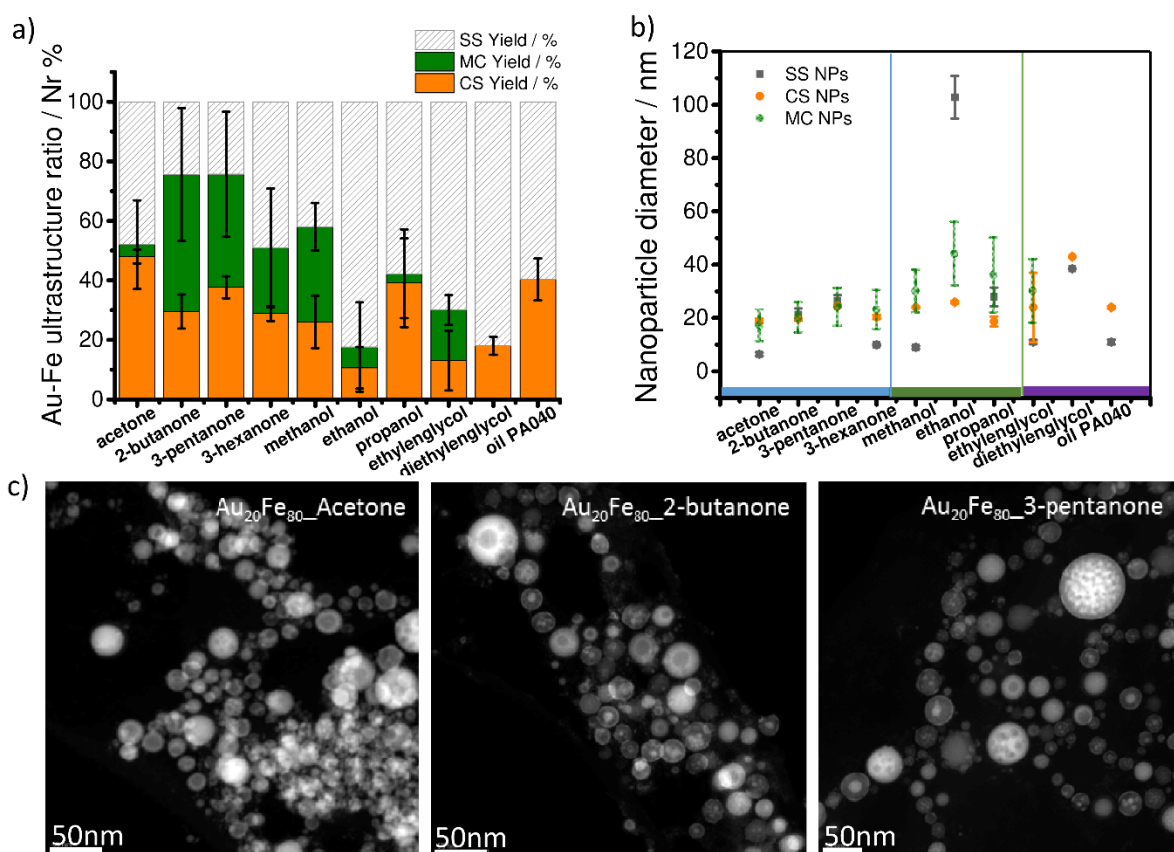


Figure 22: Influence of liquid type on the phase segregation yield for $Au_{20}Fe_{80}$ generated via 8ns laser ablation [3.85 mJ/cm^2 ; 15 kHz], with comparison between a) CS Yield (orange bars), multi CS (MC, green bars) and SS (gray bars), [error bars for SS depicted in Figure S20]. Evaluation of the correlation between the liquid type and particle diameter b) Number weighted median nanoparticles diameter for SS, CS and MC NPs for all analyzed liquids (blue marked area – ketones, green marked areas – alcohols, purple marked area – glycols with polyolefin) - Figure S16, c) 3 representative STEM images for acetone, 2-butanone and 3-pentanone, characterized with increasing MC yield and decrease in shell thickness, respectively.

images. The analysis revealed (Figure 22 a, S15), that the highest phase segregated structures (PS = CS + MC) yield was obtained for the ketones 2-butanone (75,5 % in number) and 3-pentanone (75,6 % in number). At the same time, it becomes apparent that they contained the highest MC yield, > 30 % in number.

Improvement in phase segregated structure productivity has its limits, as the phase segregated yield decreased again for higher ketones, 3-hexanone where only 50 % (in number) were detected, same as for the acetone (52 %). Nevertheless, also here a high amount of MC was present with value at 20% (in number). For comparison, the glycols (ethylene glycol and diethylene glycol) and ethanol showed the lowest phase segregated structure yield, < 30 % (in number). Apart from ethanol, which generated the lowest phase-segregated structure yield (< 20%), alcohols; methanol and propanol generate 60 and 40 % phase segregated structures respectively. Methanol, however, has high MC content, whereas propanol could be a good alternative for acetone, as it contains only a small amount of MC NPs. The low thermal and chemical stability of MC NPs (NPs with one or more iron cores or jellyfish; both are characterized with very thin Au shell) was confirmed in previous chapter 4.3.1-4.3.2. Notably, PAO40 oil (Polyalphaolefin 40), which is characteristic with high viscosity, shows quite moderate CS yield with a generation of 40 % of CS (in number), only 12 % less than acetone. Significantly, no MC NPs were found here, yet harvesting of the NPs generated in highly viscous oils is quite challenging. To sum up, ketones showed the highest phase segregated structure yield, however with a high content of MC NPs, whereas glycols, the lower amount of MC, yet lower PS yield as well. Interestingly, PAO40, showed moderate CS formation, with no MC NPs detected.

In our previous work, we already confirmed a distinctive correlation between the size and the Fe-Au NPs composition[152] and confirmed this experimentally with an extended thermodynamical model (chapter 4.1.1). Two different modes were detected; well-mixed alloy NPs SS and phase segregated core-shell NPs with pure Fe core surrounded by Au rich shell (including a low amount of MC NPs). We could verify, experimentally and theoretically, that smaller NPs with higher Au elemental content would form disordered alloy SS-NPs, while on the other hand phase segregated CS-NPs formed at average diameter >10 nm and Fe at % >35%[152]. Admittedly, we would expect that for NPs with a bigger diameter more CS should be generated, yet

MC NPs were previously considered as CS NPs and not as a separate fraction. This assumption was made based on the very low content of MC (< 5%), which were found only in a few samples for the ablation in acetone. After a detailed analysis of the chemical and thermal stability of the particular ultrastructure, low stability of MC NPs was proven, therefore separate consideration of CS and MC is required.

In the following section, the main focus would be laid on the NP diameters and their correlation towards particular ultrastructures in selected liquids. For this purpose, size distributions were analyzed separately for SS, CS and MC NPs. Representative number mean diameters for particles ablated in different liquids were summarized in Figure 22 b). Mean diameters were acquired from the fitting of the particle size distributions with a log-normal function. In most samples, independent of the liquid environment, a clear distinction between smaller SS and bigger phase segregated NPs was observed. With the exception of 2-butanone or 3-pentanone where the distinction between SS and CS NPs diameter was minimal (21/20 nm and 26/24 nm respectively). Moreover, ethanol and propanol surprisingly showed a smaller mean diameter for CS (26 and 19 nm respectively) in comparison to SS (103 and 28 nm respectively) NPs. In regard to MC NPs, the high similarity in size to CS NPs is observed for ketones (19/17 nm for acetone, 20/20 nm for 2 butanone, 24/24 nm for 3-pentanone and 20/23 nm for 3-hexanone). In the case of alcohol, MC NPs diameter was higher than the CS NPs, 6 nm higher for methanol (30/26 nm), 18 nm for ethanol (44/26 nm) and 17 nm for propanol (36/19 nm). Whereas no MC NPs were detected for diethyl glycol and PAO40 oil. In general, the mean diameter of the generated NPs, varies between 10 and 50 nm, with an exception from ethanol, where alloy NPs with a mean diameter around 100 nm were found. In the group of ketones mean (SS + CS + MC NPs) diameter resembled an increasing trend, starting with 13 nm for acetone and reaching 25 nm for 3-pentanone, only to decrease again down to 15 nm for 3-hexanone (Figure S17). Here, a clear size-composition trend can be observed, where acetone yields 52 % of segregated structures in number, 2-butanone, and 3-pentanone around 75 % in number and then decreases again for 3-hexanone until 50 % in number. Although for alcohols with longer chain length C3-5, stable and smaller NPs would be expected[197, 198], the results showed an opposite effect. Where NPs size first increase from 16 nm (methanol) to 63 nm (ethanol), only to decrease again to 23 nm (isopropanol) as shown

in Figure S19. Moreover, glycol represents high mean diameter with 17 nm for ethylene glycol and 39 nm for diethylene glycol, however, low PS yield.

Contrarily to the thermodynamic prediction towards phase segregation for NPs with size > 10 nm, no substantial increase in PS NPs was observed. This means that a higher number of efficiently stabilized large SS NPs, which are not in thermodynamic equilibrium occurred. The obtained results indicating that next to the NPs composition as well as the NPs size (chapter 4.1.3), the liquid environment plays an important role in ultrastructure control. For ketones, a clear size-ultrastructure trend was validated, whereas more polar liquids like water and alcohols seem to exhibit strong liquid effect not predicted by the simple theoretical calculations, which only consider the elements free surface energies.

To better elucidate the effect from physical properties of the liquid environment on the PS productivity, radar chart with phase segregated (CS + MC) NPs yield in dependency from chosen liquid parameter (surface tension, refractive index, density, heat capacity, and viscosity) were plotted. The impact on the phase segregation yield for all parameters was evaluated separately and is depicted in Figure 23 b-d. Overview of all considered parameters is summarized in a radar chart in Figure 23 a.

As expected, glycols with the lowest CS yield (below 30% in number) showed clear deviation from the other liquids (Figure 23 a) with the biggest variation for refractive index (RI), surface tension (ST), density and viscosity. Remarkably, for PAO40, which also resembled low 40 % (lower than acetone 52%) CS yield, RI, surface tension as well as viscosity deviation is observed. Interaction of the refractive index and the laser intensity may play a crucial role during LAL; this process is known as the self-focusing Kerr effect. This leads to a shortening of the focal distance, as a liquid would act as an additional collecting lens, decreasing productivity[20]. However, this effect applies only for very short pulse duration, where high peak power can be reached, therefore it will not be discussed here. Nevertheless, based on the results summarized in Figure 23 b, no apparent trend can be concluded. Surface tension on the other side may impact the nanoparticle growth by suppressing small cavitation bubble. As shown in Figure 23 a, for NPs generated in liquids with high surface tension (> 30 mN/m) low PS yield (lower

than for acetone 52%) was observed e.g. for glycols and PAO40 oil. Interestingly, for glycols average diameter was above 10 nm, indicating negligible quenching effect. Unfortunately, no clear surface tension - PS yield trend can be observed, as the lowest PS yield was for ethanol with low surface tension (below 25 mN/m) and at the same time for glycols with high surface tension (above 40 mN/m). Moreover, even though for lower surface tension values, more PS NPs were detected, still no correlation between surface tension – PS yield is apparent (ketones – high PS yield; alcohols – low PS yield for similar surface tension values). Based on the van der Waals model, pressure inside the cavitation bubble is proportionally dependent on the surface tension of the liquid[199]. Meaning, that if surface tension is high the pressure inside the cavitation bubble will be high as well. Yet, surface effect showed a negligible influence on the cavitation bubble lifetime, whereby comparison of alcohols and water, density[200] or more likely the ablated material thickness and laser pulse parameters[201] resembled a more pronounced impact on the cavitation bubble lifetime. In general, Amans et al. and Lam et al. showed that surface tension and viscosity can be neglected during the first cavitation bubble cycle[200]. On the other side, remarkably next to high surface tension values, glycols and PAO40 oil resemble high viscosity ($< 20 \text{ mPa}\cdot\text{s}$) as well. The effect of the viscosity on the NPs formation will be discussed in the following section.

Among all investigated parameters, viscosity appears however to have the biggest impact on the NPs morphology (Figure 24 d, f). Interestingly, ethylene glycol with a viscosity above $10 \text{ mPa}\cdot\text{s}$, was characteristic with displaced iron core (Figure 24 d). Whereas, highly viscous liquid (above $40 \text{ mPa}\cdot\text{s}$) contributed to the formation of non-spherical NPs. Remarkably, as shown in Figure 24 f, PS yield decreases up to diethylene glycol with increasing viscosity with an exception for ethanol. In addition, contrarily to observed trend in which PS yield decreases if viscosity increases, a slight increase for PAO40 was observed (up to 40%) as shown in Figure 24 f. However, not only the PS yield changed but also a spherical character of the NPs as seen in representative STEM images in Fig 24 d. Ablation efficiency is enhanced when the viscosity of the solvent increases, due to improvement of the plasma plume confinement on the ablated crater or due to slowed down dynamics of the cavitation bubble. Furthermore, high viscosity impacts the collision rate leading to the formation

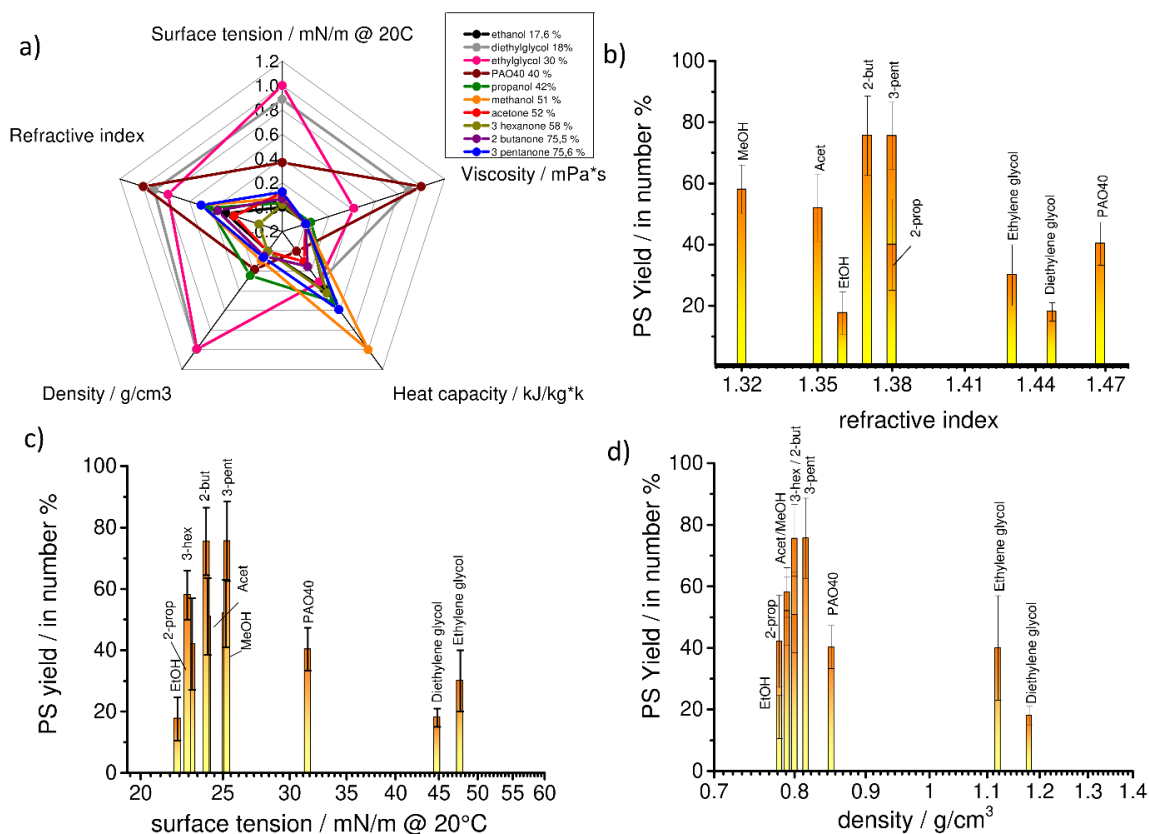


Figure 23: a) For the evaluation of the liquid environment effect on the AuFe morphology, an overview of the chosen parameters (surface tension, refractive index, density, viscosity, and heat capacity,) was prepared in form of a radar chart. Influence from the liquid environment on the generation of the phase-segregated phase was summarized as a function of the following parameters; b) the refractive index, c) surface tension, d) density. The evaluation focused on the 3 representative groups of liquids, alcohols, ketones and highly viscous liquid (glycols and PAO40 oil).

of small particles and may reduce aggregation[202]. Additionally, with higher viscosity, smaller NPs would be expected due to a decrease in cavitation bubble lifetime as shown by Chrisey group[203]. Remarkably, no clear size-viscosity trend can be observed (Figure S21 a), yet by excluding PAO40 oil, with increasing viscosity lower PS yield is noticeable (Figure 24 f). One must not forget that not only one parameter defines the ultrastructure but a mixture of several factors, where one parameter may show a more pronounced character over the final NPs structure. It's instructive at this stage to illustrate that the final statement can not be made based only on the evaluation of the early stage of the ablation of plasma plume lifetime. From a theoretical point of view, it is difficult to predict the exact transformation of the NPs up to its final state. In regard to ketones (acetone, 2-butanone and 3-pentanone), a clear correlation between PS yield and the heat capacity can be observed (Figure 24 e). Notably, with increasing heat capacity values, higher PS yield was observed. Representative STEM

images confirming the trend are shown in Figure 24 d. Then again 3-hexanone showed lower PS yield, even though it contains higher heat capacity value (Figure 24d,e). Admittedly, Kanitz et al. showed no significant plasma shape change with variation of the heat capacity of the liquid (water, acetone, and toluene), yet weaker plasma is distinguishable for organic solvents[204]. Moreover, Waag et al. reported on how the temperature of the ablated target as well as the colloid may impact on the NPs productivity. In his study, he proposed that low productivity can be contributed to the organic solvents, which have a lower heat capacity and higher viscosity[205].

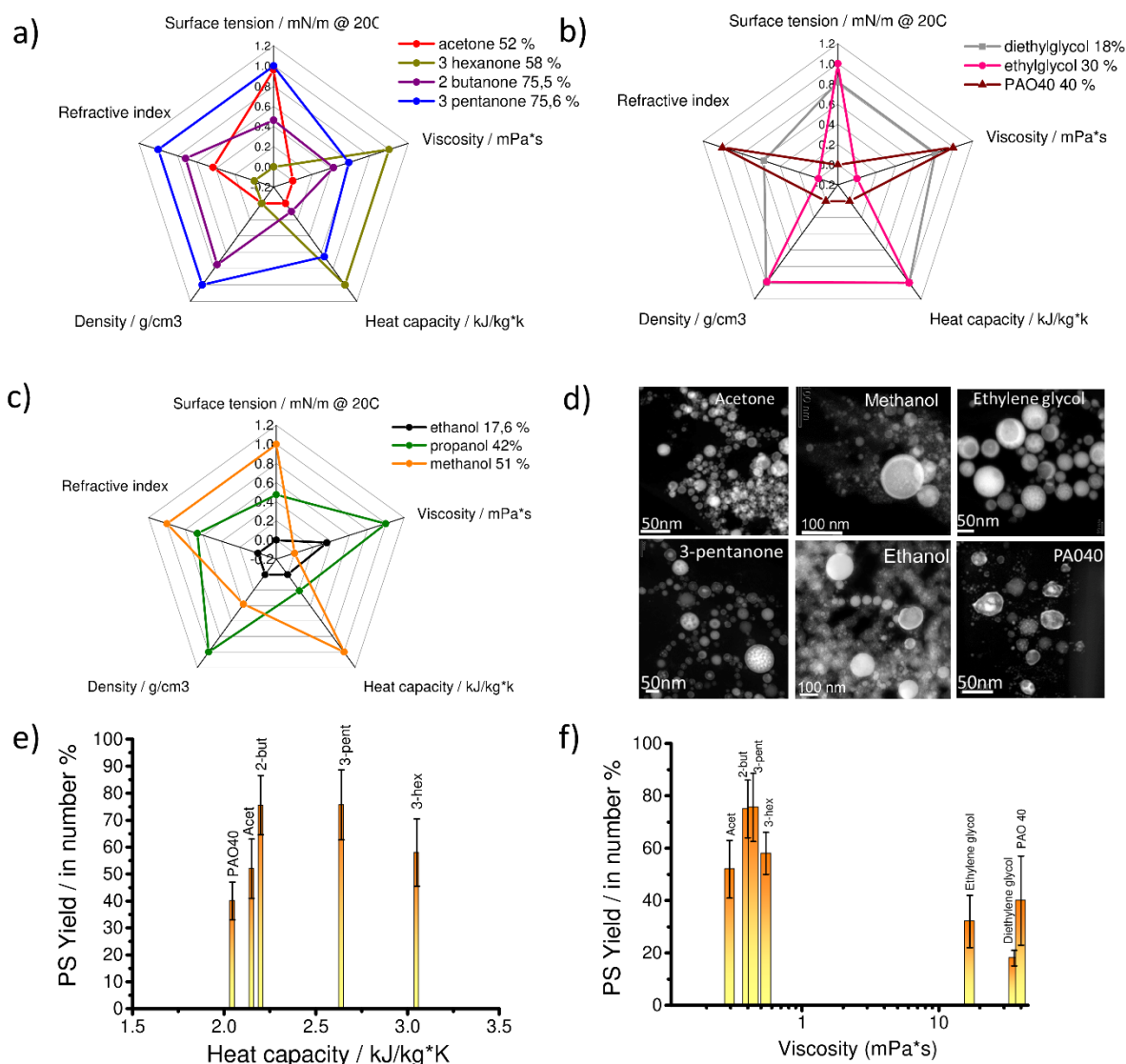


Figure 24: Overview in form of radar chart, summarizing the impact from the chosen liquid parameters towards high PS yield, shown separately for 3 groups of liquids a) ketones, b) glycols (with PAO40 oil) and c) alcohols, along with d) changes within the morphology for Au₂₀Fe₈₀ NP in dependency from the liquid type used during ablation is shown as representative STEM pictures. Finally, dependency from the PS yield from e) heat capacity and f) viscosity for e) acetone, 3-pentanone, and f) Ethylene glycol and Polyolefin (PAO40) generated via 8ns short pulse by LAL is given.

The only possible explanation coming to mind would be that heat capacity may influence the solidification process of the ablated material and recondensating in the liquid. Nevertheless, due to lack of experimental or theoretical data this prediction can not be confirmed. Despite the lack of explanation, there is indeed a relation between an increase in heat capacity and PS for ketones (acetone, 2-butanon and 3-pentanone) with an exception for 3-hexanone. Thus, based on the available data statement can be made in which the results indicate that higher heat capacity value may favor the formation of the segregated phase, yet only to a certain point. Nevertheless, up to date, this can not be explained.

In summary, up to date no clear trend between one chosen laser parameter and PS yield can be made. The most pronounced impact from laser parameters was viscosity and heat capacity. Interestingly, with increasing viscosity, PS yield decreased, indicating that plasma plume confinement or slow bubble dynamics does not favor PS formation. On the other side high heat capacity, which may affect the cooling and solidification process, not only improved CS yield but also the generation of MC NPs.

In the last section of this chapter, the NP size distribution for evaluated liquids will be summarized. The size distribution is described by the dimensionless parameter which is characterized by the PDI value. The polydispersity index (PDI) was calculated from the resulting x_c -value and the standard deviation w^2 of the distribution[21]. Polydisperse index (PDI) with a value below 0.3 represents narrow size distribution (monodisperse), while higher values represent broader size distribution (polydisperse). In Figure 25 overview of the size distribution is shown with two representative size distribution for narrow size distribution in acetone in Figure 25 b and wide size distribution in methanol Fig 25 c. In comparison, narrow size distribution can be found for ketones (PDI well below 0.3), while glycols and alcohols lead to a broad size distribution with a PDI > 0.3 (Figure 25a, S19). Here again, ketones show the most promising liquid for LAL, with the narrowest size distribution. When the size distribution is wide, additional extraction techniques would be required. For most of the applications, the size is an important factor especially for catalysis or biomedical application where the high surface of the NPs is required either for an electrochemical reaction or bio-conjugation.

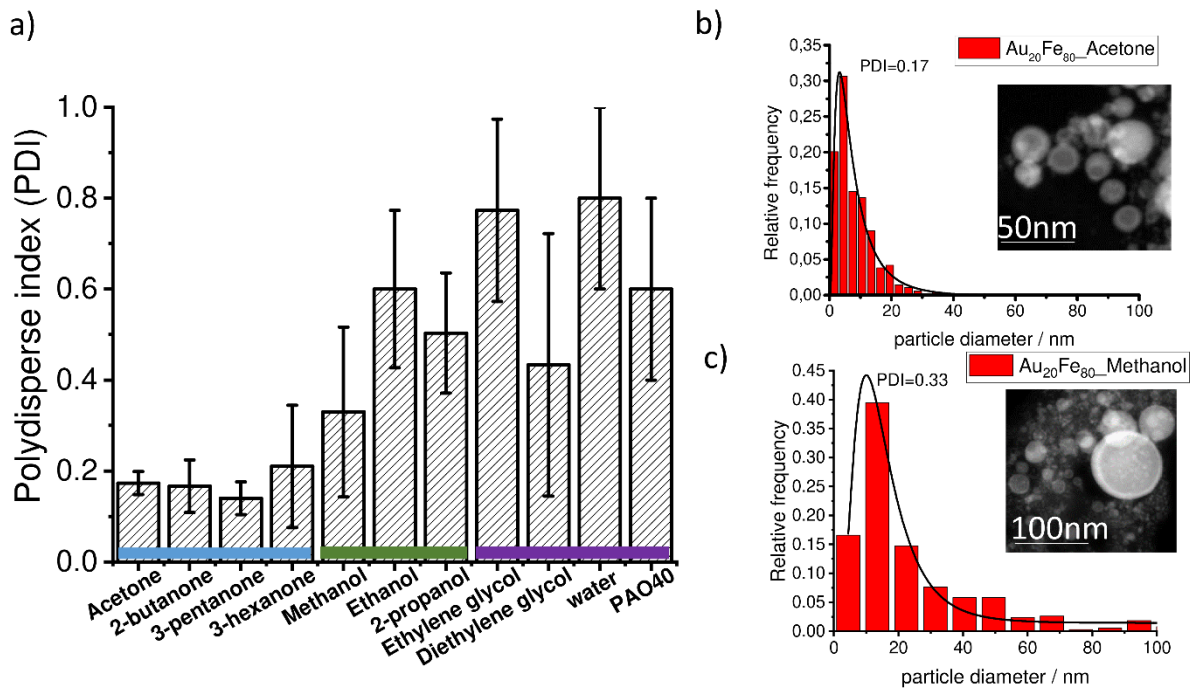


Figure 25: a) Evaluation of the size distribution described with polydispersion index (good stability > 0.3) for representative ketones (marked blue), alcohols (marked green) and glycols (marked red) and additional liquid water and polyolefin PAO 40 (marked yellow); Two representative number weighted size distributions for Au₂₀Fe₈₀ generated in b) acetone, c) methanol via 8 ns laser and respective STEM images are shown.

In summary, ketones showed by far the highest PS yield, with the lowest size distribution and optimal colloidal stability. Acetone is the most promising as it has the lowest amount of MC, low PDI, and sufficient colloid stability. Large efforts are devoted towards the controlled synthesis of defined ultrastructure and the size, however, the limitations in the theoretical simulation field, as well as limited experimental data, hinders understanding of the liquid impact. The biggest drawback is the investigation of one parameter in a controllable way. Consequently, an overview of liquids favoring CS formation for Au-Fe systems was prepared. Furthermore, the knowledge may also be applied for the systems with similar properties as a gold iron system.

4.3. Characterization of the AuFe ultrastructure

As shown in the previous chapter, independently from the conditions during the LAL synthesis, alloy and phase segregated structures are generated. In this chapter, questions regarding chemical and thermal stability of thus ultrastructures will be addressed. In order to achieve a complete and detailed overview of microstructural change, in-situ and ex-situ approach will be applied.

4.3.1 Chemical stability of Au-Fe NPs

To evaluate the chemical stability of the various ultrastructure's, etching of Au-Fe NPs with various ultrastructures under acidic conditions (with various HNO_3 concentrations) were performed and reported by Marius Kamp et al[206]. Different ultrastructures were investigated via transmission electron microscopy (STEM) to assess any changes within the composition and the ultrastructure of the Au-Fe NPs. Representative NPs before and after etching treatment are shown in Figure 26.

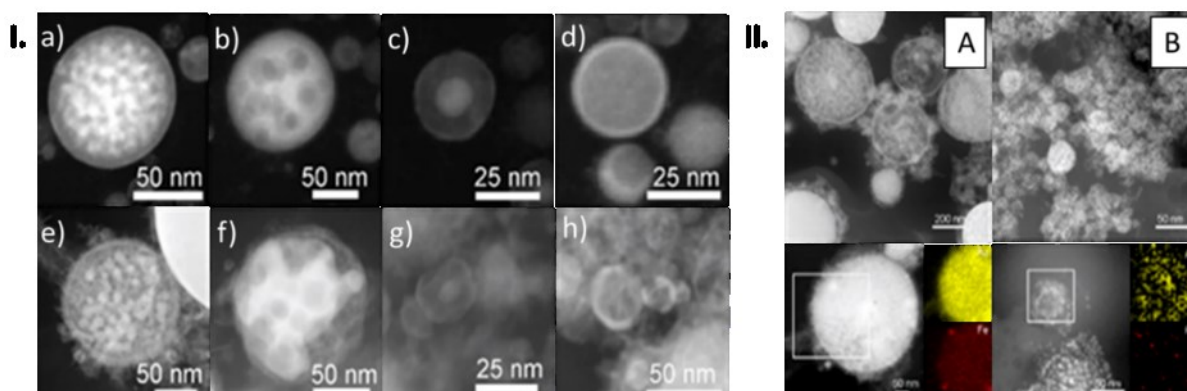


Figure 26: I. Chemical stability of the particle structure evaluated by the elemental distribution for various morphologies of representative $\text{Au}_{20}\text{Fe}_{80}$ composition with a-h) STEM analysis before and after etching with conc. HNO_3 II. Elemental distribution driven from EDX mapping determined for etched A. $\text{Au}_{20}\text{Fe}_{80}$ and B. $\text{Au}_{50}\text{Fe}_{50}$ NPs[206].

The NPs with average composition $\text{Au}_{20}\text{Fe}_{80}$ showed four different ultrastructures, namely solid solution, multi core-shell, jellyfish and core-shell, respectively. This variety is representatively shown in the form of STEM images depicted in Figure 26 I. a-d. For the illustration, selected images were compared before and after etching treatment as shown in Figure 26 a-d and identified with Z-contrast images (Figure 26 e-h). Remarkably, preservation of the initial template morphologies occurred despite the

treatment under acidic conditions, resembling good mechanical stability. In particular, the degree of the porosity for both elements was considered an important aspect characterizing the stability of the NP. Briefly, the higher Au concentration, as well as low porosity grade, resulted in brighter contrast. Interestingly, the data gathered in Figure 26, where iron core showed lower contrast, suggests higher porosity of the NP. This effect originates from the generation of voids and the formation of oxides. Moreover, Z-contrast SEM analysis was performed to establish the amount of Fe removed during the etching treatment. After etching, independently from the samples very low Fe content (only ~ 5 at%) was found in the nanoporous Au. Remarkably, even a thin Au shell preserved its shape after the etching procedure. There seems to be a compelling reason to argue, that Fe was leached through permeable Au shell, via pinholes, which are shown in Figure 27 (pinholes marked as asterisks in Figure 27 a and b). One remarkable consequence is the possibility of porosity control by simply adjusting the acid concentration. The result in Figure 27 h-j validated that statement in which 0.1 M led to the dissolution of a small amount of Fe (low porosity), 6 M to moderate Fe dissolution, whereas concentrated nitric acid led to full Fe dissolution (high porosity, Figure 27 e-h; ii).

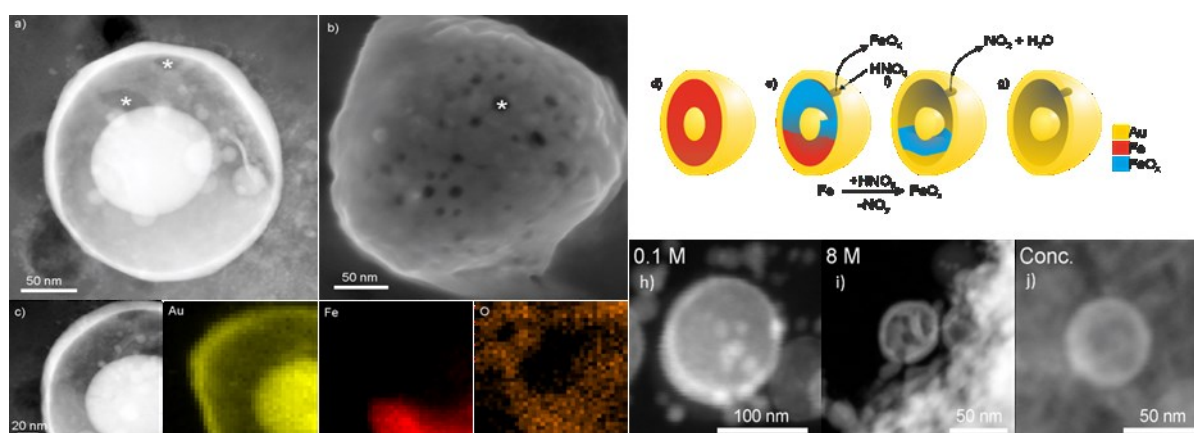


Figure 27: Chemical stability of the core-shell morphology determined with Z-contrast STEM image of an etched MCS NP at tilting angle -31° a) STEM image of an NP with pinholes b) STEM image of the same MCS NP at tilting angle of 17° and EDX elemental maps of Au-M, Fe-K and O-K are shown. In d)-g) the formation mechanism of dealloying is described by a simplified reaction scheme[207]. h-j) Exemplary Z-contrast images for different acid concentrations (48 h). From left to right the acid concentration (0.1M;8M, concentrated) used and the degree of dealloying increases, dealloying with concentrated nitric acid results in almost complete dissolution of the Fe core[206].

Furthermore, the Fe shell inside the NP was partially dissolved with Fe oxide present, as confirmed by EDX mapping (Figure 27 c), where Au (yellow), Fe (red), and O (orange) are present. This confirms our prediction that Fe can dissolve through the

pinholes as no Fe oxide was found in CS NP before the etching procedure (Figure S2). During Fe dissolution, the stabilization of ultrathin Au shell walls is suggested to occur due to the Kirkendall effect (Figure 27 d-g). Here the oxidation process in which species are traveling inside the NPs much faster, contrary to the diffusion of metals atoms to the outer parts, allowing preservation of the morphology[208]. Summarizing, galvanic dealloying was followed by the Kirkendall effect, favoring stabilization of the NP. Crystallite size investigated after etching (via electron diffraction), showed that reduction in the reflection width can be correlated with increasing crystallite size in the sample (Figure 28 a-b). Moreover, an electron diffraction pattern for two representative samples $\text{Au}_{20}\text{Fe}_{80}$ and $\text{Au}_{50}\text{Fe}_{50}$ is shown in Figure 13 a-b. Based on the available data it can be concluded that porous NP (Figure 28 b) showed characteristic diffuse intensity on concentric rings. Contrarily to $\text{Au}_{20}\text{Fe}_{80}$ sample (Figure 28 a) in which an increase in diffuse intensity was observed, indicating the decrease of the NPs crystallinity. Thus, there is indeed a relation between the crystallinity and the amount of Fe available in the NP, as the Fe content present in the NP is in direct correlation with the porosity degree of the NP.

In the last paragraph, the shift of reflection positions in comparison to bulk Au (horizontal dotted lines), as well as the intensity of the concentric rings' distribution will be discussed (Figure 28 c). The generic shift and mismatch lattice spacing can be correlated to low coordination surface sites and lattice strain. From the literature, a decrease of lattice spacing in NPs in comparison to bulk was reported[209]. These findings indicate enhanced electrochemical activity towards, for example, catalytic applications[208, 210, 211].

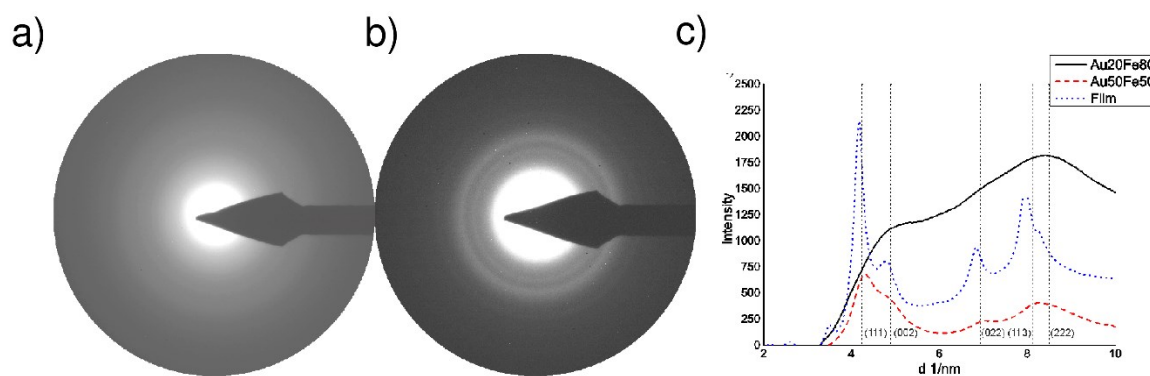


Figure 28: Electron diffraction pattern of samples after etching treatment for a) $\text{Au}_{20}\text{Fe}_{80}$ and b) $\text{Au}_{50}\text{Fe}_{50}$ NPs c) The rotational average reflection intensity of the respective electron diffraction patterns (dotted vertical line for Au bulk reflection)[206].

To summarize, the porosity of the NP can be controlled by variation of Fe content or acid concentration. Even though iron can be removed through the leaching procedure, by simply adjusting the acid concentration, stabilization of the Au shell is remarkable. Gold shell iron core structure is stable with acid treatment up to < 0.1 M nitric acid. Moreover, such an approach delivers an easy way to control a surface composition and porosity degree, which can be directly applied in catalysis.

4.3.2 Thermal stability of AuFe NPs

Aiming for a better understanding of the formation mechanism of Au-Fe NP, it is important to characterize their equilibrium morphology and the possible metastable structures. In this regard, thermal stability tests were performed and reported by M. Kamp et al.[212] The thermal stability was investigated using an in situ STEM heating experimental set up with a Gatan 652 double tilt heating holder. The reliable and stable temperature measurement was confirmed in previous studies[213]. During this test, the heating rate was 10 °C per minute, where at chosen temperatures the temperature was held for 10 minutes[214]. Two representative compositions were chosen, Au₅₀Fe₅₀ (42% CS per number) and Au₂₀Fe₈₀ (62% CS per number), as in both cases CS and SS ultrastructure were present. The in-situ analysis was complemented with the ex-situ electron tomography evaluation.

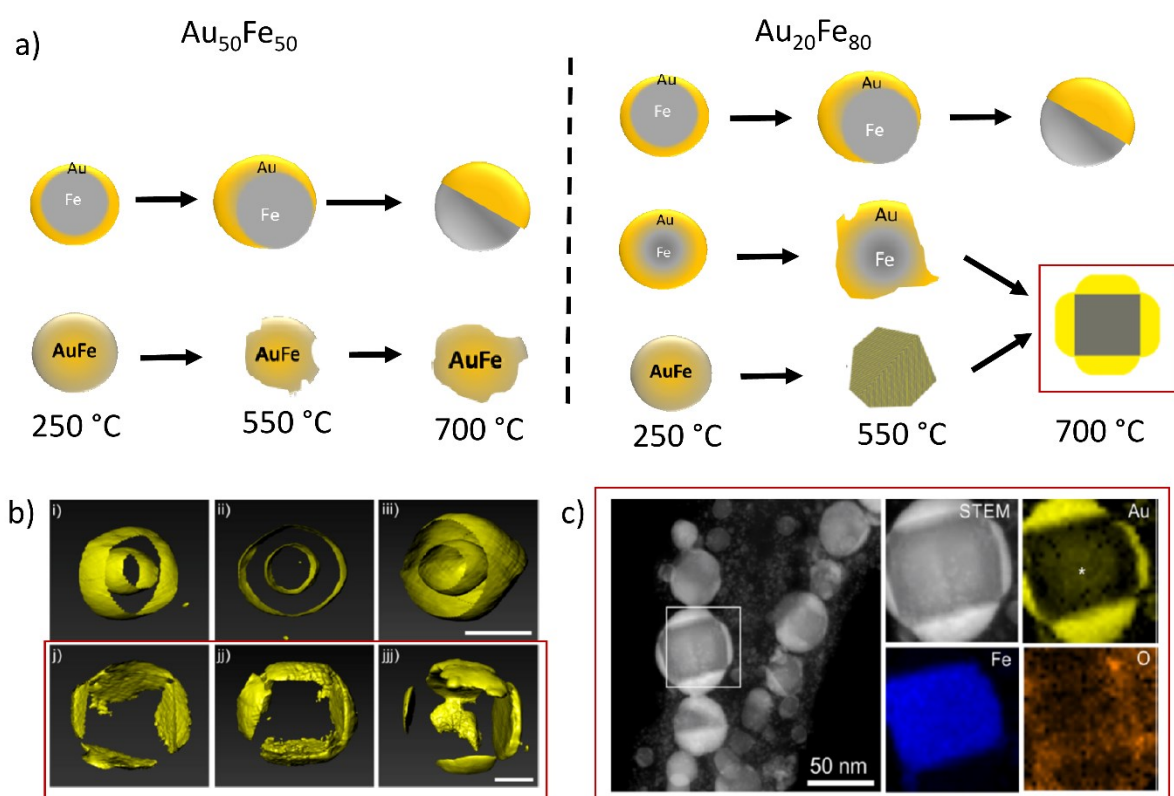


Figure 29: a) Schematic representation of two representative compositions, namely Au₅₀Fe₅₀ and Au₂₀Fe₈₀ NPs (with STEM-EDX analysis presented in Figure S1) b) Schematic tomography reconstruction of isosurface before heating at 20 °C and after heating (700 °C) c) EDX elemental mapping and STEM pictures of tetrakis hexahedron structures after heating treatment of 700 °C.[212]

The schematic overview for NPs transformation at the chosen temperatures during in situ STEM experiment is shown in Figure 29. The stability of representative, SS, CS with a thin shell and CS with thick shell were evaluated in temperature window from 0°C to 700°C. In all cases, CS NPs were thermally stable up to 250°C. In the case of Fe rich $\text{Au}_{20}\text{Fe}_{80}$ CS NP (with thick shell), a transformation occurred into Fe rich core cube-shape faceted by truncated Au rich pyramids with intermediate lamellar structures. Tetrakis hexahedrons structure were previously reported in the literature, e.g. Langlois et al.[147], reported synthesis via physical vapor deposition at 800°C, of equilibrium morphology with Fe cube, capped with the truncated Au pyramids (tetrakis hexahedrons), same as in case of iron-rich CS NP reported in this work (Figure 29 b). Minimization of the interfacial energy as a driving force was proven by the interface analysis via TEM, which indicated epitaxial growth of Au and Fe cube along [001]. Furthermore, 3D tomography reconstruction model, together with the elemental mapping confirmed the symmetric arrangement and the planar interfaces of the tetrakis hexahedron ultrastructure as predicted by Wulff's[215] (Figure 29 b). For tomography tilting series, a high angle tilting holder was used with applied maximum tilt angles of 65° to reduce artifacts from missing wedge[216]. Representative STEM images along with EDX mapping (Figure 29 c) confirmed the tetrakis hexahedron structures after annealing up to 700°C towards thermodynamically stable CS NPs, as predicted by Casanove et. al[217]. A clear distinction between the gold (yellow) shell and iron (blue) core can be observed in Figure 29 c. Noteworthy is, however, the intermediate state of lamellar morphology, based on the alternating Au rich and Fe rich stripes, with a large interface area as confirmed by Z-Contrast. Unfortunately, with available TEM technique more detailed information about phase segregation are simply not accessibly. Hence, Amram and Rabkin et al.[166] reported lamellar spacing of 200 nm, by Au-Fe bilayer heating procedure, indicating strong dependency from the size and the NP composition. On the other side CS with thinner Au shell (< 5 nm), for $\text{Au}_{50}\text{Fe}_{50}$ and $\text{Au}_{20}\text{Fe}_{80}$, transformation into a biphasic final structure was observed (Figure 29 a, S21). One remarkable contribution here is the elastic energy increase with reduced shell thickness, making Janus biphasic ultrastructure energetically more favorable, due to the minimization of the interface area between Au and Fe. Interestingly, Casanove [217] et al. showed that the shell thickness does not contribute to the overall NPs stability like in the case of another system, for instance, Ag-Cu. Interestingly, our

results showed that the Au shell thickness defined the NPs stability and led to the formation of the biphasic final structure at 700°C (Figure S21). This leads to the conclusion that the thicker shell is required to improve the stability of the CS NPs.

All things considered, it may be concluded, that during a heating experiment, equilibrium structures were generated at 700°C. The hypothesis was rationalized, by the controlled experiment in which morphologies retained their transformed equilibrium structures after cooling them to room temperature.

To summarize, the results of in-situ experiments delivered a new understanding of the formation mechanism of Au-Fe NPs during LAL, its thermodynamic stability as well as temperature-dependent transformation. The metastable character of AuFe NPs synthesized via LAL and their stability up to 250 °C is underlined by the results presented. Hence, the transformation towards a stable morphology in equilibrium is strongly affected by the NPs composition and size. Remarkably, shell thickness contributes towards overall NPs stability, where with thicker shell higher stability can be achieved.

4.4 Formation mechanism proposal for AuFe system.

Producing colloidal nanoparticle through laser ablation in liquids has become a popular technique to synthesize binary alloy NPs. In contrast to chemical synthesis, in which NPs with clean surfaces and particular structures are not accessible. Nevertheless, control over various ultrastructures in the context of harvesting the relevant properties is still challenging during laser ablation synthesis. For instance, the basic mechanism during nanoparticle formation is up to date still not fully understood. In this context, the model of the nanoscale phase diagram enriched by simple thermodynamic calculations and experimental approach for binary AuFe system has been implemented towards a better fundamental understanding of the laser ablation mechanism. A phase diagram was used, to gain more insight into possible equilibrium state of the AuFe NPs, by complementary calculations considering NPs composition, size and minimization of their surface energy as described by Gibbs[189]. As a result, NPs synthesized during LAL were suggested to be in non-equilibrium alloy phase, indicating a kinetically controlled process[152]. Admittedly, an approach based on the nanoscale phase diagram allows the prediction of NPs composition and its possible ultrastructure, yet certain conditions such as liquid environment or laser parameters are not considered. Briefly, in aim to control the generation of particular core-shell morphology, conditions during laser ablation had to be established through systematic experimental study, as summarized in chapter 4.2. Therefore, within this chapter, parameters towards the highest yield of the AuFe core-shell structure are highlighted, as this particular morphology contains a combination of magnetic, plasmonic properties[27] as well as the possibility to functionalize the NPs surface through Au-thiol chemistry[218]. Finally, the formation mechanism of AuFe NPs during LAL, was validated according to results presented in chapters 4.1.3-4.3, and summarized in form of a schematic model as depicted in Figure 30.

This paragraph aims to elucidate a final correlation between the target (Au:Fe molar ratio), liquid environment (heat capacity, length of the chain and viscosity) and NPs formation mechanism during laser ablation in liquids. In previous chapters (4.2-4.3), it was shown, that independently from the target composition bimodal particle size distributions were present, as predicted by Zhigilei et al.[137] In the case of Au rich targets, only SS NPs were found. Whereas for iron-rich targets, size distribution with

larger core-shell particles and smaller solid solution nanoparticles were detected. Furthermore, the formation of core-shell nanoparticles was not probable in particles < 10 nm, if BCC phase was not present. The diameter of the NP and its correlation to either alloy or segregated phase was determined via simple thermodynamic calculations[136], in which element segregation was shown to be oriented based on the minimization of the surface and interface energy. Remarkably, CS yield can be controlled by adjusting Au:Fe molar ratio in the target used for the ablation, whereas with increasing Fe content, higher CS yield can be achieved. To improve the CS yield even further alloy ($\text{Au}_{50}\text{Fe}_{50}$) thin multilayer targets were proposed, allowing the generation of > 90 % of CS NPs without changing the 50:50 NPs composition. Here, both target geometry (more precisely thickness), as well as pulse duration (ns long pulse duration), affects the final NPs composition. In the case of short ps pulse duration metastable SS NPs are favored, contrarily to long ns pulse duration, where CS yield reaches almost unity. Therefore, to reach high CS NPs yield an alloy thin multilayer target is proposed.

The last considered parameter was liquid surrounding, where heat capacity, chain length and the viscosity were taken into consideration. Here, it is important to mention, the difficulty of constant parameter change within one group of liquids. Therefore, liquid property – CS yield relation cannot be delivered here. Consequently, the overview of 3 groups of liquids with the impact on the CS yield was summarized. In general, CS formation is possible independently from the liquid environment. Whereas, next to methanol only 2-pentanone and 3-pentanone showed higher CS yield in comparison to acetone. CS yield improved only by several percents, however, the amount of Multi core-shell NPs also increased, which resembles low thermal and chemical stability as shown in the chapter (4.1.2). The most promising parameters toward high Au-Fe CS yield, are summarized schematically in Figure 30. Based on these findings, it can be summarized, that well-mixed iron-rich alloy thin targets lead to high yield of CS NP, if ablation occurs at long ns pulse duration in acetone.

Since a more refined approach toward the understanding of the formation mechanism is required, the liquid environment will not be considered for the mechanistic model. The lack of the verified trend between CS formation and the clear physical parameter is apparent. In this regard, only pulse duration (long ns and short ps duration) and

target alloy or layered target) during the mechanistic model of the formation mechanism proposal will be addressed.

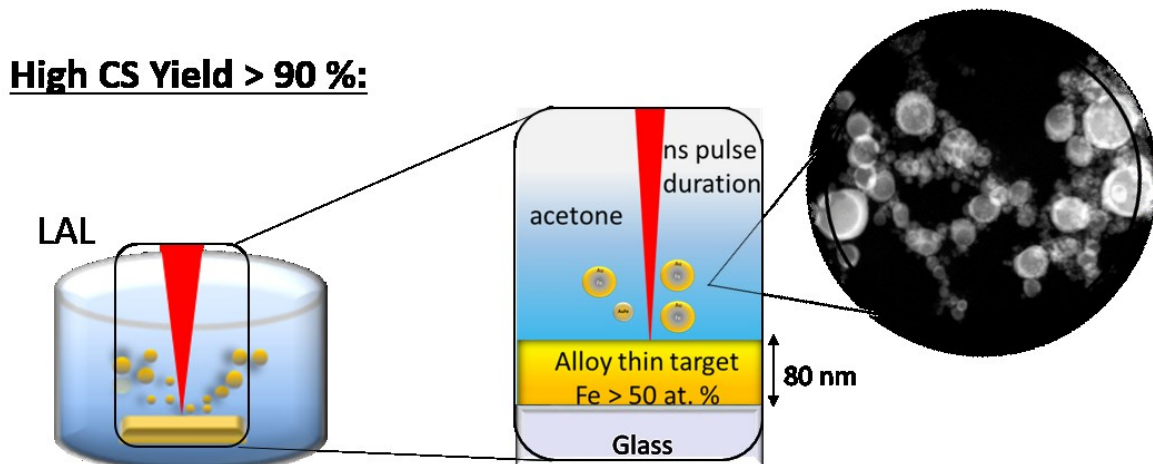


Figure 30: Schematic overview of the relevant parameters towards high AuFe core-shell yield generated via laser ablation in liquids.

To gain more insight into the NP formation mechanism, the complexity of the ablation mechanism should be considered. Namely, ablation for long ns and short ps pulse durations depicted schematically in Figure 31 a. Notably, bigger NPs diameter was observed during long ns pulse duration (Figure 15). This effect arises from the fact that both pulse durations are characterized with different ablation mechanism[153]; during long ns pulse duration, melting and vaporization occurs[103] whereas ps short pulse duration can be described as almost instantaneous solid-vapor transition of the atoms of the target[138]. One remarkable consequence of the influence of the pulse duration is for instance effect on the CS yield as shown in chapter 4.2.1. Notably, long ns pulse resembled high CS, > 90 % in number if alloy 80 nm targets were used. Owing to prolong time inside the cavitation bubble under heated state (> 5000 K)[139, 140]. Prolong cavitation bubble lifetime arises from the prolong plasma lifetime, which results from the additional heating of the plasma, due to partial overlap of the pulse width and the duration of the existing plasma plume[103, 138]. Increased lifetime of the cavitation bubble by application of larger pulse energy was reported previously by Park et.al[108]. Concerning the impact from the cooling rates, which in gas phase is lower than in the liquid phase[108], a statement can be made, that NPs in CB during ns pulse ablation have more time to reach their thermodynamic equilibrium. On the other side, NPs generate during ps are form far from the thermodynamic equilibrium and alternatively,

NPs can be formed as metastable structure if the NPs will be kinetically trapped e.g when atomic diffusivity would be rapidly frozen[219]. In case of ps, NPs will be cooled more rapidly by being exposed to the liquid phase, as their CB lifetime is shorter[155]. This phenomenon is proposed schematically in Figure 31 b, in which CB size corresponds to the lifetime period, the longer the lifetime the bigger the size of the CB. Considerable attention must be paid to the fact that SS NPs are present independently from the conditions applied. Povarnitsyn et al. proposed based on the simulation, that

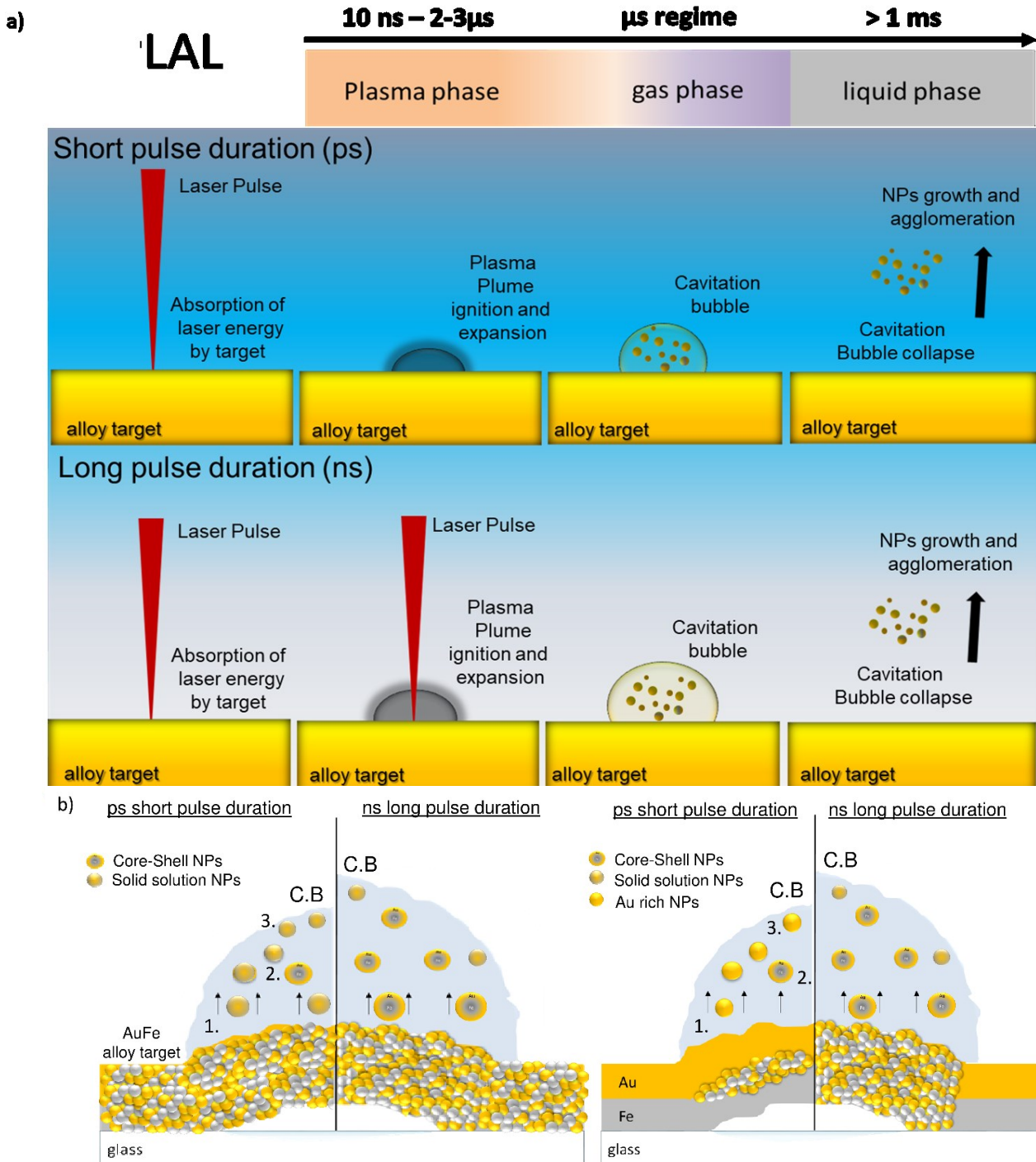


Figure 31: Schema of the mechanistic model for a) the AuFe formation mechanism during laser ablation in liquids for short ps and long ns pulse duration, b) for NPs generated for alloy target (*) c) and generated via fully separated layered target.

smaller NPs are formed in the liquid gas region (Figure 31 b-3).[141]. Notably, in accordance with thermodynamic calculations smaller NPs < 10 nm, are more thermodynamically favored in SS configuration. Whereas, the larger NPs are formed in the molten layer (Figure 3 b-2) region, therefore here CS morphology would be favored (> 10 nm; chapter 4.1.3). This hypothesis may be confirmed by Zhigilei

et al. simulation in which he proposed, that within the CB different regions can be assumed to be incubators delivering different conditions towards NPs diameter formation[104]. Moreover, this statement is further confirmed by the observation made in chapter 4.2.1, in which for fully separated layered targets during ps short pulse ablation, limited mixing of topmost layer resulted in the formation of almost pure Au NPs (Au rich NPs with only a few % of iron). In addition, only several representative CS NPs were found in this sample. Au rich NPs, are most likely generated in the liquid + gas phase region (Figure 31 c-3), whereas CS are in the region closer to the molten layers (Figure 31 c-2). Nevertheless, low CS yield can be verified by the short relative CB lifetime, hindering the full transformation of the NPs towards the equilibrium phase. In the case of long ns pulse, no simulation is available, however, based on the experimental approach conclusion can be drawn, that during ns long pulse, mixing in the early stages of the ablation is more apparent in comparison to the short ps pulse duration. Moreover, a higher yield of CS validated these predictions. At last, SS fraction, which is present in all ablated samples, further confirms the prediction of NPs formation- region dependency. Meaning, that within the CB, the formation of the NPs is depending on the duration but also the condition in particular regions of the CB. It can not be forgotten, that this formation mechanism considers only early stages of the ablation, in which simulation is not able to predict neither long ablation nor later stages of the ablation e.g after bubble collapse. After bubble collapse, the reset of the formed NPs morphology may occur and undergo not described here transformation/formation process. Nevertheless, a clear correlation between simulation and experimental data may contribute towards a fundamental understanding of the AuFe NP formation mechanism.

To summarize, the careful choice of pulse duration will impact different ablation mechanism, in case of short ps pulse ablations, metastable kinetically trapped product will be synthesized, especially if they are generated from fully separated layered target. Thus, well-mixed target contributes towards higher CS yield, if long ns pulse duration is applied. Here, the CS yield, would be dependent from the composition and size of the particle, as predicted by the thermodynamic calculations

4.4.1 High core-shell formation – transferability to AuCo system

In the aim to prove the accuracy of the model proposed in chapter 4.4, contributing towards better control over nanoparticle ultrastructure, AuCo system was selected. Similar to iron, cobalt may transfer between FCC crystal phase additional crystal phase. Iron can transfer between 2 crystal phases FCC and BCC, whereas cobalt between FCC and HCP. According to Hume-Rothery rule phase segregation can only occur if 2 different phases are present[217, 220]. As gold has FCC phase, any elements with another crystal phase would favour phase segregation. Furthermore, this rule predicts phase segregation for a system where electronegativity, crystal structure, atomic radius shows the substantial difference, contrarily to elements with similar properties, which favour alloy formation. This is, however, a simplified assumption, as this prediction does not take into account liquid environment impact, which may also have a distinctive influence on NPs formation during LAL. Therefore, for a more precise comparison with AuFe only AuCo generated in acetone will be considered.

For the evaluation of the model proposed in the previous chapter, 3 comparison parameters were chosen. First of all, phase segregated (CS + MC) and MC yields were compared (Figure 33 a and b). Followed by an evaluation of the size dependency from the AuCo composition (Figure 33 c, d). Finally, with the help of XRD the crystal structure was analyzed (Figure 34-35). All the results were summarized and compared with the AuFe system.

Analysis of both, AuFe and AuCo revealed similar ultrastructure classes: SS, CS and MC NPs (Figure 32, S22). For the simplification purpose, the comparison was focused only on the segregated phases, including CS and MC NPs (Figure 33 a). EDX mapping confirmed Au (purple color) and Co-rich regions (yellow color), by detection of Co-K and Au-L signals for representative CS NPs (Figure 32 a). The low resolution of the EDX mapping image was caused by drift correction during analysis.

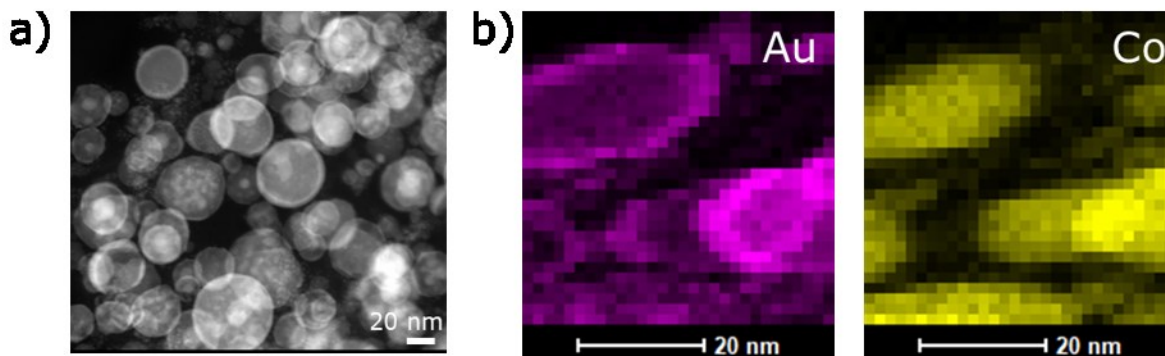


Figure 32: Evaluation of the AuCo composition with help of a) line scan through a single particle in which the formation of Au rich outer shell and Co rich inner core in a core-shell particle with is confirmed b) STEM image of Au₂₀Co₈₀ alloy NP with c), d) EDX mapping with Co-K (blue color) and Au-L (yellow color).

In Figure 33 a, the impact from the cobalt/iron content on the phase segregated NPs yield for AuCo and AuFe were compared respectively. Precisely, for non-noble Fe rich NPs, high phase segregated NPs yield reached approximately 80 at % with only 2% lower value for AuCo (78%). In the case of 50:50 at % composition, a more pronounced difference was observed. AuFe showed higher phase segregated NPs yield at 75%, whereas AuCo reached only 43% yield.

Remarkably, despite lack of the phase segregated NPs detection for Au rich NPs in the case of AuFe system, phase segregated NPs were detected for AuCo system. The absence of phase segregated NPs for any AuFe NPs with Fe content lower than 35%, can be correlated with the size restriction based on the theoretical calculation as shown in chapter 4.2.1. Thus, even though, for AuCo system, the same size regime is observed, based on the theoretical calculation (Figure S23, chapter S5, chapter 4.2.1.1) cut off diameter for Au rich NPs is above 8 nm for AuCo and 11 nm for AuFe. Meaning, that phase segregation can occur at smaller sizes for AuCo system, confirmed by detection of CS and MC NPs for Au₈₀Co₂₀.

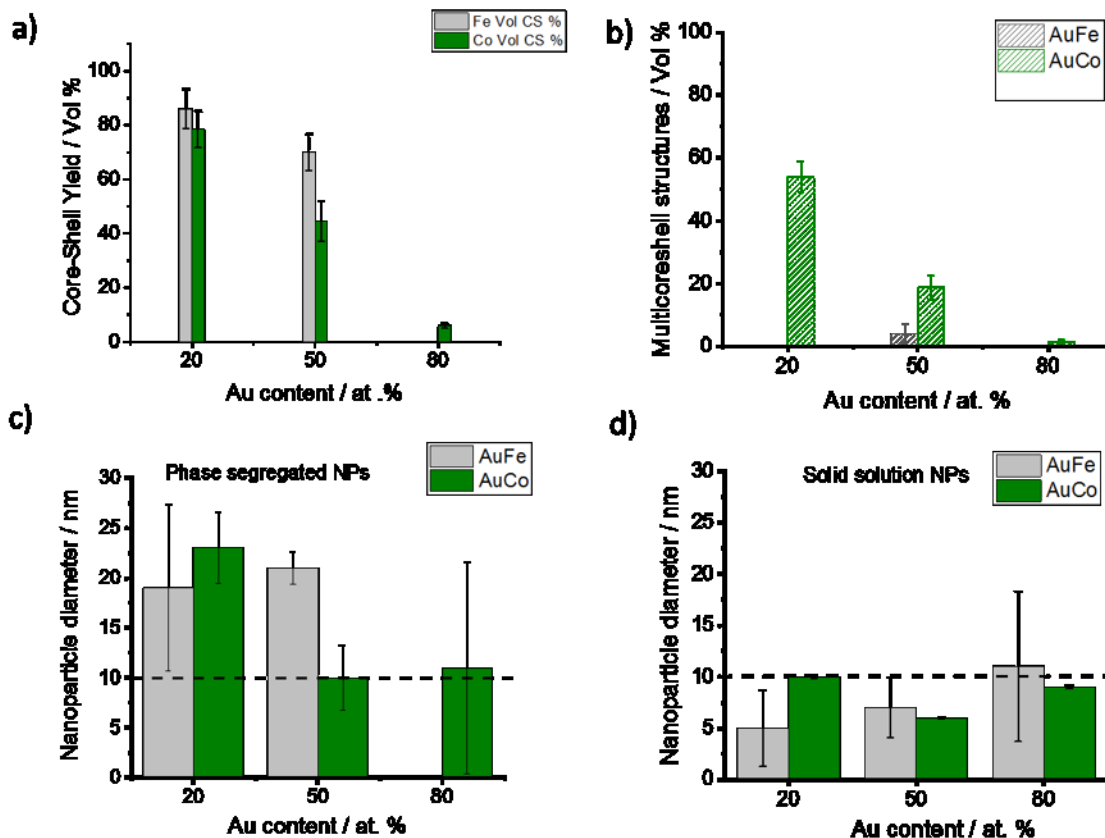


Figure 33: a) Phase segregated nanoparticles and b) Multi core-shell Yield dependency from Au content at % for both AuFe (gray bars) and AuCo (green bars) generated via 8 ns laser in acetone. Size composition dependency for molar ratio AuCo (green bars) (Figure S25) and AuFe (gray bars) system for c) core-shell NPs and d) solid solution NPs.

Nevertheless, high MC yield was detected for AuCo system (Figure 33b), especially for high Co content NPs ($\text{Au}_{20}\text{Co}_{80}$), with value > 50% of MC NPs. On the other side, only 20% were detected for $\text{Au}_{50}\text{Co}_{50}$ configuration and below 3% for Au rich one ($\text{Au}_{80}\text{Co}_{20}$). Contrarily, only composition $\text{Au}_{50}\text{Fe}_{50}$ showed around 5% MC within phase segregated NPs fraction, whereas other compositions did not show any MC presence. Notably, MC NPs are not desired as thin Au shell leads to low thermal and chemical stability (as proven in chapter 4.1.2).

In order to assess the diameter of the AuCo NPs (Figure 33 c), additional theoretical calculations as described in S5 chapter were performed (Figure S23). Interestingly, for AuCo cut off diameter for CS formation was the same as for AuFe approximately below 10 nm. The results depicted in Figure 33, confirmed this prediction, as phase segregated NPs (Figure 33 c) were all above 10 nm, whereas solid solution below 10 nm (Figure 33 d). The only exception was $\text{Au}_{80}\text{Fe}_{20}$, where SS NPs were around 11 nm, which can be correlated to the theoretical prediction that phase segregation would

be favored above 11 nm (chapter 4.2.1.1). A general trend can be observed for AuFe, where with increasing Au content, the size of the NPs increases, yet a decrease of phase segregation yield was observed. From the previous findings it was validated that, next to the bigger size (chapter 4.1.3), high Fe content leads to the formation of the phase segregated NPs. Therefore, by evaluating the experimental data both; size and the Fe content has to be considered. From the available data, it can be concluded that AuCo system did not show a clear size – composition trend. Both Au and Fe rich NPs showed similar diameters, whereas Au₅₀Fe₅₀ configuration was characteristic with a smaller diameter slightly above 5 nm.

Considering AuFe, BCC crystal phase was detected for Fe rich NPs, where high phase segregation yield was detected. In the aim to evaluate the crystal structure of AuCo system XRD analysis was performed (Figure 34). This method focused on 3 compositions Au₂₀Co₈₀, Au₅₀Co₅₀, Au₈₀Co₂₀ and Co as a reference. As shown in Figure 34 AuFe depicts 3 different FCC phases and 1 BCC phase (Figure 34 a). Whereas, AuCo resembles only 2 different FCC phases for all Au-Co compositions, contrarily to pure Co where an additional 1 HCP phase was detected (Figure 34 b). Interestingly, CS formation was possible even though no HCP crystal structure was detected.

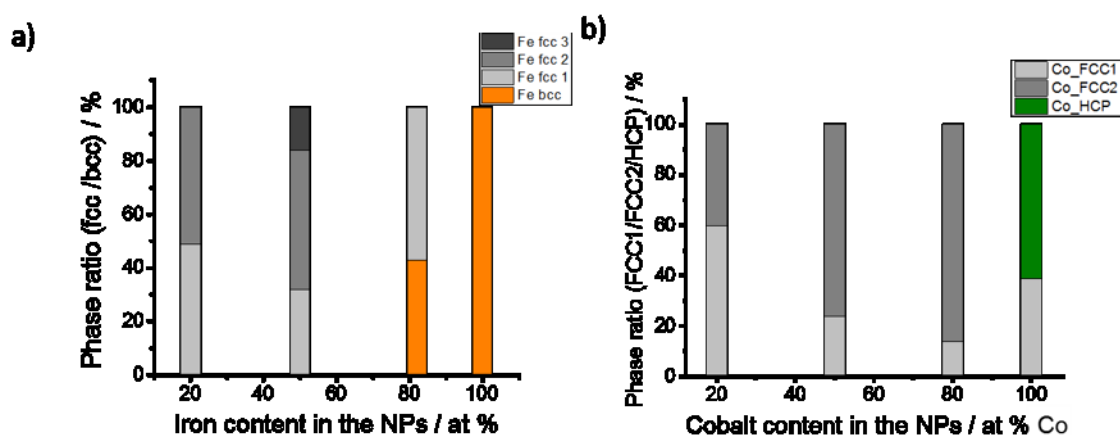


Figure 34: Phase ratio a) FCC1-3/BCC for AuFe system b) FCC1/FCC2/HCP for AuCo system (Figure S24).

Lack of addition HCP and high CS formation may be explained by the presence of nanocrystalline ϵ -Co phase. Dingea et al proposed next to HCP and FCC new crystal structures of ϵ -Co which belongs to the $P4_132$ space group with a cubic structure and lattice parameter $a=6.097\pm 0.001$ Å[221]. Such a structure was up to now only possible through the solution-phase approach. Therefore, the formation of CS NPs can be

contributed to nanocrystalline ϵ -Co favoring phase segregation due structure, which is less dense than both FCC and HCP. Synthesis of such nanocrystalline structures can be contributed to the high-temperature high-pressure condition inside the cavitation bubble followed by fast cooling ($> 10^{10} \text{ Ks}^{-1}$), leading to the formation of kinetically controlled metastable structures[222]. Furthermore, nanocrystalline cobalt resembles magnetic properties, which are dependent on the phase. For example, the symmetric low coercivity of the ϵ -Co can be used in an electronic devices, etc[223].

Lattice parameter in Figure 35 summarizes 3 differently substituted FCC crystal structures in regard to AuFe system. Apart from $\text{Au}_{50}\text{Fe}_{50}$ with a slightly elevated value to the Au lattice parameter at 4.07, FCC 1 resembled a decreasing trend with increasing Fe content. Similarly FCC 2, can be characterized with a decreasing trend when Fe doping increases. FCC 3 is only present for $\text{Au}_{50}\text{Fe}_{50}$ as previously described in chapter 4.1.3. AuCo resembled a similar behavior trend in comparison to the AuFe system.

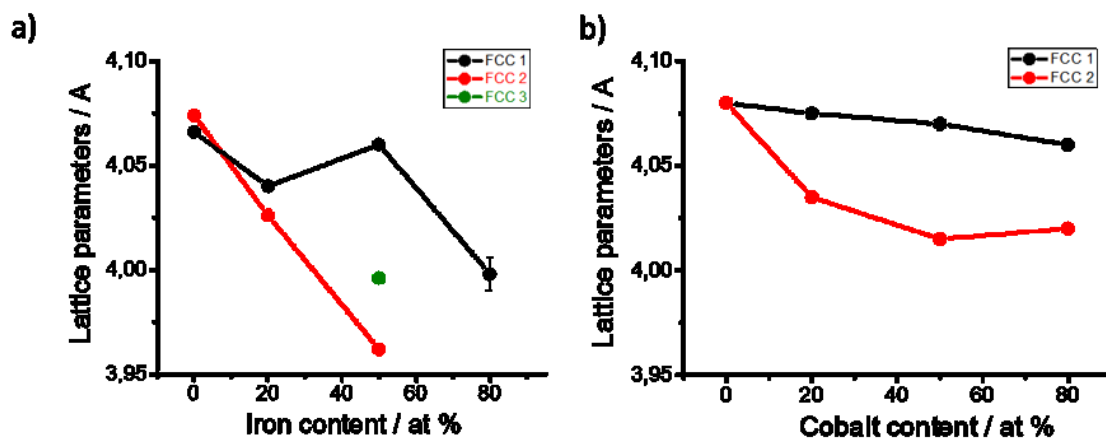


Figure 35: Lattice parameter corresponding to FCC 1,2 3 for a) AuFe system and FCC 1 & 2 for b) AuCo system.

Lattice parameter for FCC 1 phase of Co did not deviate resembling only a small decrease in lattice parameter from 4.08 to 4.07. Contrarily to FCC 2 phase where pronounced decrease from 4.08 to 4.02 for $\text{Au}_{50}\text{Co}_{50}$ composition can be observed, followed by a slight increase of up to 4.025 for Cobalt rich NPs. In both cases, it is evident that the substitution of Fe/Co atoms leads to a decrease of the lattice parameter of pure Au.

In summary, the model presented in chapter 4.4 was proven to be suitable for another binary system. Similar to AuFe, it is characterized with 3 different ultrastructures, SS, CS and MC NPs. Prediction based on the simple theoretical calculations (chapter S5), indicating that the phase segregation is more favored for bigger NPs (approximately above 10 nm), and was validated for both AuFe and AuCo with the presented data. With regard to crystal phase, phase segregation in CS NPs for AuCo system was most likely contributed to ϵ -Co. Interestingly, CS formation was possible despite absence of difference crystal phase (HCP), which according to Hume-Rothery Rule would be required in order for the particle to segregate. Nevertheless, this phenomenon can not be fully explain up to date. At last, as predicted by theoretical calculations, non noble metal composition contribution towards high phase segregation yields was validated. To sum up, the proposed model can be used for other binary systems, in which phase segregation driven by Gibbs free surface energy minimization can be predicted considering the particle composition and size.

5. Summary

The combination of magnetic, optical and electrical properties in one alloy nanoparticle is beneficial in numerous applications. The design of the multifunctional binary alloy nanomaterial is still limited due to the lack of a fundamental understanding of the laser ablation process. The biggest challenge is the precise clarification of the formation mechanism during laser ablation in liquids, both experimentally and theoretically. In particular, the full utilization of the properties is hindered by the generation of various ultrastructures. Despite the progress in the fundamental understanding of laser ablation of alloys in liquids, many challenges such as nanoparticle ultrastructure and size control remain to be solved. Control over the final alloy nanoparticles composition and structure can be achieved by adjusting parameters such as molar ratio, pulse duration, liquid environment, etc. In the aim to better elucidate the importance of condition during laser ablation, binary system Au-Fe was chosen for the systematic study. In particular, adjustment of the parameters towards high iron core gold shell configuration was motivated by high application demand in comparison to solid solution (alloy) nanoparticles.

The aim of this thesis was the design of the iron-gold nanoparticle formation mechanism model, by addressing an entire formation process during laser ablation with possible morphologies and stability of various phases. In this context, the influence from the target composition (Au:Fe molar ratio, multilayer- vs alloy-target), pulse duration: short ps- and long ns-pulse and liquid environment (alcohols, ketones, and highly viscous liquids) on the CS NPs formation was clarified. Nanoparticle ultrastructure, size, and the NPs composition were evaluated with the help of HAADF-STEM imaging, accompanied by Energy Dispersive X-Ray (EDX) spectroscopy. The focus was laid on the investigation of kinetic or thermodynamic contribution during LAL. For this purpose, thermal and chemical stability of various phases were investigated. In particular, nanophase diagram enriched by the formation mechanism model, and its transferability towards another binary alloy systems, generated via laser ablation in liquids was addressed.

In this work, the limitations of the pure core-shell NPs fraction formation due to the competitive process of synthesis of a solid solution will be addressed by the designed nanophase diagram. In the aim to design such model, a combination of simple thermodynamic calculations with the experimental approach was employed. The formation of the phase segregated nanoparticles was predicted based on the size and the molar fraction and then compared with the experimental approach. Here free surface Gibbs energy described NPs with a bigger diameter (>10 nm) as phase segregation favoring, due to its low value contrarily to solid solution NPs, only favored for smaller diameters (<7 nm). Admittedly, a certain discrepancy between the experimental and theoretical data was noted, in which a small fraction of SS solution resembled higher diameter, as predicted by the model (<20 nm). This can be correlated to the limitation of the model in case of the kinetically controlled morphologies. In this regard, the model does not apply for the structure which is not in thermodynamic equilibrium. For this reason, the model was extended toward another ultrastructure, with an alloy shell and pure elemental core. The recalculated values were characteristics with a shift for the bigger diameter threshold required to build the CS (in thermodynamic equilibrium) for gold-rich particles, from 7 to 23 nm. Yet only small variation in threshold diameter was observed for NPs with iron content > 50 at. %. Further, despite circumventing another relevant parameter involved during the laser ablation mechanism, a prediction based on those simple thermodynamic model was successfully confirmed experimentally. Further considering the adapted model, an interesting finding was made, namely, the formation of SS particles with a diameter below 10 nm, was observed independently from the target composition. Whereas, CS formation was observed only if the iron composition was above 50 at. %. However, the CS NPs are fundamentally different depending on target composition in gold-rich targets, the growth of these particles is quenched by interactions of gold-rich particles with the solvent acetone, yielding average particle sizes < 10 nm. As the iron-rich NPs, need to implement more iron, probably in BCC morphology and are consequently prone to form larger core-shell structures. To summarize, Fe FCC crystal structure favors SS NPs only when size is quenched below 10 nm. Whereas CS would be preferred for NPs with an average size above 10 nm, where high Fe fraction (above 50 at. %) and BCC crystal structure would attribute to phase segregation toward CS NPs. Remarkably, by comparison to the bulk phase diagram, in which fully segregated

iron core with the gold shell would be expected at the room temperature, non-equilibrium iron core with alloy shell were generated via laser ablation. Detailed, EDX and XRD analysis, confirmed alloy character of the shell, and formation of SS. These findings suggest kinetically controlled formation mechanisms during laser ablation of the iron gold system. Nevertheless, nanophase diagram can only deliver relevant information about the composition at a particular temperature, yet parameters such as liquid environment nor the pulse duration during laser ablation can be employed.

To this end, an experimental study has explored ways to more efficiently control the particle size and ultrastructure. First of all the pulse duration effect on the final NPs composition was tested for long ns and short ps pulse durations with Au₅₀Fe₅₀ composition having various thin layered target configurations. Mainly bilayer (AuFe/glass, FeAu/glass), multilayered (AuFeAuFe/glass) and Au/Fe alloy configuration. In all cases, bimodality was found with two different NPs structures small (<10 nm) solid solution alloy NPs and larger (>10 nm), segregated CS NPs. The results revealed that for both ns and ps pulse duration, the target with the outermost layer of Au leads to the formation of low CS yield, contrarily to alloy film, which allows high CS production. Nevertheless, CS yield was clearly lower for ps pulse duration than in the case of ns pulse duration, pointing out the importance of laser parameter in the determination of the final morphology. During short ps pulses, short plasma and cavitation bubble lifetime contribution to the formation of metastable alloy NPs. By contrast, for long ns pulse cavitation bubble lifetime is extended, allowing, therefore, phases closer to the thermodynamic equilibrium (CS) to be formed. Hence, the highest CS yield was achieved for long ns pulse from alloy targets and reached around 99 % per volume (87 % per number). Therefore, for Fe-Au system, it can be concluded, that well-mixed targets, as well as long ns pulses, lead to high CS yield as more time is given in the early stages of NPs formation to get closer to the thermodynamic equilibrium state (CS), overcoming diffusion limitation with pre-well-mixed elements in the target.

In addition, large efforts were devoted towards the controlled synthesis of defined ultrastructure and the size by application of various liquid environments, however, the limitations in the theoretical simulation field, as well as limited experimental data reported in the literature, hinders understanding of the liquid impact. The biggest

drawback is the evaluation of one parameter in a controllable way. Hence, although no clear trend between one chosen laser parameter and CS yield can be identified, an overview of liquid favoring high CS yield was summarized. Therefore, for the investigation on the impact of the liquid environment on the NPs ultrastructure alloy target with high Fe content ($\text{Au}_{20}\text{Fe}_{80}$) was chosen. Three groups of liquids were selected aiming to understand the liquid-particle interaction during LAL, mainly ketones (heat capacity), alcohols (chain length) and glycols with additional highly viscous PAO40 oil (viscosity). Overall, the generation of CS NPs was possible independently from the liquid environment. However, the most pronounced impact on high CS productivity was observed for viscosity and heat capacity. Interestingly with increasing viscosity, CS yield decreased, indicating that plasma plume confinement or bubble dynamic does not favor CS formation. On the other side heat capacity, which may impact the cooling and solidification rates, not only improve CS yield but also the generation of MC NPs. To summarize ketones showed the highest CS yield, with the lowest size distribution and an optimal stability for Fe rich NPs. Acetone is the most promising as during synthesis the lowest amount of MC was produced, with narrow size distribution and sufficient colloid stability.

Finally, the formation mechanism for the gold iron binary alloy system during laser ablation was addressed. To this end, the evaluation of either kinetic or thermodynamic contribution during laser ablation was investigated. In this context, detailed analysis with HAADF-STEM, EDX, and XRD was performed, revealing 4 different ultrastructure solid solution (SS), core-shell (CS), multi core-shell (MC) and jellyfish. Based on the bulk phase diagram, CS with a pure iron core and the gold shell would be thermodynamically favored. Yet, independently from the applied condition during LAL, SS alloy NPs were always present. Thus, indicating kinetically controlled contribution regarding NPs formation. Remarkably, phase segregation between the gold shell and iron core within CS NPs was not completed. A significant amount of iron was found in the gold shell, with the quantity depending on the composition in the target. The pure nature of Fe core can be justified by BCC crystal structure, where only a few % of gold can be implemented. The nanoparticle in non-equilibrium phase was further confirmed by thermal stability test, where NPs with high Fe content, both

SS and CS transformed into a phase in thermodynamical equilibrium, the tetrakis hexahedron structures. Whereas, NPs with composition $\text{Au}_{50}\text{Fe}_{50}$ fell apart. Another example showing the importance of molar ratio not only on the CS yield but also on NPs stability. Moreover, shell thickness contributes to the thermal stability leading to element separation in the case of a particle with thin Au rich shell. Worth to mention is the chemical stability of the CS NPs, where the negligible impact on the architecture of the Au shell was observed, after etching with concentrated acid. Fe was leached out, leaving porous stable Au particle. The results collected within this work, reveal the critical role of the pulse duration, composition and size of the particle towards morphology control. The formation mechanism proposal is supported based on the data collected in this work and is summarized as followed. The NP formation during LAL is a kinetically controlled process, which based on the pulse duration allows the NP to either formed phase close to their thermodynamic equilibrium state (long ns pulse) or are captured as kinetically frozen products (short ps pulse) in metastable alloy form. Notably, alloy target contributed towards higher CS yield, yet SS morphology is always present, and most likely generated in the liquid/gas region of the cavitation bubble due to its size restricted as predicted by simple theoretical calculations. Whereas CS NPs are formed in the region closer to the molten layers. No statement can be made based on the liquid environment, apart from the conclusion that CS formation is possible independently from the liquid. In summary, the significance of size and the elemental fraction in target, target thickness, pulse duration, and that the liquid, which has a profound influence on the final composition of the AuFe laser-generated NPs was shown.

The combination of theoretical and experimental approaches represent a promising tool to gain more knowledge in the fundamental understanding of nanoparticle formation during laser ablation in liquids. The proposed model transferability was confirmed for another binary alloy system, and therefore it may be used for further systems, for which phase segregation is driven by Gibb's free surface energy under the restriction of Hume-Rothery rule.

6. outlook

Although the experimental and theoretical approach within this thesis contributed to knowledge about nanoparticle formation mechanism during laser ablation in liquid, yet for towards full understanding of this process, there are still many aspects to be discovered. Here the detailed analysis of parameters such as molar ratio, liquid environment, and pulse duration as well as a detailed investigation of Core-shell ultrastructure contributed towards the mechanistic model, relevant for other binary systems fulfilling Hume-Rothery rule towards phase segregation.

Further experiments should be conducted with various binary, ternary system e.g. FeCoAu or FeNiAu. Where a combination of simulation and experimental data would allow preparing a library of conditions for preparation of various ultrastructure with different compositions depending on the required application. Such an idea is driven by the lack of phase diagram at nanoscale for many binary alloy systems.

Additionally, an extension of the investigated parameter, especially liquid environment, as well as another laser parameter e.g., pulse energy, could contribute even further to more precise control over either CS or SS NPs formation. The most pressing issue is the competitive formation of SS independently from the applied condition. This accounts for the question if a clean fraction of either SS or CS can be generated via laser ablation in liquid. Due to its magnetic properties, additional techniques such as centrifugation or membrane selection are not sufficient to separate smaller SS (< 10 nm) from bigger CS (<10 nm) NPs. Preliminary experiments also with the magnetic field were unfortunately unsuccessful. Moreover, NPs stabilization in acetone is lost if transferred into water in case of membrane separation, encouraging to look for alternative conditions towards biomedical application.

7. Appendix

7.1 Reference

1. F. Calvo, *Nanocalloys: from fundamentals to emergent applications*, ed. Elsevier. 2013, Oxford.
2. Gajanan, K. and S.N. Tijare, *Applications of nanomaterials*. Materials Today: Proceedings, 2018. 5(1): p. 1093-1096.
3. Abdullaeva, Z., *Nanomaterials in Daily Life Compounds, Synthesis, Processing and Commercialization*. 2017: Springer, Cham.
4. Olea-Mejía, O., et al., *SERS-active Ag, Au and Ag–Au alloy nanoparticles obtained by laser ablation in liquids for sensing methylene blue*. Applied Surface Science, 2015. 348: p. 66-70.
5. Wadell, C., et al., *Hysteresis-free nanoplasmonic Pd-Au alloy hydrogen sensors*. Nano Lett, 2015. 15(5): p. 3563-70.
6. Malaki, M., et al., *Advanced Metal Matrix Nanocomposites*. Metals, 2019. 9(3): p. 330.
7. Gangopadhyay, P., *Metallic Alloy Nanoparticles and Metal-Semiconductor Nanomaterials*. NanoWorld Journal, 2018. 04(03).
8. Roy Chowdhury, S., K. Kanti Bera, and S. Kumar Bhattacharya, *Enhanced and Synergistic Catalysis of Green Synthesized Pd-Ag Alloy Nanoparticles for Anodic Oxidation of Propan-2-ol in Alkali*. Materials Today: Proceedings, 2018. 5(1): p. 2171-2178.
9. Carpenter, M.K., et al., *Solvothermal synthesis of platinum alloy nanoparticles for oxygen reduction electrocatalysis*. J Am Chem Soc, 2012. 134(20): p. 8535-42.
10. Marzun, G., et al., *Laser synthesis, structure and chemical properties of colloidal nickel-molybdenum nanoparticles for the substitution of noble metals in heterogeneous catalysis*. J Colloid Interface Sci, 2017. 489: p. 57-67.
11. Million, N.C., V. ; Wile, P. ; Rehbock, C. ; Vogt, P. M. ; Pich, A. ; Barcikowski, S., *Water-based, surfactant-free cytocompatible nanoparticle-microgel-composite biomaterials - rational design by laser synthesis, processing into fiber pads and impact on cell proliferation*. BioNanoMaterials, 2017. 18(3-4): p. 1-18.
12. Springer, A., et al., *Development of new processes for welding of thermal Al–Cu solar absorbers using diode lasers*. Journal of Laser Applications, 2012. 24(5).
13. Reiss, G. and A. Hutten, *Magnetic nanoparticles: applications beyond data storage*. Nat Mater, 2005. 4(10): p. 725-6.
14. Cao, Y.J., R.; Mirkin, C. , *DNA-Modified Core-Shell Ag/Au Nanoparticles*. J. Am. Chem. Soc., 2001. 123: p. 7961–7962.
15. Sun, Q.K., A.; Wang, Q.; Jena, P.; Kawazoe, Y.; Marquez, M., *Effect of Au Coating on the Magnetic and Structural Properties of Fe Nanoclusters for Use in Biomedical Applications: A density functional Theoretical Study*. Rev. B: Condens. Matter Mater. Phys., 2006. 73: p. 134409.
16. Ferrando, R., Jellinek, J., Johnston, R. L., *Nanocalloys: From theory to applications of alloy clusters and nanoparticles*. Chemical Reviews, 2008. 108(3): p. 845-910.
17. Amendola, V., et al., *Formation of alloy nanoparticles by laser ablation of Au/Fe multilayer films in liquid environment*. J Colloid Interface Sci, 2017. 489: p. 18-27.
18. Rehbock, C., J.J.G.L., et. Al, , *Current state of laser synthesis of metal and alloy nanoparticles as ligand-free reference materials for nano-toxicological assays*. Beilstein J Nanotechnol., 2014. 5: p. 1523–1541.
19. Zhang, D., B. Gokce, and S. Barcikowski, *Laser Synthesis and Processing of Colloids: Fundamentals and Applications*. Chem Rev, 2017. 117(5): p. 3990-4103.
20. Zhang Dongshi, G.B., Barcikowski Stephan *Laser synthesis and processing of colloids; fundamentals and applicaiton*. ACS publications.

21. Barcikowski, S.A., Vincenzo; Marzun, Galina; Rehbock, Christoph; Reichenberger, Sven; Zhang, Dongshi; Gökce, Bilal, *Handbook of Laser Synthesis of Colloids*. 2016.
22. Amendola, V. and M. Meneghetti, *What controls the composition and the structure of nanomaterials generated by laser ablation in liquid solution?* *Phys Chem Chem Phys*, 2013. **15**(9): p. 3027-46.
23. Anastas, P.E., N., *Green chemistry principals and practice*. *Chem. Soc. Rev.* , 2010. **39**: p. 301-312.
24. Vassalini, I., et al., *Enhanced Electrocatalytic Oxygen Evolution in Au-Fe Nanoalloys*. *Angew Chem Int Ed Engl*, 2017. **56**(23): p. 6589-6593.
25. Kleibert, A., et al., *Structure, morphology, and magnetic properties of Fe nanoparticles deposited onto single-crystalline surfaces*. *Beilstein J Nanotechnol*, 2011. **2**: p. 47-56.
26. M., L.-M.L., *Tailoring surface plasmons through the morphology and assembly of metal nanoparticles*. *Langmuir* 2006. **22**: p. 32-41.
27. Amendola, V., et al., *Coexistence of plasmonic and magnetic properties in Au₈₉Fe₁₁ nanoalloys*. *Nanoscale*, 2013. **5**(12): p. 5611-9.
28. Dykman, L.A. and N.G. Khlebtsov, *Gold nanoparticles in biology and medicine: recent advances and prospects*. *Acta Naturae*, 2011. **3**(2): p. 34-55.
29. S., P.S.B., *Conjugation efficiency of laser-based bioconjugation of Gold nanoparticles with nucleic acids*. *J. Phys. Chem. C*, 2009. **113**: p. 19830–19835.
30. Ke, F., et al., *Controlled synthesis of novel Au@MIL-100(Fe) core-shell nanoparticles with enhanced catalytic performance*. *Chem Commun (Camb)*, 2013. **49**(13): p. 1267-9.
31. Ke, F., L. Wang, and J. Zhu, *Multifunctional Au-Fe₃O₄@MOF core-shell nanocomposite catalysts with controllable reactivity and magnetic recyclability*. *Nanoscale*, 2015. **7**(3): p. 1201-8.
32. Yun-Qian Li, M.X., Udesch Dhawan, Wai-Ching Liu, Kou-Ting Wu, Xin-Rui Liu, Chingpo Lin, Gang Zhao, Yu-Chuan Wu, and Ren-Jei Chung, *Iron-gold alloy nanoparticles serve as a cornerstone in hyperthermia-mediated controlled drug release for cancer therapy*. *Int J Nanomedicine*, 2018. **13**: p. 5499–5509.
33. Kayal S. , R.R.V.J., *Anti-cancer drug loaded Iron-Gold core-shell nanoparticles (Fe@Au) for magnetic drug targeting*. *Nanotechnol*. **10**: p. 5527–5539.
34. Sun, X., et al., *Tracking stem cells and macrophages with gold and iron oxide nanoparticles – The choice of the best suited particles*. *Applied Materials Today*, 2019. **15**: p. 267-279.
35. Alele, N., et al., *Ultrafiltration membrane-based purification of bioconjugated gold nanoparticle dispersions*. *Separation and Purification Technology*, 2016. **157**: p. 120-130.
36. Jun, Y.W., J.H. Lee, and J. Cheon, *Chemical design of nanoparticle probes for high-performance magnetic resonance imaging*. *Angew Chem Int Ed Engl*, 2008. **47**(28): p. 5122-35.
37. Cho, S.J., et al., *Gold-coated iron nanoparticles: a novel magnetic resonance agent for T-1 and T-2 weighted imaging*. *Nanotechnology*, 2006. **17**(3): p. 640-644.
38. Dahl, J.A., B.L. Maddux, and J.E. Hutchison, *Toward greener nanosynthesis*. *Chem Rev*, 2007. **107**(6): p. 2228-69.
39. Cho, S.J., et al., *Growth mechanisms and oxidation resistance of gold-coated iron nanoparticles*. *Chemistry of Materials*, 2005. **17**(12): p. 3181-3186.
40. Jendrzej S., D.G.B., Epple M. Barcikowski S., , *How Size Determines the Value of Gold: Economic Aspects of Wet Chemical and Laser-Based Metal Colloid Synthesis*,. 2017. **18**(9): p. 1012–1019
41. Amendola, V., et al., *Magneto-plasmonic Au-Fe alloy nanoparticles designed for multimodal SERS-MRI-CT imaging*. *Small*, 2014. **10**(12): p. 2476-86.
42. Wagener, P., et al., *Solvent-surface interactions control the phase structure in laser-generated iron-gold core-shell nanoparticles*. *Sci Rep*, 2016. **6**: p. 23352.

43. Gokce, B., V. Amendola, and S. Barcikowski, *Opportunities and Challenges for Laser Synthesis of Colloids*. Chemphyschem, 2017. **18**(9): p. 983-985.
44. Neumeister, A., et al., *Monophasic ligand-free alloy nanoparticle synthesis determinants during pulsed laser ablation of bulk alloy and consolidated microparticles in water*. Phys Chem Chem Phys, 2014. **16**(43): p. 23671-8.
45. Zhang, J., et al., *Preparation of PtAu Alloy Colloids by Laser Ablation in Solution and Their Characterization*. The Journal of Physical Chemistry C, 2012. **116**(24): p. 13413-13420.
46. Malviya, K.D. and K. Chattopadhyay, *Synthesis and Mechanism of Composition and Size Dependent Morphology Selection in Nanoparticles of Ag–Cu Alloys Processed by Laser Ablation Under Liquid Medium*. The Journal of Physical Chemistry C, 2014. **118**(24): p. 13228-13237.
47. I.-C. Chiang and D.-H. Chen, *Synthesis of monodisperse feau nanoparticles with tunable magnetic and optical properties*. Advanced Functional Materials, 2007. **17**(8): p. 1311–1316.
48. C. W. Hills, N.H.M., and R. G. Nuzzo, *The size-dependent structural phase behaviors of supported bimetallic (Pt-Ru) nanoparticles*. The Journal of Physical Chemistry B, 2003. **107**(12): p. 2626–2636.
49. Luo, M.M.M., V. Petkov, N. N. Kariuki, L. Wang, P. Njoki, D. Mott, Y. Lin, and C.-J. Zhong, , *Phase properties of carbon-supported gold-platinum nanoparticles with different bimetallic compositions*. Chemistry of materials, 2005. **17**(12): p. 3086–3091.
50. Z. Peng and H. Yang, *Ag–Pt alloy nanoparticles with the compositions in the miscibility gap*. Journal of Solid State Chemistry, 2008. **181**(7): p. 1546–1551.
51. S. Xiao, W.H., W. Luo, Y. Wu, X. Li, and H. Deng, *Size effect on alloying ability and phase stability of immiscible bimetallic nanoparticles*. The European Physical Journal B-Condensed Matter and Complex Systems, 2006. **54**(4): p. 479-484.
52. Damien Alloyeau, C.M., Christian Ricolleau, *Nanoalloys: Synthesis, Structure and Properties*. 2012: Springer Science & Business Media.
53. Kolosnjaj-Tabi, J., et al., *The One Year Fate of Iron Oxide Coated Gold Nanoparticles in Mice*. ACS Nano, 2015. **9**(8): p. 7925-39.
54. Swiatkowska-Warkocka, Z., et al., *Synthesis of new metastable nanoalloys of immiscible metals with a pulse laser technique*. Sci Rep, 2015. **5**: p. 9849.
55. Calvo, F., *Nanoalloys: From Fundamentals to Emergent Applications*. 2013: Elsevier.
56. Favez, D., J.D. Wagniere, and M. Rappaz, *Au-Fe alloy solidification and solid-state transformations*. Acta Materialia, 2010. **58**(3): p. 1016-1025.
57. Bosco, *Phase transformations in Au–Fe melt spun alloys*. Materials Science and Engineering A, 2004. **375**(1): p. 468-472.
58. Mizutani, U., *Hume-Rothery Rules for structural Complex Alloy Phases*. CRC Press. 2011.
59. Guisbiers, G., et al., *Electrum, the Gold-Silver Alloy, from the Bulk Scale to the Nanoscale: Synthesis, Properties, and Segregation Rules*. ACS Nano, 2016. **10**(1): p. 188-98.
60. Guisbiers, G., et al., *Gold-copper nano-alloy, "Tumbaga", in the era of nano: phase diagram and segregation*. Nano Lett, 2014. **14**(11): p. 6718-26.
61. Zhuravlev, I.A., et al., *Phase stability, ordering tendencies, and magnetism in single-phase fcc Au-Fe nanoalloys*. Physical Review B, 2017. **96**(13).
62. Handwerker, C.A. and T.M. Pollock, *Emerging Science and Research Opportunities for Metals and Metallic Nanostructures*. Jom, 2014. **66**(7): p. 1321-1341.
63. Cheng, G. and A.R. Hight Walker, *Synthesis and characterization of cobalt/gold bimetallic nanoparticles*. Journal of Magnetism and Magnetic Materials, 2007. **311**(1): p. 31-35.
64. Estelrich, J. and M.A. Busquets, *Iron Oxide Nanoparticles in Photothermal Therapy*. Molecules, 2018. **23**(7).

65. Fang, Z., et al., *Evolution of light-induced vapor generation at a liquid-immersed metallic nanoparticle*. Nano Lett, 2013. **13**(4): p. 1736-42.
66. Anderson, S.D., V.V. Gwenin, and C.D. Gwenin, *Magnetic Functionalized Nanoparticles for Biomedical, Drug Delivery and Imaging Applications*. Nanoscale Res Lett, 2019. **14**(1): p. 188.
67. Eustis, S. and M.A. El-Sayed, *Why gold nanoparticles are more precious than pretty gold: Noble metal surface plasmon resonance and its enhancement of the radiative and nonradiative properties of nanocrystals of different shapes*. Chemical Society Reviews, 2006. **35**(3): p. 209-217.
68. Homola, J., *Surface Plasmon Resonance Based Sensors*, ed. S.S.B. Media. 2006.
69. Yi-Tao Long, C.J., *Localized Surface Plasmon Resonance Based Nanobiosensors*. 2014: Springer Science & Business Media.
70. Jana, J., M. Ganguly, and T. Pal, *Enlightening surface plasmon resonance effect of metal nanoparticles for practical spectroscopic application*. RSC Advances, 2016. **6**(89): p. 86174-86211.
71. Duynne., K.A.W.u.R.P.V., *Localized surface plasmon resonance spectroscopy and sensing*. . Annu. Rev. Phys. Chem.,, 2007. **58**(1): p. 267 – 297.
72. Kelly, K.L., et al., *The optical properties of metal nanoparticles: The influence of size, shape, and dielectric environment*. Journal of Physical Chemistry B, 2003. **107**(3): p. 668-677.
73. Pal., S.K.G.u.T., *Interparticle coupling effect on the surface plasmon resonance of gold nanoparticles: From theory to applications*. Chem. Rev., 2007. **107**(11): p. 4797 – 4862.
74. Erik C. Dreaden, A.M.A., Xiaohua Huang, Catherine J. Murphy und Mostafa A. El-Sayed. , *The golden age: gold nanoparticles for biomedicine*. . Chem. Soc. Rev., , 2012. **41**(7): p.:2740 – 2779.
75. Link, S. and M.A. El-Sayed, *Shape and size dependence of radiative, non-radiative and photothermal properties of gold nanocrystals*. International Reviews in Physical Chemistry, 2000. **19**(3): p. 409-453.
76. Peter N. Njoki, I.-I.S.L., Derrick Mott, Hye-Young Park, Bilal Khan, Suprav Mishra, Ravishanker Sujakumar, Jin Luo und Chuan-Jian Zhong. , *Size correlation of optical and spectroscopic properties for gold nanoparticles*. . J. Phys. Chem. C, , 2007. **111**(40): p.:14664 – 14669.
77. Xiaohua Huang, I.H.E.-S., Wei Qian und Mostafa A. El-Sayed. , *Cancer cell imaging and photothermal therapy in the near-infrared region by using gold nanorods*. J. Am. Chem. Soc., , 2006. **128**(6): p. 2115 – 2120.
78. Zhang, J., Post, M, Veres, T., Jakubek, Z. J, Guan, J., Wang, D., Normandin, F., *Laser assisted synthesis of supermagnetic Fe@Au Core-Shell nanoparticles*. J. Phys. Chem. B., 2006. **110**: p. 7122-7128.
79. Nguyen, T.T., F. Mammeri, and S. Ammar, *Iron Oxide and Gold Based Magneto-Plasmonic Nanostructures for Medical Applications: A Review*. Nanomaterials (Basel), 2018. **8**(3).
80. Abd-Elsalam, K.A., Mohamed A. Mohamed, Prasad Ram *Magnetic Nanostructures: Environmental and Agricultural Applications*. 2019: Springer.
81. Bautin, V.A., et al., *Magnetic properties of polycrystalline cobalt nanoparticles*. AIP Advances, 2017. **7**(4).
82. Reddy, L.H., Arias, J. L., Nicolas, J, Couvreur, P., *Magnetic nanoparticles: design and characterization, toxicity and biocompatibility, Pharmaceutical and biomedical applications*. Chem Rev., 2012. **112**: p. 5818-5878.
83. Hudson, R., et al., *Highly efficient iron(0) nanoparticle-catalyzed hydrogenation in water in flow*. Green Chemistry, 2013. **15**(8).
84. Maneeratanasarn, P., et al., *Synthesis of phase-controlled iron oxide nanoparticles by pulsed laser ablation in different liquid media*. Physica Status Solidi a-Applications and Materials Science, 2013. **210**(3): p. 563-569.

85. Fan J.H., H.W.I., Li W.T., Yeh J.M. , *Biocompatibility Study of Gold Nanoparticles to Human Cells*. Lim C.T., Goh J.C.H., 2009. **23**(13th International Conference on Biomedical Engineering.)
86. Gubin, S.P., *Magnetic nanoparticle* 2007, Wiley-VCH.
87. Wijn, H.P.J., *Magnetic Properties of Metals: d-Elements, Alloys and Compounds*. 2012: Springer Science & Business Media,.
88. Thanh, N.T., *Clinical Applications of Magnetic Nanoparticles: From Fabrication to Clinical Applications*. 2018: CRC Press, .
89. Thanh, N.T.K., *MAGNETIC NANOPARTICLES From Fabrication to Clinical Applications*. 2012: CRC Press.
90. W. Schütt, C.G., U. Häfeli, , *Hybridoma*, , 1997. **16**: p. 109.
91. Neuberger, T., et al., *Superparamagnetic nanoparticles for biomedical applications: Possibilities and limitations of a new drug delivery system*. *Journal of Magnetism and Magnetic Materials*, 2005. **293**(1): p. 483-496.
92. Redolfi, E., Pastoriza-santos, I., Lak, A., Pellegrino, T., Pérez-juste, J., Mattoli, V. , *Plasmonic / Magnetic Nanocomposites: Gold Nanorods-Functionalized Silica Coated Magnetic Nanoparticles*. *Journal of colloid and interface science.*, 2017. **502**: p. 201-209. .
93. Silva, S.M., Tavallaie, R., Sandiford, L., Tilley, D., Gooding, J.J. *Gold Coated* 2016; , *Magnetic Nanoparticles : From Preparation to Surface Modification for Analytical and Biomedical Applications*. *Chemical Communications*. , 2016. **52**: p. 7528-7540
94. Kinoshita, T., Seino, S., Mizukoshi, Y. , *Functionalization of Magnetic Gold / Iron-Oxide Composite Nanoparticles With Oligonucleotides and Magnetic Separation of Specific Target*. . *Journal of Magnetism and Magnetic Materials.*, 2007. **311**: p. 255-258
95. Faraday, M., *The Bakerian Lecture: Experimental Relations of Gold (and Other Metals) to Light*. *Philosophical Transactions of the Royal Society of London*, 1857. **147**: p. 145–181.
96. Turkevich, J., P.C. Stevenson, and J. Hillier, *A Study of the Nucleation and Growth Processes in the Synthesis of Colloidal Gold*. *Discussions of the Faraday Society*, 1951. **11**(11): p. 55-&.
97. Wang, X., et al., *Rapid construction of TiO₂ aggregates using microwave assisted synthesis and its application for dye-sensitized solar cells*. *RSC Advances*, 2015. **5**(12): p. 8622-8629.
98. Murray, C.B., C.R. Kagan, and M.G. Bawendi, *Synthesis and Characterization of Monodisperse Nanocrystals and Close-Packed Nanocrystal Assemblies*. *Annual Review of Materials Science*, 2000. **30**(1): p. 545-610.
99. Sousa, F., et al., *Superparamagnetic Nanoparticles as High Efficiency Magnetic Resonance Imaging T2 Contrast Agent*. *Bioconjug Chem*, 2017. **28**(1): p. 161-170.
100. Amendola, V. and M. Meneghetti, *Laser ablation synthesis in solution and size manipulation of noble metal nanoparticles*. *Phys Chem Chem Phys*, 2009. **11**(20): p. 3805-21.
101. Yang, G., *Laser ablation in liquids: Applications in the synthesis of nanocrystals*. *Progress in Materials Science*, 2007. **52**(4): p. 648-698.
102. Barcikowski, S.C., G., *Advanced nanoparticle generation and excitation by lasers in liquids*. *Phys. Chem. Chem. Phys.*, 2013. **15**: p. 3022–3026.
103. H. Yoo, S.H.J., X.L. Mao, R. Greif, R.E. Russo, ,, *Evidence for phase-explosion and generation of large particles during high power nanosecond laser ablation of silicon*. *Appl. Phys. Lett.* , 2000. **76**: p. 783-785. .
104. Zhigilei, L.V., Z. Lin, and D.S. Ivanov, *Atomistic Modeling of Short Pulse Laser Ablation of Metals: Connections between Melting, Spallation, and Phase Explosion*. *The Journal of Physical Chemistry C*, 2009. **113**(27): p. 11892-11906.

105. Sakka, T., et al., *Laser ablation at solid-liquid interfaces: An approach from optical emission spectra*. Journal of Chemical Physics, 2000. **112**(19): p. 8645-8653.
106. Dell'Aglio, M.G., R.; De Pascale, O.; De Giacomo, A., *Mechanism and Processes of pulsed laser ablation in liquids during nanoparticles production*. Appl. surf. Sci. , 2015. **348**: p. 4-9.
107. Kabashin, A.V. and M. Meunier, *Synthesis of colloidal nanoparticles during femtosecond laser ablation of gold in water*. Journal of Applied Physics, 2003. **94**(12).
108. Kim, K.K., Roy, M., Kwon, H., Song, J.K., Park S. M., , *Laser ablation dynamics in liquid phase: the effects of magnetic field and electrolyte* 2015, J. Appl. Phys. . p. 074302.
109. Lam, J., et al., *Al₂O₃ nanoparticles synthesis by pulse laser ablation in liquids a plasma analysis*. Phys. Chem. Chem. Phys, 2014. **16**: p. 963-973.
110. Matsumoto, A., et al., *Transfer of the Species Dissolved in a Liquid into Laser Ablation Plasma: An Approach Using Emission Spectroscopy*. Journal of Physical Chemistry C, 2015. **119**(47): p. 26506-26511.
111. Tamura, A.M., A.; Fukami, K.; Nishi, N.; Sakka, T., *Simultaneous Observation of Nascent Plasma and Bubble Induced by Laser Ablation in Water with Various Pulse Durations*. . J. Appl. Phys., 2015. **117**: p. 173304.
112. C.-Y. Shih, C.W., M. V. Shugaev and L. V. Zhigilei, , *Atomistic Modeling of Nanoparticle Generation in Short Pulse Laser Ablation of Thin Metal Films in Water*. J. Colloid Interface Sci., 2017. **489**: p. 3–17.
113. Zhang, D.G.k., B.; Notthoff, C.; Barcikowski, S. and 1., *Layered Seed-Growth of AgGe Football-like Microspheres via Precursor-Free*. Sci. Rep. , 2015. **5**: p. 13661.
114. Jendrzzej, S., et al., *Barrierless growth of precursor-free, ultrafast laser-fragmented noble metal nanoparticles by colloidal atom clusters - A kinetic in situ study*. J Colloid Interface Sci, 2016. **463**: p. 299-307.
115. Tomko, J.N., J. J.; Jimenez, R.; Tan, Y.; Steiner, M.; Fitz-Gerald, J. M.; Bubb, D. M.; O'Malley, S. M. , *Size and Polydispersity Trends Found in Gold Nanoparticles Synthesized by Laser Ablation in Liquids*. . Phys. Chem. Chem. Phys., 2015. **17**: p. 16327–16333.
116. Bubb, D., *Cavitation Bubble Dynamics and Nanoparticle Size Distributions in Laser Ablation in Liquids*, in ANGEL. 2016: Essen, Germany.
117. Ibrahimkuty, S., et al., *Nanoparticle formation in a cavitation bubble after pulsed laser ablation in liquid studied with high time resolution small angle x-ray scattering*. Applied Physics Letters, 2012. **101**(10).
118. Wagener, P., et al., *Dynamics of silver nanoparticle formation and agglomeration inside the cavitation bubble after pulsed laser ablation in liquid*. Phys Chem Chem Phys, 2013. **15**(9): p. 3068-74.
119. Bonse, J.B., S.; Krüger, J.; Kautek, W.; Lenzner, M., *Femtosecond Laser Ablation of Silicon—Modification Thresholds and Morphology*. . Appl. Phys. A: Mater. Sci. Process., 2002. **74**: p. 19–25.
120. Dörfler, H.-D., *Grenzflächen und kolloid-disperse Systeme: Physik und Chemie*; . 2002, Berlin: Springer.
121. Musaev, O.R., et al., *Influence of the liquid environment on the products formed from the laser ablation of tin*. Applied Physics A, 2013. **113**(2): p. 355-359.
122. Jung, H.J. and M.Y. Choi, *Specific Solvent Produces Specific Phase Ni Nanoparticles: A Pulsed Laser Ablation in Solvents*. Journal of Physical Chemistry C, 2014. **118**(26): p. 14647-14654.
123. Lam, J., et al., *Dynamical study of bubble expansion following laser ablation in liquids*. Applied Physics Letters, 2016. **108**(7).
124. Tsuji, T.T., D. H.; Okazaki, Y.; Nakanishi, M.; Tsuboi, Y.; Tsuji, M. , *Preparation of Silver Nanoparticles by Laser Ablation in Polyvinylpyrrolidone Solutions*. Appl. Surf. Sci. , 20098. **254**: p. 5224–5230.

125. Mortazavi, S.Z., et al., *Hydrogen storage property of laser induced Pd-nanoparticle decorated multi-walled carbon nanotubes*. Rsc Advances, 2013. **3**(5): p. 1397-1409.
126. Tsuji, T.T., Y.; Kitamura, N.; Tsuji, M. , *Microsecond-Resolved Imaging of Laser Ablation at Solid–Liquid Interface: Investigation of Formation Process of Nano-Size Metal Colloids*. . Appl. Surf. Sci. , 2004. **229**(365-371).
127. Rehbock, C., et al., *Size control of laser-fabricated surfactant-free gold nanoparticles with highly diluted electrolytes and their subsequent bioconjugation*. Phys Chem Chem Phys, 2013. **15**(9): p. 3057-67.
128. Waag, F., et al., *Adjusting the catalytic properties of cobalt ferrite nanoparticles by pulsed laser fragmentation in water with defined energy dose*. Sci Rep, 2017. **7**(1): p. 13161.
129. Zhang, D., et al., *Germanium Sub-Microspheres Synthesized by Picosecond Pulsed Laser Melting in Liquids: Educt Size Effects*. Sci Rep, 2017. **7**: p. 40355.
130. Hagedorn, K.L., B.; Marcinkevicius, A. , *Intermetallic PtPb Nanoparticles Prepared by Pulsed Laser Ablation in Liquid*. J. Electrochem. Soc. 2013, , 2013. **160**: p. F106–F110.
131. Zhang, D.M., Z.; Spasova, M.; Yelsukova, A. E.; Lu, S.; Farle, M.; Wiedwald, U.; Gökce, B., *Formation Mechanism of Laser Synthesized Iron-Manganese Alloy Nanoparticles, Manganese Oxide Nanosheets and Nanofibers*. Part.Part.Syst.Character, 2016. **34**: p. 1600225.
132. Jakobi, J.M.n.-M.n., A.; Chakravadhanula, V. S. K.; Kienle, L.; Wagener, P.; Barcikowski, S. , *Stoichiometry of Alloy Nanoparticles from Laser Ablation of PtIr in Acetone and Their Electrophoretic Deposition on PtIr Electrodes*. Nanotechnology 2011. **22**: p. 145601. .
133. Lam, J.A., D. Dujardin, C.; Ledoux, G.; Allouche, A.-R., *Atomistic mechanism for the nucleation of aluminium oxide nanoparticles*. J. Phys. chem. A, 2015. **119**.
134. Mazhukin, V.I., *Laser Ablation - From Fundamentals to Applications chapter Nanosecond Laser Ablation: Mathematical Models, Computational Algorithms, Modeling*, ed. T. Itina. 2017: Open access peer-reviewed Edited Volume.
135. Peng, H., et al., *Modeling the Phase Stability of Janus, Core–Shell, and Alloyed Ag–Cu and Ag–Au Nanoparticles*. The Journal of Physical Chemistry C, 2015. **119**(4): p. 2186-2195.
136. Srivastava, C., et al., *Size dependent microstructure for Ag–Ni nanoparticles*. Acta Materialia, 2011. **59**(16): p. 6501-6509.
137. Shih, C.Y., et al., *Two mechanisms of nanoparticle generation in picosecond laser ablation in liquids: the origin of the bimodal size distribution*. Nanoscale, 2018. **10**(15): p. 6900-6910.
138. C. Momma, B.N.C., S. Nolte, F. von Alvensleben, A. Tünnermann, H. Welling, B. Wellegehausen, , *Short-pulse laser ablation of solid targets*, . Opt. Commun., 1996. **129**: p. 134-142. .
139. R. Tanabe, T.T.P.N., T. Sugiura, Y. Ito, *Bubble dynamics in metal nanoparticle formation by laser ablation in liquid studied through high-speed laser stroboscopic videography*. Appl. Surf. Sci. , 2015. **351**: p. 327-331.
140. A. Matsumoto, A.T., A. Kawasaki, T. Honda, P. Gregorcic, N. Nishi, K. Amano, K. Fukami, and T. Sakka, *Comparison of the overall temporal behavior of the bubbles produced by short- and long pulse nanosecond laser ablations in water using a laser-beam-transmission probe*. Appl. Phys. A 2016. **122**: p. 234.
141. Mikhail E. Povarnitsyn, T.E.I., Pavel R. Levashov and Konstantin V. Khishchenko, *Mechanisms of nanoparticle formation by ultra-short laser ablation of metals in liquid environment*. Physical Chemistry Chemical Physics 2013. **15**(9): p. 3108-3114.
142. Lu, A.H., E.L. Salabas, and F. Schuth, *Magnetic nanoparticles: synthesis, protection, functionalization, and application*. Angew Chem Int Ed Engl, 2007. **46**(8): p. 1222-44.
143. Liz-Marzan, L.M., *Tailoring surface plasmons through the morphology and assembly of metal nanoparticles*. Langmuir, 2006. **22**(1): p. 32-41.

144. Streubel, R., S. Barcikowski, and B. Gokce, *Continuous multigram nanoparticle synthesis by high-power, high-repetition-rate ultrafast laser ablation in liquids*. Opt Lett, 2016. **41**(7): p. 1486-9.
145. Amendola, V., et al., *Magneto-plasmonic Au-Fe alloy nanoparticles designed for multimodal SERS-MRI-CT imaging*. Pub Med, 2014. **10**(12): p. 2476-86.
146. Swiatkowska-Warkocka, Z., et al., *Various Morphologies/Phases of Gold-Based Nanocomposite Particles Produced by Pulsed Laser Irradiation in Liquid Media: Insight in Physical Processes Involved in Particles Formation*. Journal of Physical Chemistry C, 2017. **121**(14): p. 8177-8187.
147. Langlois, C., et al., *Fully Crystalline Faceted Fe-Au Core-Shell Nanoparticles*. Nano Lett, 2015. **15**(8): p. 5075-80.
148. Calvo, F., et al., *Modeling Iron–Gold Nanoparticles Using a Dedicated Semi-Empirical Potential: Application to the Stability of Core–Shell Structures*. The Journal of Physical Chemistry C, 2017. **121**(8): p. 4680-4691.
149. Barmparis, G.D., et al., *Nanoparticle shapes by using Wulff constructions and first-principles calculations*. Beilstein J Nanotechnol, 2015. **6**: p. 361-8.
150. Baricco, M., *Metastable phases and phase diagrams*. METALLURGIA FISICA, 2004.
151. Prymak, O., et al., *Crystallographic characterization of laser-generated, polymer-stabilized 4 nm silver-gold alloyed nanoparticles*. Materials Chemistry and Physics, 2018. **207**: p. 442-450.
152. Tymoczko, A., et al., *How the crystal structure and phase segregation of Au-Fe alloy nanoparticles are ruled by the molar fraction and size*. Nanoscale, 2018. **10**(35): p. 16434-16437.
153. N. Chichkov, C.M., S. Nolte, F. von Alvensleben, A. Tünnermann, , *Femtosecond, Picosecond and Nanosecond Laser Ablation of Solids*,. Appl. Phys. A, 1996. **63**: p. 109-115.
154. Lewis, L.J. and D. Perez, *Laser ablation with short and ultrashort laser pulses: Basic mechanisms from molecular-dynamics simulations*. Applied Surface Science, 2009. **255**(10): p. 5101-5106.
155. J. Lam, D.A., F. Chaput, M. Diouf, G. Ledoux, N. Mary, K. Masenelli-Varlot, V. Motto-Ros, and C. Dujardin, *Al₂O₃ nanoparticles synthesised by pulsed laser ablation in liquids: a plasma analysis*, . Phys. Chem. Chem. Phys. , 2014. **16**: p. 963-973. .
156. Y. Xia, K.D.G., H.-C. Peng and X. Xia, , Angew. Chemie Int. Ed., 2017., 2017. **56**,: p. 60–95.
157. A. R. Tao, S.H.a.P.Y., . Small, 2008. **4**: p. 310–325.
158. J. Joo, E.J.K., J. Kang, M. Skalak, E. J. Anglin, A. P. Mann, E. Ruoslahti, S. N. Bhatia and M. J. Sailor, , Nanoscale Horizons,, 2016. **1**: p. 407–414.
159. J. Zhang, Y.H., X. Jin, A. Nazartchouk, M. Liu, X. Tong, Y. Jiang, L. Ni, S. Sun, Y. Sang, H. Liu, L. Razzari, F. Vetrone and J. Claverie, , Nanoscale Horizons, 2019. ,**4**: p. 907–917.
160. D. H. Hasenöhrl, A.S., V. Strauss, L. Wibmer, S. Klein, D. M. Guldi and A. Hirsch,, J. Mater. Chem. B., 2017. **5**: p. 8591–8599.
161. S. J. Tan, M.J.C., D. Luo and W. Cheng, Nat. Nanotechnol., 2011. **6**: p. 268–276.
162. D. Yang, X.P., Y. He, Y. Wang, G. Chen, W. Wang and Z. Lin, , Angew. Chemie, 2015. **127**: p. 12259–12264.
163. D. Dong, Q.S., D. Sikdar, Y. Zhao, Y. Liu, R. Fu, M. Premaratne and W. Cheng,, Nanoscale Horizons, 2019. **4**: p. 940–946.
164. J. Park, S.C., A. Oh, H. Jin, J. Joo, H. Baik and K. Lee, , Nanoscale Horizons, 2019. **4**: p. 727–734.
165. P.-C. Chen, J.S.D., B. Meckes, L. Huang, Z. Xie, J. L. Hedrick, V. P. Dravid and C. A. Mirkin, . J. Am. Chem. Soc., 2017. **139**: p. 9876–9884.
166. Amram, D. and E. Rabkin, *Core(Fe)-shell(Au) nanoparticles obtained from thin Fe/Au bilayers employing surface segregation*. ACS Nano, 2014. **8**(10): p. 10687-93.

167. J. Vernieres, S.S., J. Zhao, P. Grammatikopoulos, R. Ferrando, K. Nordlund, F. Djurabekova and M. Sowwan, , *Adv. Sci.*, 2019. **1900447**.
168. J. Canet-Ferrer, P.A., A. Ribera, J. V. Usagre and S. A. Maier, , *Nanoscale Horizons*, 2017. **2**: p. 205–216.
169. J. Kim, S.P., J. E. Lee, S. M. Jin, J. H. Lee, I. S. Lee, I. Yang, J.-S. Kim, S. K. Kim, M.-H. Cho and T. Hyeon, , *Angew. Chemie*, 2006. **118**: p. 7918–7922.
170. H. Fuse, N.K., Y. Ishikawa, Z. Swiatkowska-Warkocka, H. Fuse, N. Koshizaki, Y. Ishikawa and Z. Swiatkowska-Warkocka, , *Nanomaterials*, 2019. **9**: p. 198.
171. H. Wang, A.P., K. Kawaguchi, X. Li, Z. Swiatkowska-Warkocka and N. Koshizaki, *Angew. , Chemie Int. Ed.*, 2010. **49**: p. 6361–6364.
172. A. Baptista, F.J.G.S., J. Porteiro, J. L. Míguez, G. Pinto and L. Fernandes, , *Procedia Manuf.*, 2018. **17**: p. 746–757.
173. U. Seyfert, U.H., G. Teschner and J. Strümpfel, *SVC Bull.*, 2015: p. 22–26.
174. S. Wirtz, A.C., M. Labusch, G. Marzun, S. Barcikowski, D. Söffker, S. F. Wirtz, A. P. A. Cunha, M. Labusch, G. Marzun, S. Barcikowski and D. Söffker, , *Sensors*, , 2018. **18**: p. 1775.
175. V. Amendola, M.M., O. M. Bakr, P. Riello, S. Polizzi, S. Fiameni, H. Dalaver, P. Arosio, T. Orlando, C. de Julian Fernandez, F. Pineider, C. Sangregorio and A. Lascialfari, , *Nanoscale*, 2013. **5**: p. 5611–5619.
176. V. Amendola, S.S., F. Carraro and E. Cattaruzza, , *J. Colloid Interface Sci.*, 2017, 489, 18–27., 2017.
177. D. Amram, Y.A.a.E.R., *Acta Mater.*, 2016. **102**: p. 342–351.
178. C.-Y. Shih, R.S., J. Heberle, A. Letzel, M. V. Shugaev, C. Wu, M. Schmidt, B. Gökce, S. Barcikowski and L. V. Zhigilei, , *Nanoscale*, 2018. **10**: p. 6900–6910.
179. M. B. Gawande, A.G., T. Asefa, H. Guo, A. V. Biradar, D.-L. Peng, R. Zboril and R. S. Varma, , *Chem. Soc. Rev.*, 2015. **44**: p. 7540–7590.
180. Z. Luo, J.H., L. Menin, Q. K. Ong and F. Stellacci, , *Angew. Chemie Int. Ed.*, 2017. **56**: p. 13521–13525.
181. G. Beck, S.B., V. S. K. Chakravadhanula, M. Comesaña-Hermo, M. Deng, M. Farle, M. Hilgendorff, J. Jakobi, J. Janek, L. Kienle, B. Mogwitz, T. Schubert and F. Stiemke, , *Thin Solid Films*, 2015. **595**: p. 96–107.
182. V. Amendola, S.S., S. Agnoli, S. Polizzi and M. Meneghetti, , *Nanoscale*, 2014. **6**: p. 1423–1433.
183. H. Lai, F.X.a.L.W., *J. Mater. Sci.*, 2018. **53**: p. 8677–8698.
184. D. Song, R.Y., F. Long and A. Zhu, , *J. Environ. Sci.*, 2019. **80**: p. 14–34.
185. V. Amendola and M. Meneghetti, *Adv. Funct. Mater.*, 2012. **22**: p. 353–360.
186. V. Amendola, R.P., M. Frascioni, O. M. Maragò and M. A. Iati, , *J. Phys. Condens. Matter*, 2017. **29**: p. 203002.
187. K. Seshan and D. Schepis. *Handbook of Thin Film Deposition*, . 2018, Elsevier Ltd.
188. W. T. Osowiecki, X.Y., P. Satish, K. C. Bustillo, E. L. Clark and A. P. Alivisatos, , *J. Am. Chem. Soc.*, 2018. **140**: p. 8569–8577.
189. J. W. Gibbs, *Trans. Connect. Acad. Arts Sci.*, 1876. **111**: p. 108–248.
190. F. Calvo, N.C., J. Morillo and M. Benoit, , *J. Phys. Chem. C*, 2017. **121**: p. 4680–4691.
191. Y. P. Lee, Y.V.K., V. V Nemoshkalenko, R. Gontarz and J. Y. Rhee, , *Phys. Rev. B*, 2003. **67**: p. 104424.
192. K. K. Kim, M.R., H. Kwon, J. K. Song and S. M. Park, , *J. Appl. Phys.*, 2015. **117**: p. 074302.
193. S. Barcikowski, A.P., K. S. Suslick and A. Vogel, , *MRS Bull.*, 2019. **44**: p. 382–391.
194. S. Scaramuzza, M.Z.a.V.A., *J. Phys. Chem. C*, 2016. **120**: p. 9453–9463.
195. Yan, Z.B., R. Chrisey, d. B., *The generation of Ag-Ag₂O complex nanostructures by exmier laser ablation of Ag in water*. *Phys. Chem. Chem. Phys.*, 2013. **15**: p. 3052-3056.
196. Mafune, F., *Physical preparation of size-selected gold nanoaprticles in solution: laser ablation and laser induced size control*. *J. Phys. Chem. B*, 2002. **106**(7575-7577).

197. Werner, D., et al., *Examination of Silver Nanoparticle Fabrication by Pulsed-Laser Ablation of Flakes in Primary Alcohols*. The Journal of Physical Chemistry C, 2008. **112**(5): p. 1321-1329.
198. Yang, G., *Laser Ablation in Liquids: Principles and Applications in the Preparation of Nanomaterials*, ed. C. series. 2012.
199. Xiao, J., et al., *External field-assisted laser ablation in liquid: An efficient strategy for nanocrystal synthesis and nanostructure assembly*. Progress in Materials Science, 2017. **87**: p. 140-220.
200. Lam, J., *Pulsed Laser Ablation in Liquid : towards the comprehension of the growth processes*. 2015.
201. De Giacomo, A., et al., *Cavitation dynamics of laser ablation of bulk and wire-shaped metals in water during nanoparticles production*. Phys Chem Chem Phys, 2013. **15**(9): p. 3083-92.
202. Oseguera-Galindo, D.O.M.-B., A.; Guetaz, L., *Effects on the confinig solvent on the size distribution of silver NPs by laser ablation*. Nanopart. Res., 2012. **14**: p. 1133.
203. Yan, Z.B., R, Chrisey, d. B., *Hollow nanoparticle generation on laser induced cavitation bubble via bubble interface pinning*. Appl. Phys. Lett. , 2010. **97**: p. 124106.
204. Kanitz, A., et al., *Impact of liquid environment on femtosecond laser ablation*. Applied Physics A, 2017. **123**(11).
205. Waag, F., *Laser Synthesis of Metallic and Oxidic Transition Metal, Multi-Element Nanoparticles for Catalytic Applications*, in *Faculty of Chemistry Institute for Technical Chemistry I University of Duisburg-Essen*. 2019, University of Duisburg-Essen: Essen. p. 280.
206. Kamp, M.T., Anna; Schürmann, Ulrich; Jakobi, Jurij; Rehbock, Christoph; Barcikowski, Stephan; Kienle, Lorenz, *Templated dealloying: designing novel ultrastructures by memory effect*. Crystal Growth & Design, 2019.
207. Latscha, H.P., Klein, H. A., Eds.; , *Säure-Base-Systeme. In Anorganische Chemie: Chemie-Basiswissen I*. Springer Berlin Heidelberg:, ed. Springer-Lehrbuch;. 2007, Berlin, Heidelberg, .
208. Anderson, B.D. and J.B. Tracy, *Nanoparticle conversion chemistry: Kirkendall effect, galvanic exchange, and anion exchange*. Nanoscale, 2014. **6**(21): p. 12195-216.
209. Qi, W.H.W., M. P. J. , *Size and Shape Dependent Lattice Parameters of Metallic Nanoparticles*. Nanoparticle Res. , 2005. **7**(1): p. 51-57.
210. Pedireddy, S., et al., *Nanoporous Gold Bowls: A Kinetic Approach to Control Open Shell Structures and Size-Tunable Lattice Strain for Electrocatalytic Applications*. Small, 2016. **12**(33): p. 4531-40.
211. Zhang, J. and C.M. Li, *Nanoporous metals: fabrication strategies and advanced electrochemical applications in catalysis, sensing and energy systems*. Chem Soc Rev, 2012. **41**(21): p. 7016-31.
212. Kamp, M., et al., *Temperature-Dependent Ultrastructure Transformation of Au–Fe Nanoparticles Investigated by in Situ Scanning Transmission Electron Microscopy*. Crystal Growth & Design, 2018. **18**(9): p. 5434-5440.
213. Hansen, A.-L.D., T.; Winkler, M.; Ditto, J.; Johnson, and J.D.B. D. C.; Koenig, K.; Kienle, L.; Bensch, W. , *Synthesis and Thermal Instability of High-Quality Bi₂Te₃/Sb₂Te₃ Superlattice Thin Film Thermoelectrics*. Chem. Mater., 2014. **26**: p. 6518–6522.
214. Koch, C., et al., *Enhanced temperature stability and exceptionally high electrical contrast of selenium substituted Ge₂Sb₂Te₅ phase change materials*. Rsc Advances, 2017. **7**(28): p. 17164-17172.
215. Barmparis, G.D., et al., *Nanoparticle shapes by using Wulff constructions and first-principles calculations*. Beilstein Journal of Nanotechnology, 2015. **6**: p. 361-368.
216. Bals, S.V.A., S.; Van Tendeloo, G. , *High Resolution Electron Tomography* Curr. Opin. Solid State Mater. Sci. , 2013. **17**: p. 107–114.

217. Benoit, M., et al., *Structural and electronic properties of the Au(001)/Fe(001) interface from density functional theory calculations*. Physical Review B, 2012. **86**(7).
218. Petersen, S. and S. Barcikowski, *Conjugation Efficiency of Laser-Based Bioconjugation of Gold Nanoparticles with Nucleic Acids*. The Journal of Physical Chemistry C, 2009. **113**(46): p. 19830-19835.
219. Anna Tymoczko, a.M.K., Christoph Rehbock, Lorenz Kienle, Elti Cattaruzza, Stephan Barcikowski, Vincenzo Amendola, *One-step synthesis of Fe–Au core–shell magnetic-plasmonic nanoparticles driven by interface energy minimization*. Nanoscale Horiz., 2019. **4**: p. 1326-1332.
220. Favez, D., J.D. Wagnière, and M. Rappaz, *Au–Fe alloy solidification and solid-state transformations*. Acta Materialia, 2010. **58**(3): p. 1016-1025.
221. Dinega, D.P. and M.G. Bawendi, *A Solution-Phase Chemical Approach to a New Crystal Structure of Cobalt*. Angew Chem Int Ed Engl, 1999. **38**(12): p. 1788-1791.
222. Bang, J.H.a.K.S.S., *Applications of ultrasound to the synthesis of nanostructured materials*. Advanced materials, 2010. . 22 2010. **10**: p. 1039-1059.
223. Osorio-Cantillo, C.a.O.P.-P., *Synthesis and characterization of metastable nanocrystalline cobalt*. . Journal of Applied Physics,, 2019. **105**(7): p. 07A332.
224. E. Cattaruzza, G.B., F. Gonella, R. Polloni, B. F. Scremin, G. Mattei, P. Mazzoldi and C. Sada, , Appl. Surf. Sci., 2007. **254**: p. 1017–1021.
225. E. Cattaruzza, G.B., P. Riello, D. Cristofori and M. Tamisari, , Appl. Surf. Sci., 2014. **320**: p. 863–870.
226. V. Amendola, S.S., F. Carraro and E. Cattaruzza,, J. Colloid Interface Sci., 2017. **489**: p. 18–27.
227. E. C. Le Ru and P. G. Etchegoin, Chem. Phys. Lett., 2006. **423**: p. 63–66.
228. B. T. Draine and P. J. Flatau, arXiv, , 2010: p. 1002.1505.
229. B. T. Draine and P. J. Flatau, J.Opt.Soc.Am.A, 1994. **11**: p. 1491–1499.
230. J. J. Goodman, B.T.D.a.P.J.F., Opt.Lett, 1991. **16**: p. 1198–1200.
231. R. L. Olmon, B.S., T. W. Johnson, D. Shelton, S.-H. Oh, G. D. Boreman and M. B. Raschke, , Phys. Rev. B, 2012. **86**: p. 235147.
232. P. Johnson and R. Christy, Phys. Rev. B, 1974. **9**: p. 5056–5070.
233. U. Kreibig and M. Vollmer, *Optical Properties of Metal Clusters*, , ed. Springer. 1995, Berlin.
234. I. Barin, O.K.a.O.K. Thermochemical properties of inorganic substances,. 1977, Berlin, Heidelberg,: Springer Berlin Heidelberg, .
235. H. Okamoto, T.B.M., L. J. Swartzendruber and P. A. Beck, , Bull. Alloy Phase Diagrams, , 1984,. **5**: p. 592–601.
236. W. Mönch, *Semiconductor Surfaces and Interfaces*. Vol. 26. 2001, Berlin Heidelberg: Springer Berlin Heidelberg,.
237. H. Fredriksson, U.A., *Physics of functional materials*, ed. W.I.O. service). 2008: John Wiley & Sons, .
238. W. H. Qi, M.P.W., M. Zhou and W. Y. Hu, , J. Phys. D. Appl. Phys., 2005. **38**: p. 1429–1436.
239. Kittel, C., *Introduction to solid state physics*,. 2005: I Wiley,.
240. Williams, R.H., *Semiconductor surfaces and interfaces*,. Vol. 33. 1983: Springer Science & Business Media.
241. C. N. Singman, J. Chem. Educ, 1984. **61**: p. 137.

7.2 Supporting information

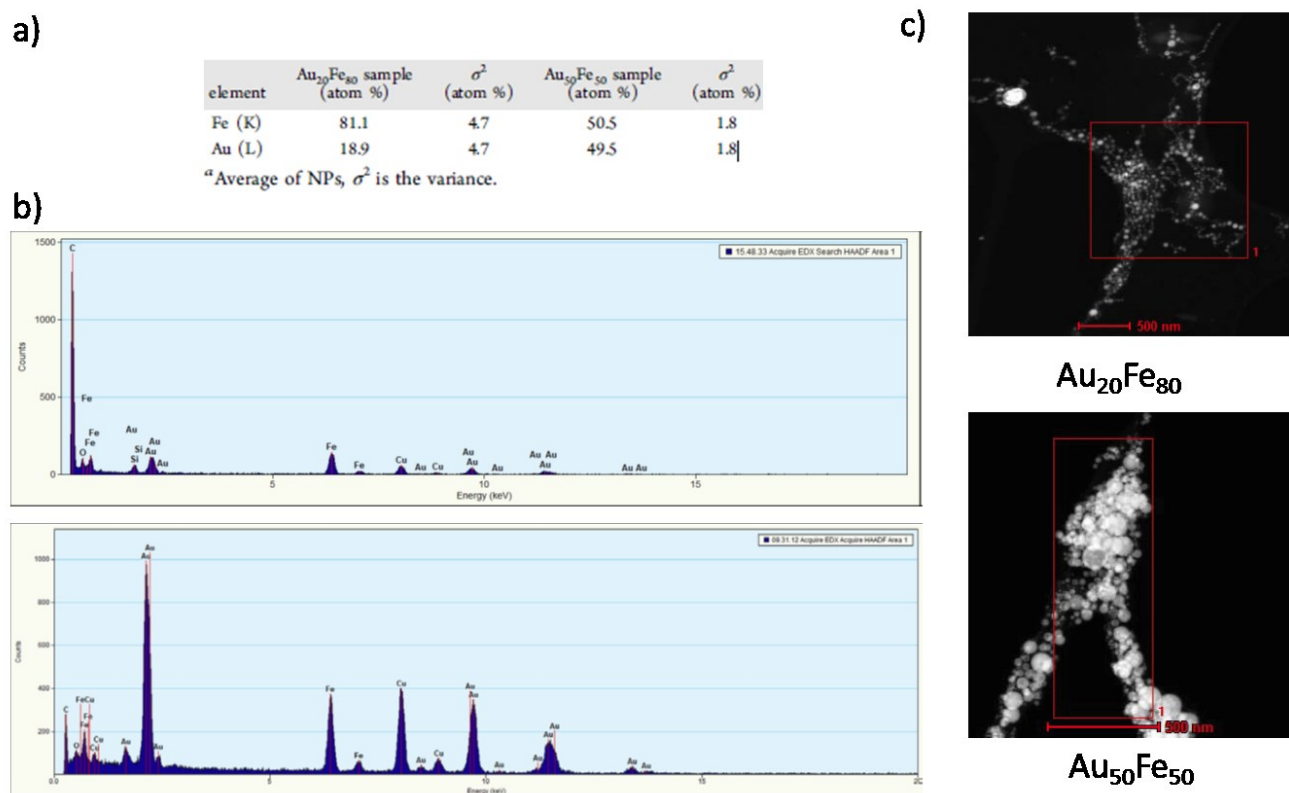
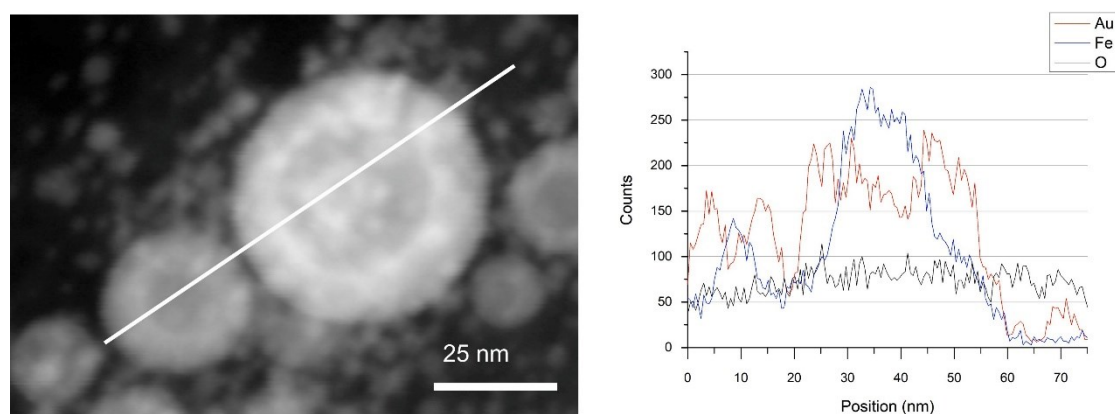


Figure S1: a) Summarized chemical composition for Au₂₀Fe₈₀ and Au₅₀Fe₅₀ from STEM-EDX analysis b) Measurements EDX spectrum for sample Au₂₀Fe₈₀ obtained from the area marked in STEM pictures shown in c); c) STEM pictures for Au₂₀Fe₈₀ (top) and Au₅₀Fe₅₀ (bottom).



How Crystal Structure and Phase Segregation of Au-Fe Alloy Nanoparticles is ruled by Molar Fraction and Size

Experimental Section

Au-Fe nanoparticles synthesis

For all studies Au-Fe alloy targets (fem Institut für Edelmetalle und Metallchemie, Schwäbisch Gmünd) with varied Au:Fe atomic % ratio (10:90, 20:80, 35:65, 50:50, 65:35, 80:20 and 90:10) were ablated in Acetone 99.98 % (Carl-Roth GmbH, Karlsruhe). LAL was performed with a 10 ns Nd:YAG laser (Rofin Sinar Technologies, Plymouth) at 1064nm with a repetition rate of 15 kHz and a fluence 3.85 mJ/cm². A lens with a focal length of 100 mm was used to focus the beam through a glass window into the batch reactor containing the Au-Fe alloy target emerged in 30 mL acetone. The alloy target was placed vertically to the bottom of the batch-chamber. Additionally, an electrical motor was mounted at the back of the chamber to assure a constant flow of the ablated material, avoiding absorption of the laser energy by already generated NPs. The amount of ablated mass was determined gravimetrically by weighing the target before and after laser ablation using a microbalance.

Particle analysis

The size and the internal composition of LAL generated Au-Fe nanoparticles were determined using transmission electron microscopy STEM-HAADF (FEI, Tecnai F30 G² STWIN). 10 µL of the colloid dispersion were pipetted onto a carbon-coated copper microgrid and dried overnight. The ferret diameter of the sample was measured for weighted 1000 nanoparticles each. The results were plotted both as to the number and volume-weighted distribution and fitted using a log-normal function. The average particle size was obtained from the Xc values of this fit. Energy dispersive x-ray spectroscopy is a suitable method for quantitative elemental detection of the iron gold system. Thus differentiation of the elements and corresponding oxide is distinct. EDX results are obtained by STEM-EDX measurements with Phillips XL 30 with EDAX DX-4. Therefore, different kind of EDX spectra is generated. The integration over a large number of nanoparticles confirms the coincidence of target and nanoparticle composition. Based on Z-contrast of STEM-HAADF imaging mode, a distinct hint of the ultrastructure is possible. EDX mapping and line scans characterize the existence

of the CS ultrastructure in each sample. Furthermore, the absence of oxidation especially in the iron core of Au@Fe nanoparticles was proved by this method. By means of X-ray powder diffraction (XRD) using a Bruker D8 Advance diffractometer (Cu K α radiation, $\lambda = 1.54 \text{ \AA}$; 40 kV, 40 mA) a phase composition of all targets and produced Au-Fe NPs was determined. The target materials were positioned in the sample holder. All nanoparticle samples were prepared from a high concentrated colloid homogeneously distributed on a silicon single crystal to minimize scattering. To determine the phase ratios, lattice parameters and percentage of the Fe/Au substitution in the FCC and BCC structures as well as to estimate the average crystallite sizes from diffraction peak broadening reflections (using the Scherrer equation), the Rietveld refinement was performed with the Bruker software TOPAS 4.2. The patterns of cubic Au-FCC (#004-0784) and Fe-BCC (#006-0696) phases from the ICDD database were used as a reference for the qualitative phase analysis, which was done with a Diffrac. suite EVA V1.2 from Bruker.

Characterization of Au-Fe laser-generated nanoparticles

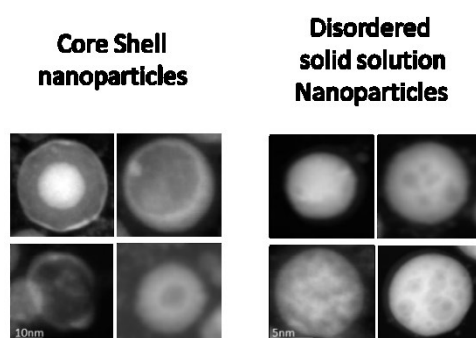


Figure S3: Representation of possible Au-Fe alloy ultrastructure generated via LAL in Acetone. The structure of Au-Fe bimetallic nanoparticle can be defined by distribution mode of the two elements and its orientation is described as a) Core Shell arrangement with clearly defined segregated Au-Fe phase boundary (Core Shell nanoparticles) b) randomly mixed alloy structure (disordered solid solution nanoparticles).

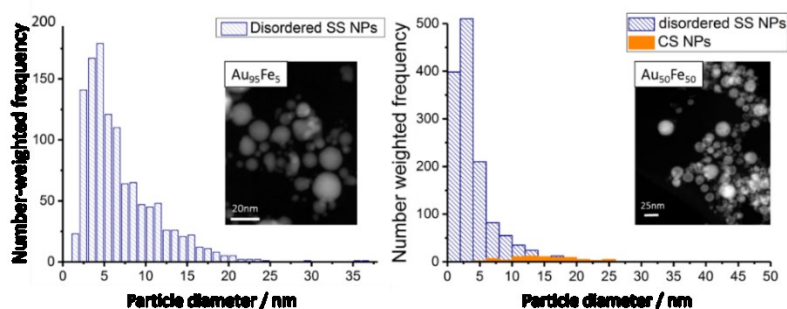


Figure S4: Two representative number-weighted particle size histograms for LAL generated Au₉₅Fe₅ and Au₅₀Fe₅₀ nanoparticles analyzed by HAADF STEM (blue bars Disordered Solid Solution NPs, orange bars Core-Shell NPs).

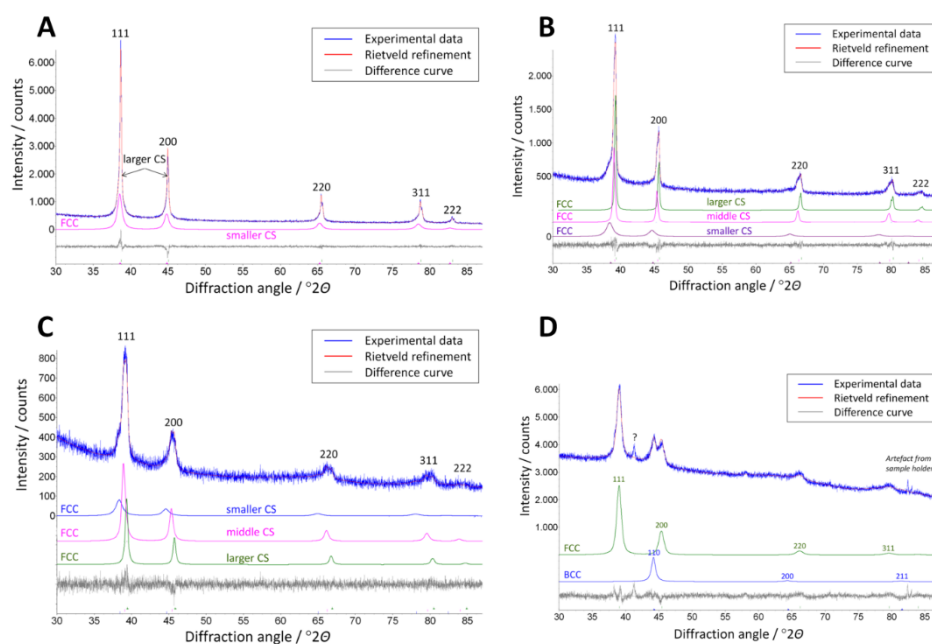


Figure S5: Representative X-ray powder diffractograms with Rietveld refinement of Au₈₀Fe₂₀ (A), Au₆₅Fe₃₅ (B), Au₅₀Fe₅₀ (C) and Au₂₀Fe₈₀ (D) nanoparticles with additionally denoted FCC and BCC phases (incl. multiply FCC peak profiles with smaller-larger crystallite sizes, CS) for the investigated Au-Fe nanoparticles. One non-identified reflection peak (?) probably belongs to Iron-oxide phase, which is observed for the Au-Fe nanoparticles with BCC-phase.

	Au ₅₀ Fe ₅₀	Fe bcc	Au _{71.2} Fe _{28.2}
Au₅₀Fe₅₀	SS	Core	shell
2.30	2.24		2.31
2.08		2.04	
2.00	1.94		2.00
1.41	1.37	1.44	1.41
1.18	1.17	1.18	1.21
1.12	1.12		1.15
0.99	0.97	1.02	1.00
0.91	0.89	0.91	0.92

Figure S6: Table with an overview for SAED patterns obtained experimentally for Au₅₀Fe₅₀ with fitted diffraction patterns.

One-Step Synthesis of Fe-Au Core-Shell Magnetic-Plasmonic Nanoparticles Driven by Interface Energy Minimization

Materials and methods.

1. Thin film preparation.

Fe-Au films were prepared at room temperature by radiofrequency magnetron multitarget sputtering deposition of iron and gold, in pure Ar atmosphere at a working pressure of 40×10^{-4} mbar. Two different 13.56 MHz radiofrequency sources were used

for iron and gold, respectively. Substrates were sodalime glass slides cleaned according to a previously published procedure.[224] Before deposition, the soda-lime substrates were rf-biased at 20 W for 20 min, to remove possible surface contaminants (removed layer thickness around 10 nm). During deposition, the sample holder was rotating at 10 Hz. The rf power to the 2 in. diameter targets was 40 W for iron and 20 W for gold. Different deposition times were used to obtain layers of the prescribed thickness. The final thickness of the different layers was measured by Rutherford backscattering spectrometry (RBS) by using a 2.2 MeV 4He^+ beam.[225] The incident direction was normal to the sample surface, and scattered particles were detected at the angle of 160° . For each deposition, different RBS measurements were performed in randomly selected film points. Film thickness was calculated by using the density value of the bulk phases. Relative random uncertainty on film thickness was less than 2% in all films.

Film thickness and corresponding Fe: Au ratios are reported in Table S1 below:

Table S1. Film thickness

Film type	Thickness	Fe: Au ratio
Au+Fe/glass	76 nm	0.90
Fe/Au/glass	32 nm / 45 nm	1.03
Au/Fe/Au/Fe/glass	21 nm / 17 nm / 22 nm / 17 nm	1.13
Au/Fe/glass	43 nm / 33 nm	1.10

2. Laser ablation synthesis.

LASiS was performed in Acetone (HPLC Plus, >99.9%, Sigma-Aldrich) adapting a previously described procedure,[226] with either 6 ns, 1064 nm pulses of a Nd:YAG laser with pulse energy of 22.6 mJ and fluence of 3.1 J/cm^2 , or 10 ps, 1064 nm pulses of a Nd:YAG laser with pulse energy of 0.08 mJ and fluence of 4 J/cm^2 . The film targets were placed in acetone at the bottom of the glassy batch-chamber, and ablated from the top. The focal point was moved at each laser pulse in order to ablate a different point of the film at each single laser pulse, with a minimum distance of 0.2 mm between each ablation crater.

Coating with NTP was performed in two steps: first, the thiol was added to the NPs dispersion in acetone with a final concentration of 10^{-3} M , then the NPs were attracted with a permanent NdFeB magnet at the bottom of the vial, the supernatant removed,

and fresh liquid solution added again. The latter procedure was repeated 7 times. Finally, NPs were redispersed by ultrasounds and drop casted on a soda-lime microscope slide embedded between two permanent NdFeB magnets to obtain NPs alignment during liquid evaporation.

3. Analysis of nanoparticles.

UV-vis spectroscopy of nanoparticle colloidal suspension in acetone was performed using a Cary 5 UV-vis-NIR spectrophotometer in 1 cm quartz cuvettes. Stability of the laser synthesized colloids was also assessed by UV-vis spectroscopy, by monitoring absorbance over time (an example is reported in Figure S1 below).

In experiments of Figures 2B-C, Raman spectra were collected with a 50X microscope objective of a DXR ThermoScientific microRaman equipped with a 532 nm laser. NPs were deposited on a microscope slide embedded between two permanent NdFeB magnets, as described above. MG solutions (10000, 500, 200, 100, 50 and 10 nM) were drop casted (1000 nL each drop) onto NPs spots before collection of Raman spectra.

For experiments of Figure 2E, a 10X objective and a piezo stage were used for collecting bidimensional Raman maps on the areas delimited by the red square in the optical microscope images shown in the same Figure. The maps were collected on an area of 1500 x 1600 μm^2 at 532 nm with acquisition time of 30 s for each point and a power of 1.5 mW. Maps of Figure 2E refer to the Raman spectrum intensity at 1615 cm^{-1} . For accumulation of CS NPs, a cylindrical NdFeB permanent magnet (2 mm in diameter for 8 mm length) was placed below the glass substrate before drop casting of the aqueous solution. Colloid concentration is indicated in the main text. For this experiment, CS NPs were obtained in the following way: the colloid as obtained from LASiS was placed in a glass vial on top of a 40 mm x 40 mm NdFeB permanent magnet; after 3 h acetone was completely removed with a micropipette and replaced with distilled water, and NPs were redispersed by ultrasounds. As a reference, commercial citrate stabilized 50 nm Au NPs were used (Sigma Aldrich) at a final concentration of 22 $\mu\text{g}/\text{mL}$.

The size and the internal composition of laser-generated NPs were determined using transmission electron microscopy (FEI Tecnai F30 STWIN G) in STEM HAADF or EDS modality. 10 μL of each colloid dispersion were pipetted onto a carbon-coated copper

microgrid and dried overnight. The Feret diameter of the sample was measured for a minimum of 500 NPs for each sample with help of Image J software.

4. Numerical calculations.

G_{SERS} was evaluated as the 4th power of the ratio between the local electric field E_{loc} in the proximity to the surface of the metal nanostructure and the incident electric field E_0 from a linearly polarized 532 nm electromagnetic radiation, according to ref.[182, 186, 227]. E_{loc} was calculated by the discrete dipole approximation (DDA) method using the DDSCAT 7.1 and the relative DDFIELD packages.[228] The Fe-Au CS dimer of Figure 2D was built with two spheres of, respectively, 70 and 62 nm in external diameter and 52 and 46 nm in core diameter, with an interparticle gap of 2 nm. The final target resulted in $6.5 \cdot 10^5$ dipoles and interdipole spacing lower than 1 nm. The Fe-Au CS dimer of Figure S3A was built with two equal spheres of 22.4 nm in external diameter (according to the average NPs diameter extracted from the size histogram of Figure 1F) and 4.4 nm in shell thickness (according to the average NPs shell thickness extracted from the histogram in Figure S3B), and with an interparticle gap of 1 nm. The final target resulted in $7.6 \cdot 10^5$ dipoles and interdipole spacing lower than 1 nm. For metal particles in the 2–200 nm size range, an error smaller than 10% is achieved using a number of dipoles at least of the order of 10^4 and using an interdipole spacing much smaller than the wavelength of interest,[228-230] as in the present case. The optical constants of Au and Fe were obtained from ref.[231] and [232] respectively. The optical constants were corrected for the particle size, as reported previously.[186, 233]

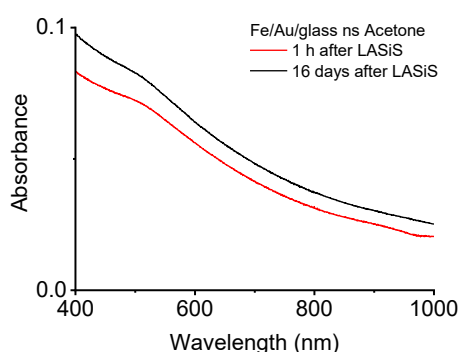


Figure S7: UV-vis spectra of the colloid obtained by ns LASiS with the Fe/Au/glass film in acetone, collected 1 h (black line) and 16 days (red line) after the synthesis. A limited decrease in absorbance is observed after 16 days, that is still the 87 ± 1 % of its value 1h after LASiS.

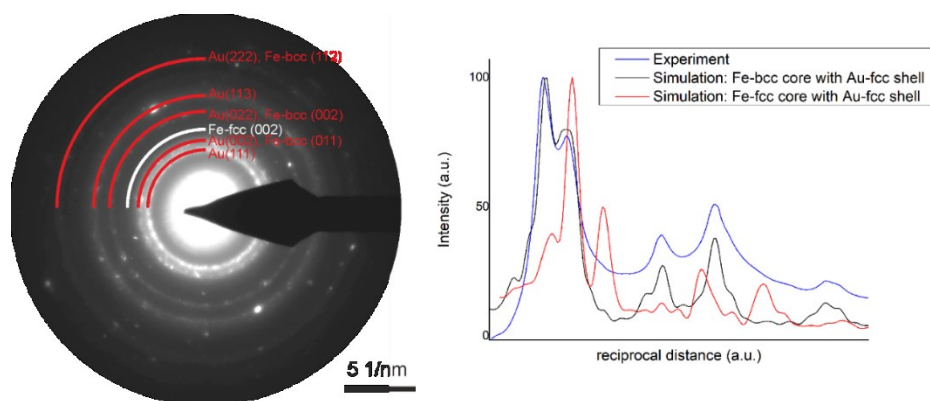


Figure S8: Left: SAED pattern of Fe-Au CS NPs synthesized from alloy target. The intensity is distributed on concentric rings, which coincides with the intensities of Au-fcc and Fe-bcc phase (the respective lattice planes are indicated in red). By superimposing of the lattice spacing (Au-fcc and Fe-bcc) a direct assignment to the Fe-bcc phase is not possible, except when all further phases of Fe can be precluded. The only additional known stable metal iron phase is Fe-fcc. However, the position of the Fe-fcc (002) reflection (marked in white) shows no intensity in the experiment, confirming the absence of this phase. Right: Rotational average intensity profiles of the experiment (blue line) and the simulations for a CS NP with Au fcc shell and Fe-bcc (black line) and Fe-fcc (red line) core. The presence of Fe-fcc can be excluded by comparing the simulated diffraction intensities, overall indicating that the SAED pattern is compatible with a nanostructure containing Au-fcc and Fe-bcc.

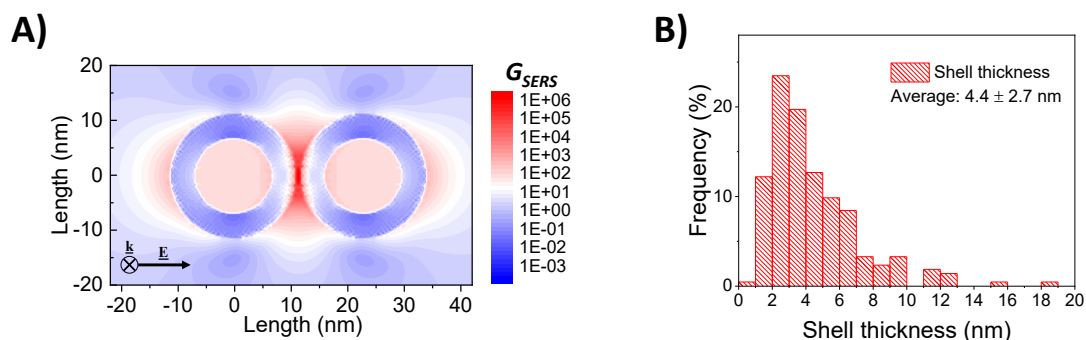


Figure S9: a) Bidimensional map of SERS enhancement factor (G_{SERS}) for 532 nm excitation, calculated for a dimer of CS NPs with average size of 22.4 nm (according to the size histogram reported in Figure 1F) and shell thickness of 4.4 nm (according to the TEM measured histogram of shell thickness reported in Figure S3B).

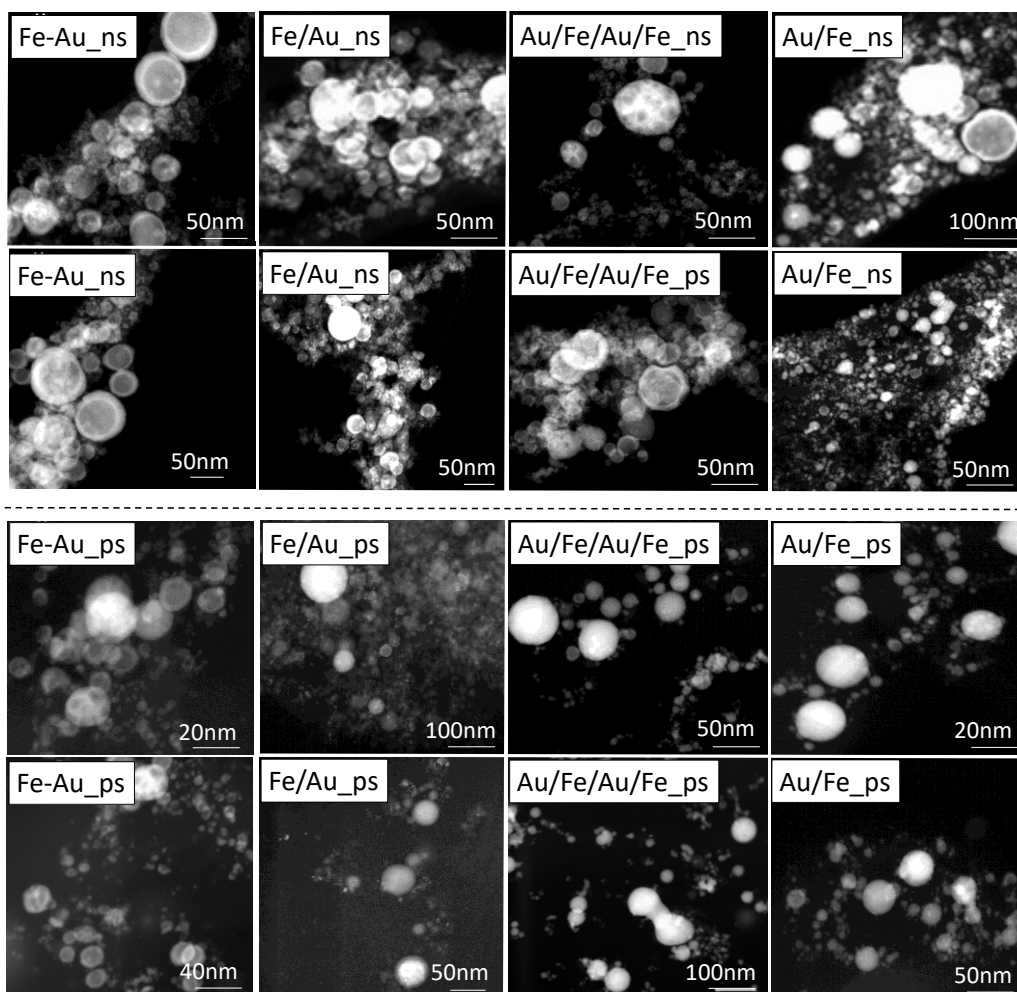


Figure S10: Representative STEM-HAADF pictures for all samples.

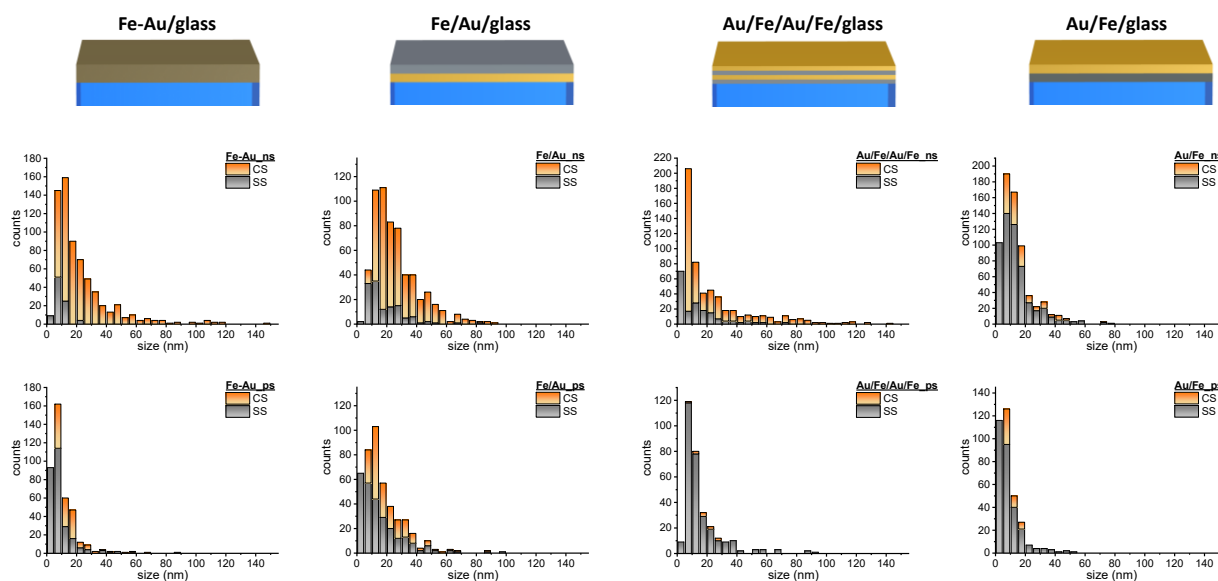


Figure S11: Cumulative histogram (CS+SS counts) showing number-weighted particle diameter distribution for all synthesized Fe-Au colloids.

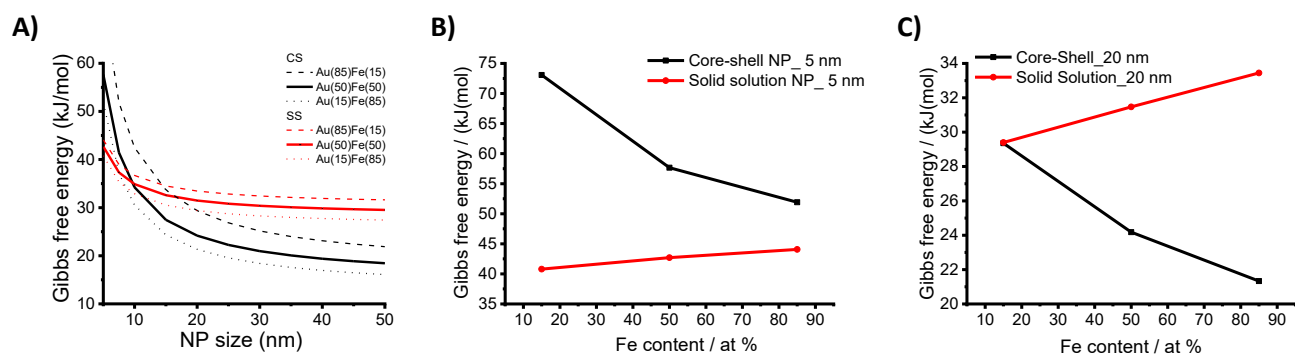


Figure S12: (A) Plot of Gibbs free energy calculated for SS (red lines) and CS (black lines) as a function of NPs size, and for three representative compositions: Fe(15)Au(85) (dashed lines), Fe(50)Au(50) (continuous lines), and Fe(85)Au(15) (dotted lines). (B-C) Plot of Gibbs free energy for CS (black dots) and SS (red dots) for the three compositions, for nanospheres with size of 5 nm (B) and 20 nm (C).

S5. Thermodynamic model for Gibbs free energy in SS and CS NPs.[136]

The Gibbs free energy (G) was separately calculated for solid solution (SS) and core-shell (CS) nanoparticles. In the SS there is a homogeneous distribution of both elements within the particle, while the CS is composed by an iron core covered by a gold shell. Besides, the thermodynamic model only considers spherical particles with no faceting involved, therefore average surface energy values can be used, namely differences in interface/surface energies for different facets are ignored. It is also assumed that there is no stress at the interface, according to analogous studies reported in literature.[136] [188] Finally, interactions with the solvent are not considered in this model.

Model for calculation of the Gibbs free energy for SS NPs (G_{SS})

$$\mathbf{G}_{SS} = \mathbf{X}_{Au}\mathbf{G}_{Au} + \mathbf{X}_{Fe}\mathbf{G}_{Fe} + \Delta\mathbf{G}_{mix} + (2\gamma_{ss}\mathbf{V}_{AuFe})/(\mathbf{D}/2) \quad (\text{eq. S1})$$

with

D: the diameter of the particle

X_{Fe} , **X_{Au}** : the mole fraction of Au and Fe respectively

G_{Au} , **G_{Fe}** : the molar free energies of pure Au ($G_{Au} = -14.1\text{kJ/mol}$) and Fe ($G_{Fe} = -7.95\text{kJ/mol}$)[234]

$\Delta\mathbf{G}_{mix} = \Delta H_{mix} - T\Delta S_{mix}$: the excess free energy of the alloy phase due to mixing ($\Delta G_{mix} = 39.296\text{kJ/mol}$)[235]

γ_{ss} : the size dependent specific surface energy (surface energy per unit area) of the nanoparticle with solid solution of Au and Fe atoms, given by

$$\gamma_{ss} = \mathbf{N} E_s(\mathbf{D}) / \pi\alpha\mathbf{N}_A\mathbf{D}^2 \quad (\text{eq. S2})$$

with

N : the number of atoms on the surface of a particle of diameter **D** with fcc solid solution structure, that is

$$\mathbf{N} = \pi\alpha\mathbf{f}^{-2/3}\mathbf{n}^{2/3}$$

with

α : the shape factor (defined as the surface area ratio of non-spherical and spherical nanoparticles of identical volumes); $\alpha = 1$ for spherical nanoparticles[235]

f : the packing fraction for different structures; 0.74 was used for fcc cell

n : total number of atoms in the particle

with

$$n = R^3/r^3$$

$R = D/2$: the radius of the nanoparticle

r : the composition weighted average of r_{Au} and r_{Fe} , the atomic radii of the elements in the fcc cell, given by

$$r_{Au} : 0.288 \text{ nm (for fcc structure)} [236]$$

$$r_{Fe} : 0.258 \text{ nm (for fcc structure)} [237]$$

$E_s(D)$: the size-dependent specific surface energy for a particle, given by [136, 238]

$$E_s(D) = \{2 - [Z_s(D)/Z_b] - [Z_s(D)/Z_b]^{1/2}\} E_{ci}(D)/2$$

with

$$E_{ci}(D) = E_c(D) / \{1 - p(D) \{2 - [Z_s(D)/Z_b] - [Z_s(D)/Z_b]^{1/2}\} / 2$$

where:

$p(D) = N_s(D)/N_{tot}(D)$: the relation between the total number of atoms present on the surface, $N_s(D)$, and inside a particle, $N_{tot}(D)$, of a given size, respectively

$Z_s(D)$: size dependent average coordination number of surface atoms

Z_b : average coordination number of the internal atoms

$E_c(D)$: size and composition dependent cohesive energy, given by

$$E_c(D) = X_{Au} E_{Au} (1 - (\alpha D^2 / n d_{Au}^2)) + X_{Fe} E_{Fe} (1 - (\alpha D^2 / n d_{Fe}^2)) - X_{Au} X_{Fe} A$$

X_{Au} , X_{Fe} : the molar fraction of Au and Fe, respectively

E_{Au} , E_{Fe} : the bulk cohesive energies of Au and Fe, respectively

$$E_{Au} = 368 \text{ kJ/mol} [239]$$

$$E_{Fe} = 413 \text{ kJ/mol} [235]$$

d_{Au} , d_{Fe} : the atomic diameters of Au and Fe, respectively

n : the total number of atoms in the particle

A : interaction parameter with a value of 60 kJ/mol [235]

N_A : Avogadro's number

and resulting in:

Table S2. The size dependent specific surface energy (surface energy per unit area) of the Au-Fe solid solution nanoparticle for three representative compositions

NPs size / nm	$\gamma_{ss}(d_{Au}, d_{Fe})$ (J/m ²)		
	Au ₁₅ Fe ₈₅	Au ₅₀ Fe ₅₀	Au ₈₅ Fe ₁₅
5	2.1	2.09	1.88
7.5	2	1.96	1.77
10	2	1.91	1.72
15	1.99	1.87	1.69
20	1.98	1.85	1.67
25	1.97	1.84	1.66
30	1.96	1.83	1.65
35	1.96	1.83	1.65
40	1.95	1.83	1.65
45	1.95	1.82	1.65
50	1.95	1.82	1.65
60	1.95	1.82	1.65
70	1.95	1.82	1.65
120	1.95	1.82	1.65
170	1.95	1.82	1.65

V_{AuFe} : the molar volume of fcc AuFe solid solution, with

$$V_{AuFe} = X_{Au} \cdot V_{Au} + X_{Fe} \cdot V_{Fe}$$

Calculated and summarized in Table S3:

Table S3. Calculated molar volume values for three representative compositions.

Au:Fe at %	V/ cm ³ /mol
Au	10.21
Au ₈₅ Fe ₁₅	9.96
Au ₅₀ Fe ₅₀	8.55
Au ₁₅ Fe ₈₅	7.4
Fe	6.93

With V_{Au} and V_{Fe} being the molar volume of pure iron and gold, respectively.

Model for calculation of the Gibbs free energy for CS NPs (G_{CS})

$$G_{CS} = X_{Au}G_{Au} + X_{Fe}G_{Fe} + \alpha_{Au}S_{Au} \gamma_{Au} + \alpha_{Fe}S_{Fe} \gamma_{Fe} + G_{int} \quad (eq. S3)$$

with

X_{Fe} , X_{Au} : the mole fraction of Au and Fe respectively

G_{Au} , G_{Fe} : the molar free energies of pure Au ($G_{Au} = -14.1$ kJ/mol) and Fe ($G_{Fe} = -7.95$ kJ/mol)[234]

α_{Au} , α_{Fe} : the fractions of surface atoms of Au and Fe vs the total number of Au and Fe atoms in the particle, where

$$\alpha_{Fe} = N_{Fe}/n_{Fe}$$

$$\alpha_{Au} = N_{Au}/n_{Au}$$

with

n_{Au} , n_{Fe} : total number of Au or Fe atoms, that for a core-shell is given by

$$n_{Fe} = R_{Fe}^3/r_{Fe}^3f_{Fe}$$

$$n_{Au} = R_{Au}^3/r_{Au}^3f_{Au} - R_{Fe}^3/r_{Au}^3f_{Au}$$

with

f_{Au} , f_{Fe} : the packing fraction for Au and Fe structures. 0.74 was used for fcc structure and applied for Au and 0.68 was used for bcc structure applicable to Fe

r_{Au} , r_{Fe} : the atomic radii of the Au or Fe structure

r_{Au} : 0.288 nm (for fcc structure)[240]

r_{Fe} : 0.248 nm (for bcc structure)[237]

N_{Au} , N_{Fe} : number of the surface atoms of Au or Fe, given by

$$N_{Fe} = \pi\alpha f_{Fe}^{-2/3}n_{Fe}^{2/3}$$

$$N_{Au} = \pi\alpha f_{Au}^{-2/3}n_{Au}^{2/3}$$

with

α : the shape factor (defined as the surface area ratio of non-spherical and spherical nanoparticles of identical volumes); $\alpha = 1$ for spherical nanoparticles[238]

$R_{Au/Fe}$: the radius of the iron core for Fe, or the radius of the whole particle for Au, as illustrated in the following Figure S7.

Core-Shell nanoparticle

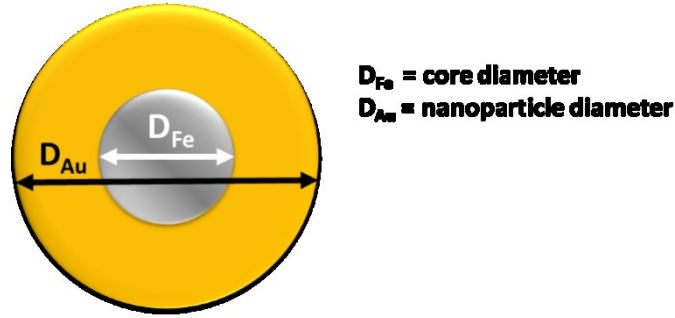


Figure S13: Schematic representation illustrating how core and shell diameters are identified.

The diameter of the iron core was calculated based on simple geometric assumptions. The following Table S4 depicts the Fe-core diameters in correlation with particle composition and overall particle diameter:

Table S4. Atomic versus Volume fraction in CS NPs.

Atomic versus Volume fractions in CS NPs with different Fe content	
atomic %	Vol %
85	80
50	41
15	11

S_{Au} , **S_{Fe}**: the surface areas occupied by 1 mole of atoms of Au and Fe, respectively, where

$$S_{Au} = 4.3 \times 10^4 \text{ m}^2$$

$$S_{Fe} = 3.2 \times 10^4 \text{ m}^2$$

γ_{Au} , **γ_{Fe}** : the size dependent specific surface energy (surface energy per unit area) of the nanoparticle for either Au and Fe atoms, given by:

$$\gamma_{Fe} = N_{Fe} E_s(D_{Fe}) / \pi \alpha N A D_{Fe}^2 [\text{Jm}^{-2}] \quad (\text{eq. S4a})$$

$$\gamma_{Au} = N_{Au} E_s(D_{Au}) / \pi \alpha N A D_{Au}^2 [\text{Jm}^{-2}] \quad (\text{eq. S4b})$$

with

N_{Au} , N_{Fe} : the number of atoms on the surface of a particle of diameter D_{Au} , D_{Fe} (for γ_{Au} the particle surface is equal to the surface of the NPs (Au is outside), while for γ_{Fe} the surface of the iron core is assumed, Figure S7).

$$N_{Au/Fe} = \pi \alpha f_{Au/Fe}^{-2/3} n_{Au/Fe}^{2/3}$$

with

α : the shape factor (defined as the surface area ratio of non-spherical and spherical nanoparticles of identical volumes) $\alpha = 1$ for spherical nanoparticles[238]

f_{Au} , f_{Fe} : the packing fraction for different structures. 0.74 was used for FCC structure and applied for Au and 0.68 was used for BCC structure applicable to Fe

$$n_{Au/Fe} = R_{Au/Fe}^3 / r_{Au/Fe}^3 f_{Au/Fe}$$

with

r_{Au} , r_{Fe} : the atomic radii of Au and Fe in the respective structures

r_{Au} : 0.288 nm (for fcc structure)

r_{Fe} : 0.248 nm (for bcc structure)

R_{Au} , R_{Fe} : the radii of spherical nanocrystal; for Fe we assumed the radius of the iron core, while for Au we assumed the diameter of the whole particle as illustrated in Figure S7.

$E_s(D_{Au})$, $E_s(D_{Fe})$: size-dependent specific surface energy for a particle of size

D_{Au} or D_{Fe}

For each metal (Au or Fe):

$$E_s(D) = \{2 - [Z_s(D)/Z_b] - [Z_s(D)/Z_b]^{1/2}\} E_{ci}(D) / 2$$

$$E_{ci}(D) = E_c(D) / \{1 - p(D) \{2 - [Z_s(D)/Z_b] - [Z_s(D)/Z_b]^{1/2}\} / 2$$

$$p(D) = N_s(D) / N_{tot}(D)$$

where:

$Z_s(D)$: size dependent average surface coordination number of the metal

Z_b : the average coordination number of the internal atoms of the metal

$E_c(D)$: size and composition dependent cohesive energy for that metal

$$E_c(D_{Au}) = E_{Au} (1 - (\alpha D_{Au}^2 / n_{Au}^2))$$

$$E_c(D_{Fe}) = E_{Fe} (1 - (\alpha D_{Fe}^2 / nd_{Fe}^2))$$

with

E_{Au} , E_{Fe} : the bulk cohesive energies of Au and Fe, respectively.

E_{Au} : 368 kJ/mol

E_{Fe} : 413 kJ/mol

D_{Au} , D_{Fe} : the radii of spherical nanocrystal; for Fe we assumed the radius of the iron core, while for Au we assumed the diameter of the whole particle as illustrated in Figure S7.

d_{Au} , d_{Fe} : are the atomic diameters of Au and Fe, respectively.

N : total number of atoms in the particle

$p(D)$: is the relation between the total number of atoms present on the surface

$N_s(D)$ and

inside a particle $N_{tot}(D)$ of a given size, respectively

α : the shape factor (defined as the surface area ratio of non-spherical and spherical nanoparticles of identical volumes); $\alpha = 1$ for spherical nanoparticles

G_{int} : the Gibbs free energy contribution given by the geometrical (γ_{geo}) and chemical (γ_{chem}) factors, that can be written as:

$$G_{int} = A (\gamma_{geo} + \gamma_{chem})$$

(eq. S5)

$$\gamma_{geo} = (F/2) (\gamma_{Au} + \gamma_{Fe}) \quad (eq. S5a)$$

$$\gamma_{chem} = \{X_{Au} \Delta H_{Au_in_Fe} / [C_o(V_{Au})^{2/3} + X_{Fe} \Delta H_{Fe_in_Au} / [C_o(V_{Fe})^{2/3}]\} \quad (eq. S5b)$$

Resulting in:

$$G_{int} = A [(0.33/2) (\gamma_{Au} + \gamma_{Fe})] + \{X_{Au} \Delta H_{Au_in_Fe} / [C_o(V_{Au})^{2/3} + X_{Fe} \Delta H_{Fe_in_Au} / [C_o(V_{Fe})^{2/3}]\} \quad (eq. S6)$$

with

A : surface area occupied by 1 mole of interfacial atoms, as described in Table

S5 below

Table S5. Calculated values for surface area occupied by 1 mole of interfacial atoms

Au:Fe at %	A / m²
Au	4.3 x 10 ⁴
Au ₈₅ Fe ₁₅	4.13 x 10 ⁴
Au ₅₀ Fe ₅₀	3,79 x 10 ⁴
Au ₁₅ Fe ₈₅	3.36 x 10 ⁴
Fe	3.2 x 10 ⁴

F = 0.33 : The multiplication factor of 0.33 is based on the assumption that the grain boundary energy is 30 % of the surface energy at 0 K[136]

$\Delta H_{\text{Au_in_Fe}}$, $\Delta H_{\text{Fe_in_Au}}$: the heat of solution of Au in Fe (or Fe in Au) at infinite dilution, according to ref.[136]

γ_{Au} , γ_{Fe} are calculated based on eq. S4 and are summarized in Table S6

Table S6. Calculated values for size dependent surface energies for Au₅₀Fe₅₀

NPs size (nm)	γ_{Au} (Jm⁻²)	γ_{Fe} (Jm⁻²)
5	0.00173	0.00221
7.5	0.00164	0.00211
10	0.0016	0.00208
15	0.00157	0.00205
20	0.00155	0.00204
25	0.00154	0.00203
30	0.00154	0.00203
35	0.00153	0.00202
40	0.00153	0.00202
45	0.00153	0.00202
50	0.00153	0.00202

X_{Au} , **X_{Fe}** : are the molar fraction of Au and Fe, respectively

ΔH : is the heat of solution of Au in Fe (or Fe in Au) at infinite dilution, where[238]

$$\Delta H_{\text{Au_in_Fe}} = 8 \text{ kJ/mol}$$

$$\Delta H_{\text{Fe_in_Au}} = 6 \text{ kJ/mol}$$

C₀ : is a constant being 4.5 x 10⁸.

V : are the molar volumes of Au and Fe, respectively, where[241]

$$V_{\text{Au}} = 10.21 \text{ cm}^3/\text{mol} \text{ for Au fcc}$$

$$V_{\text{Fe}} = 7.09 \text{ cm}^3/\text{mol for Fe bcc}$$

An example of Gibbs free energy for three representative compositions of Fe-Au CS NPs is reported in the previous Figure S6.

S5-1. Updated calculations

1. Primary equation as described above (pure iron core and pure gold shell) –Figure S16 a)

$$G_{\text{ss}} = X_{\text{Au}}G_{\text{Au}} + X_{\text{Fe}}G_{\text{Fe}} + \Delta G_{\text{mix}} + (2\gamma_{\text{ss}}V_{\text{AuFe}})/(D/2)$$

$$G_{\text{CS}} = X_{\text{Au}}G_{\text{Au}} + X_{\text{Fe}}G_{\text{Fe}} + \alpha_{\text{Au}}S_{\text{Au}} \gamma_{\text{Au}} + \alpha_{\text{Fe}}S_{\text{Fe}} \gamma_{\text{Fe}} + G_{\text{int}}$$

D - particle diameter

2. Adapted equation for CS NPs with diameter (pure iron core and pure gold shell) – Figure S16 b)

$$G_{\text{ss}} = X_{\text{Au}}G_{\text{Au}} + X_{\text{Fe}}G_{\text{Fe}} + \Delta G_{\text{mix}} + (2\gamma_{\text{ss}}V_{\text{AuFe}})/(D/2)$$

$$G_{\text{CS}} = X_{\text{Au}}G_{\text{Au}} + X_{\text{Fe}}G_{\text{Fe}} + \alpha_{\text{Au}}S_{\text{Au}} \gamma_{\text{Au}} + \alpha_{\text{Fe}}S_{\text{Fe}} \gamma_{\text{Fe}} + G_{\text{int}}$$

D – considered separately for D_{Au} and D_{Fe} (Figure S15)

3. Adapted equation with AuFe alloy shell and pure iron core – Figure S16 c)

$$G_{\text{ss}} = X_{\text{Au}}G_{\text{Au}} + X_{\text{Fe}}G_{\text{Fe}} + \Delta G_{\text{mix}} + (2\gamma_{\text{ss}}V_{\text{AuFe}})/(D/2)$$

$$G_{\text{CS}} = X_{\text{AuFe}}G_{\text{AuFe}} + X_{\text{Fe}}G_{\text{Fe}} + \alpha_{\text{AuFe}}S_{\text{AuFe}} \gamma_{\text{AuFe}} + \alpha_{\text{Fe}}S_{\text{Fe}} \gamma_{\text{Fe}} + G_{\text{int}}$$

$$G_{\text{int}} = A [(0.33/2) (\gamma_{\text{AuFe}} + \gamma_{\text{Fe}})] + \{ [X_{\text{AuFe}} \Delta H_{\text{Au_in_Fe}} / [C_{\text{o}}(V_{\text{Au}})^{2/3} + X_{\text{Fe}} \Delta H_{\text{Fe_in_Au}} / [C_{\text{o}}(V_{\text{Fe}})^{2/3}]] \}$$

D – considered separately for D_{Au} and D_{Fe} (Figure S15)

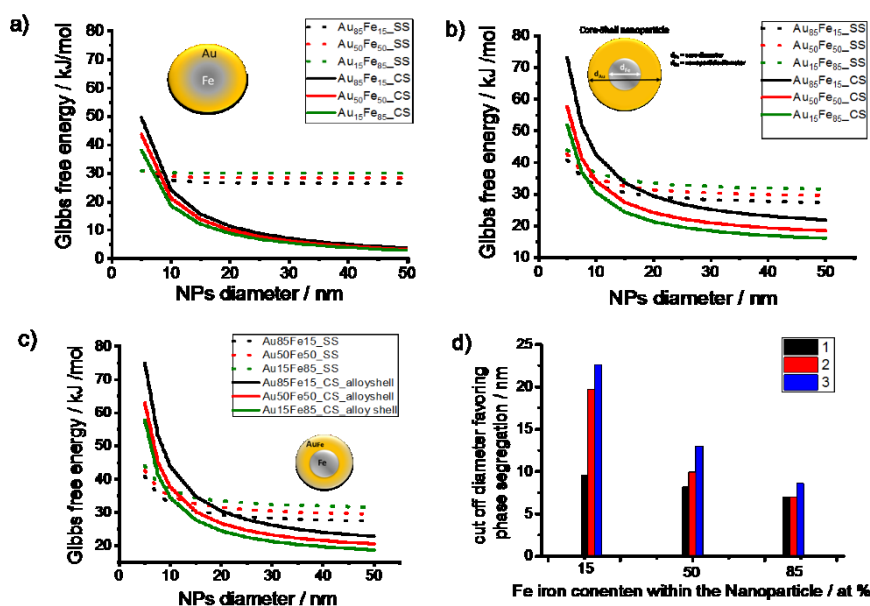


Figure S14: Theoretical calculations for SS and CS compositions for 3 representative Au₁₅Fe₈₅, Au₅₀Fe₅₀ and Au₈₅Fe₁₅ a) CS with pure iron core and gold shell according to method described elsewhere¹⁴¹ b) CS with pure iron and pure shell with modified equation as described in chapter SI 5 c) CS with pure iron and alloy shell d) Comparison of Cut off diameter favouring phase segregation for all 3 calculation methods, for CS with pure iron core and gold shell according to method described elsewhere (black bar), CS with pure iron and pure shell with modified equation as described in chapter SI 5 c (red bar) and CS with pure iron and alloy shell (blue).

Liquid environment influence on the NPs formation

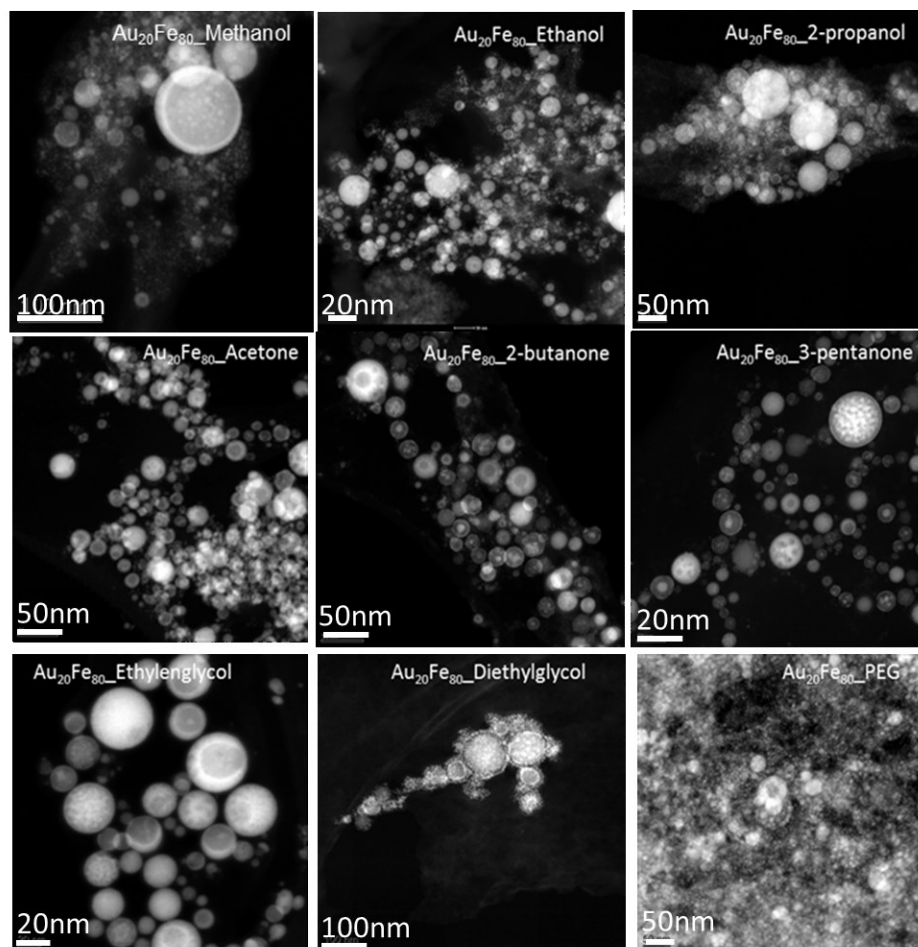


Figure S15: Representative STEM pictures for $\text{Au}_{20}\text{Fe}_{80}$ generated in various liquids: methanol, Ethanol, 2-propnal, Acetone, 2-butanone, 3-pentanone, Ethylene glycol, diethylene glycol, PEG and oil PAO40 via 8ns laser.

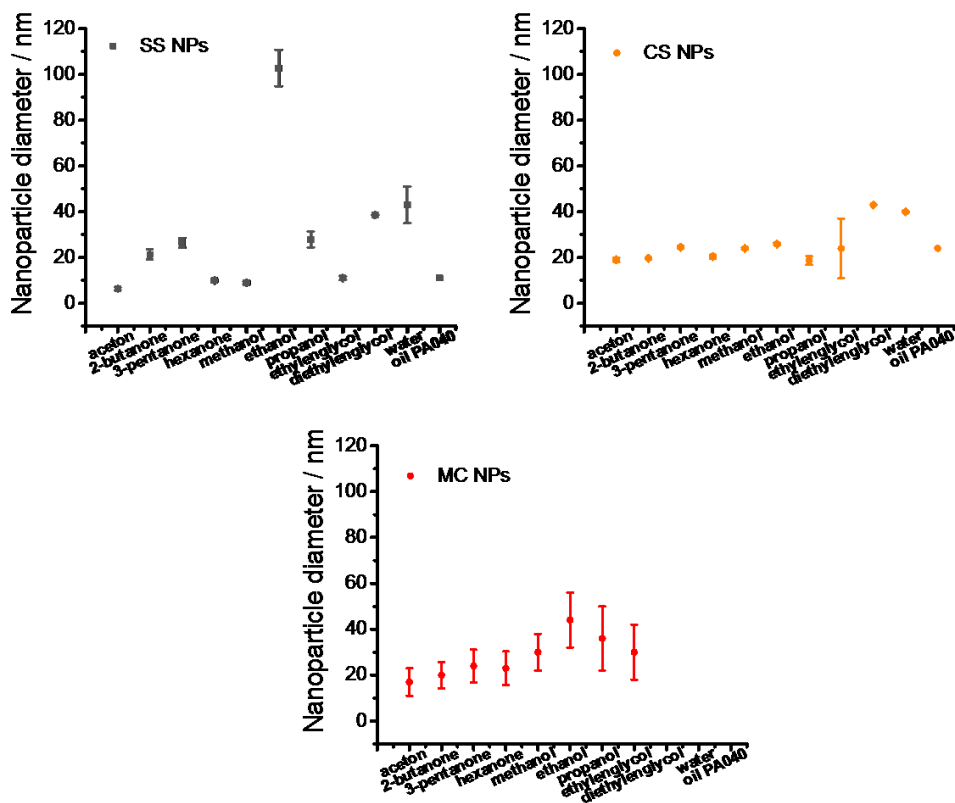


Figure S16: Number weighted median nanoparticle diameter for individual ultrastructure's solid solution, Core-Shell and Multi-Core-Shell for 3 representative types of liquids: ketones, alcohols and glycols (with additional highly viscous liquid PAO40 oil).

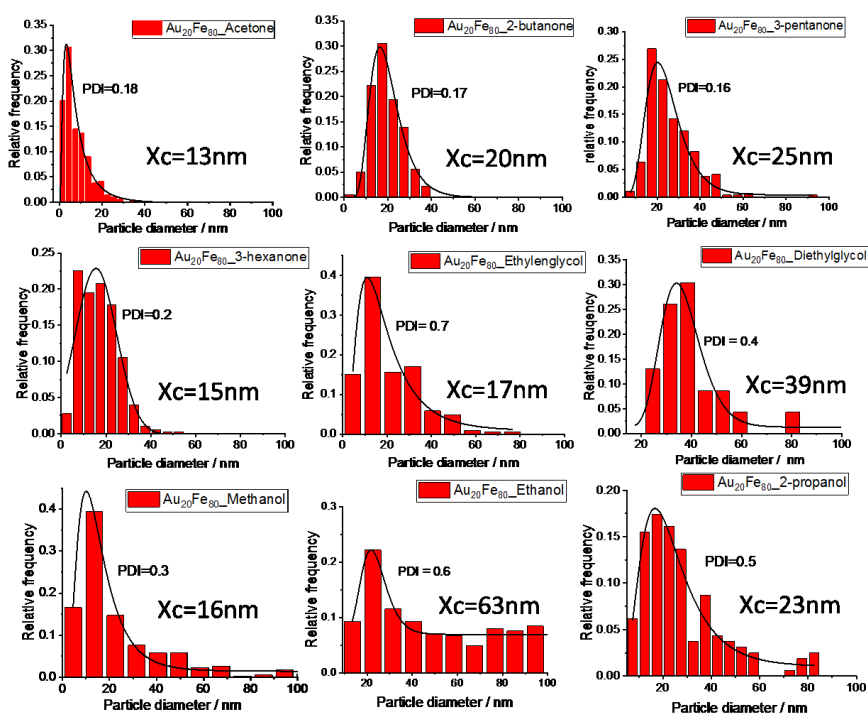


Figure S17: Number weighted size distribution for ketones, alcohols and glycols. The mean diameter is calculated by fitting the distribution with a log-normal function

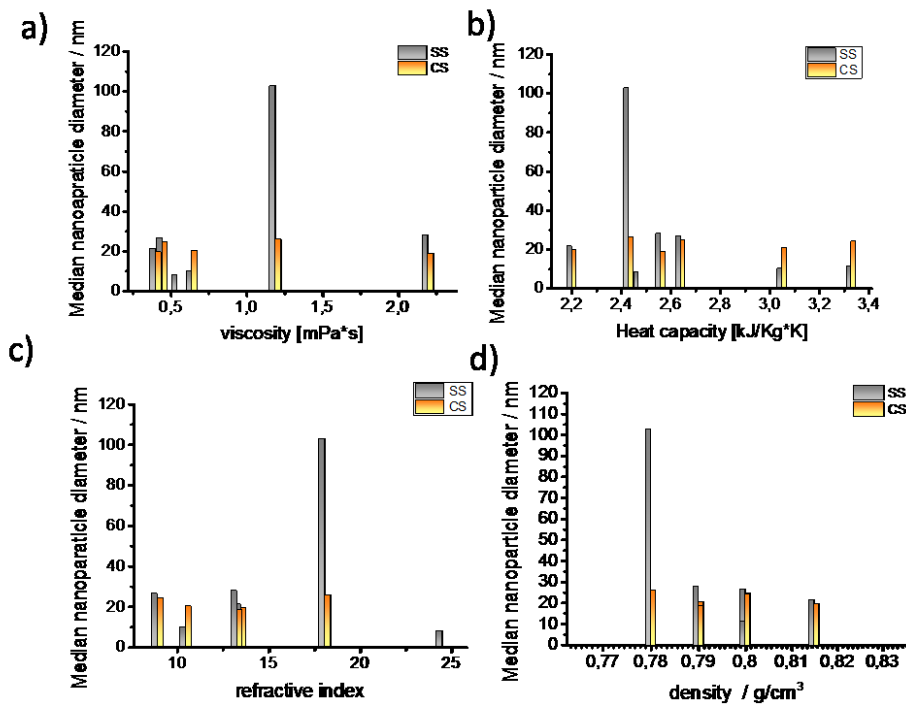


Figure S18: Overview of parameters influencing the AuFe diameter, namely a) viscosity b) heat capacity c) refractive index and d) density for Au₂₀Fe₈₀ configuration generated via 8 ns with LAL.

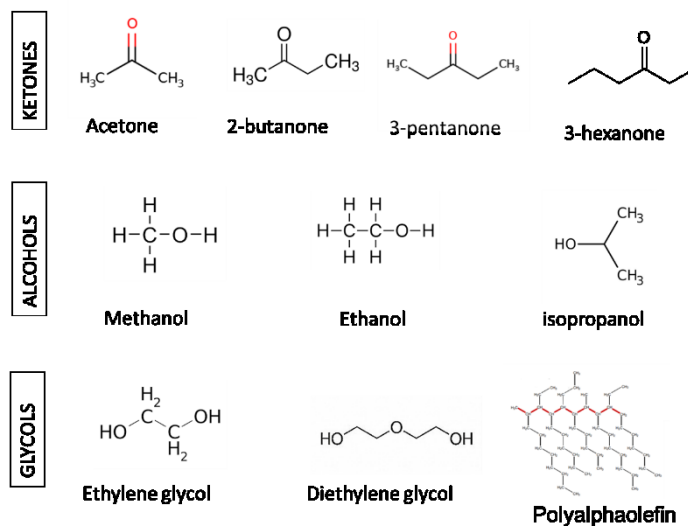


Figure S19: Schematic overview of chemical structures for the liquid used in the chapter 4.2.2.

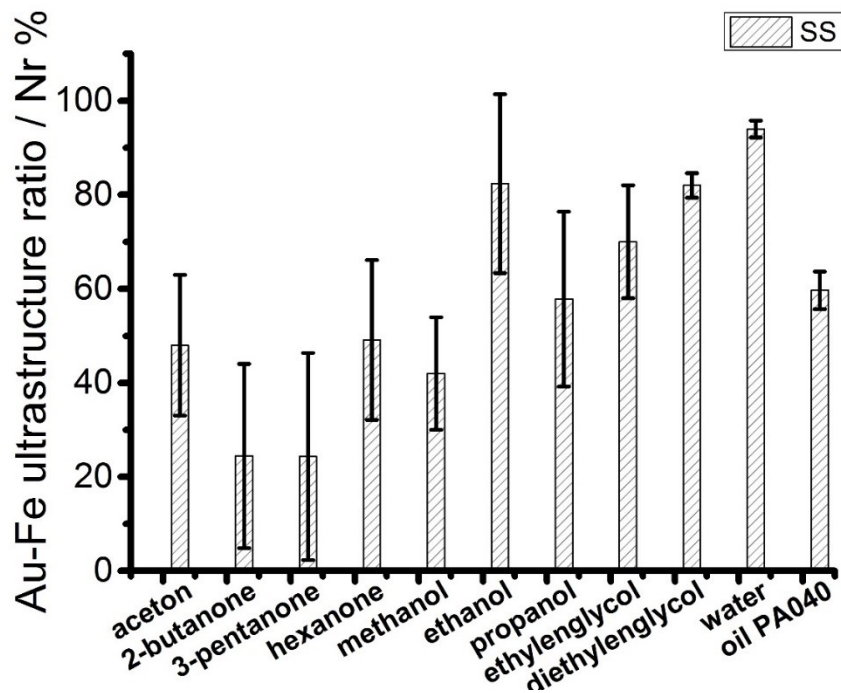
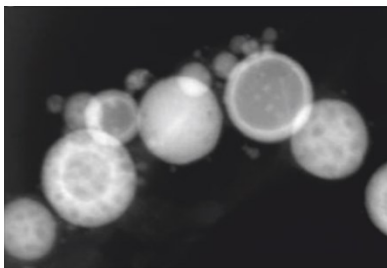
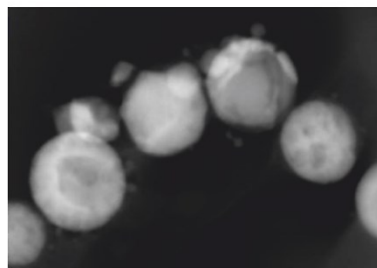


Figure S20: Yield of solid solution number weighted for for 3 representative types of liquids: ketones, alcohols and glycols (with additional highly viscous liquid PAO40 oil).

250°C



550°C



700°C



Figure S21: Morphology changes for $\text{Au}_{20}\text{Fe}_{80}$ sample with representative Z-contrast images recorded during in situ heating for selected temperatures; 250°C, 550°C and 700°C.

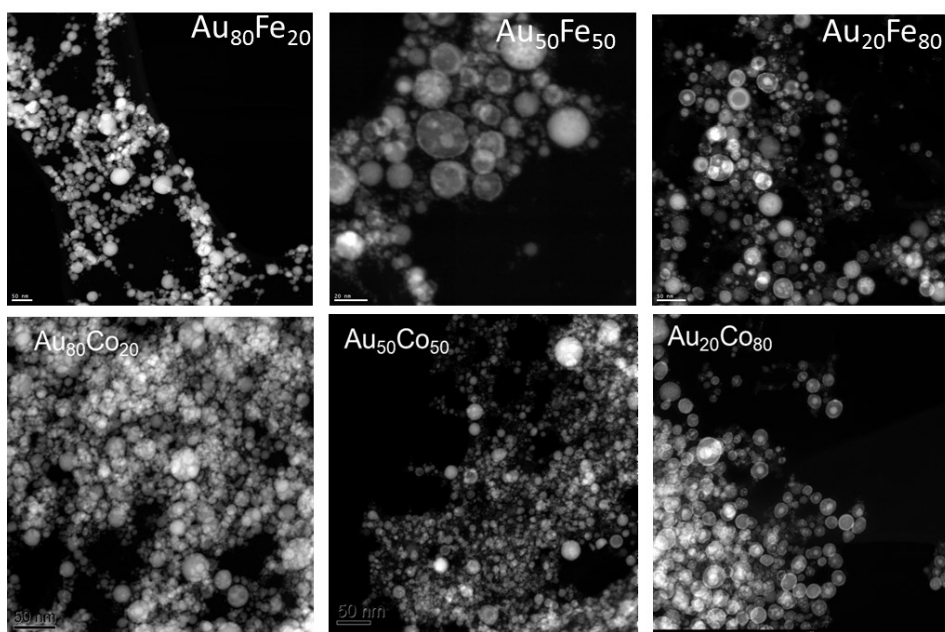


Figure S22: Representative STEM pictures for AuCo and AuFe for 3 compositions: 20:80; 50:50: and 80:20, all samples were generated in Acetone via 8 ns laser.

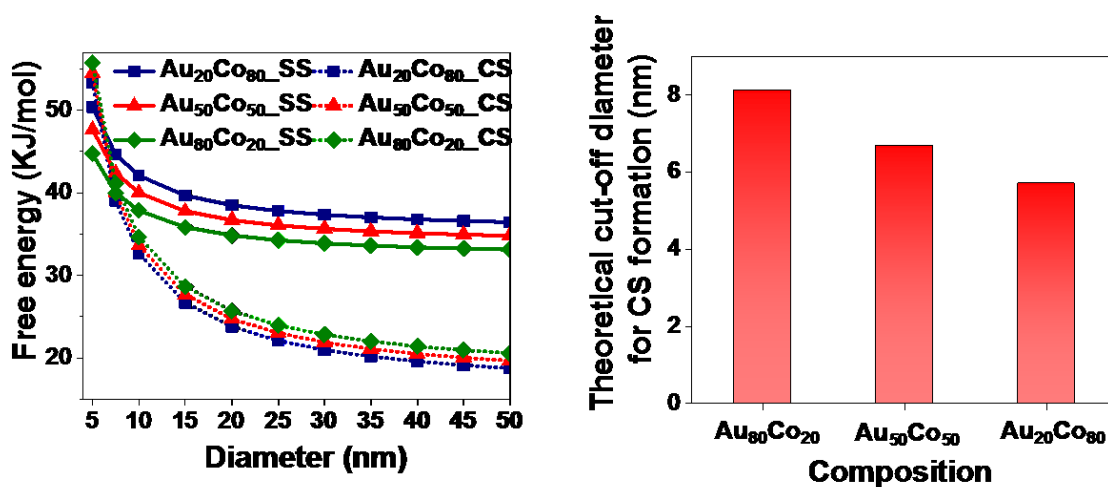


Figure S23: Theoretical calculation for AuCo as described in chapter S5 with distinction of cut off diameter for Core-Shell nanoparticle formation.

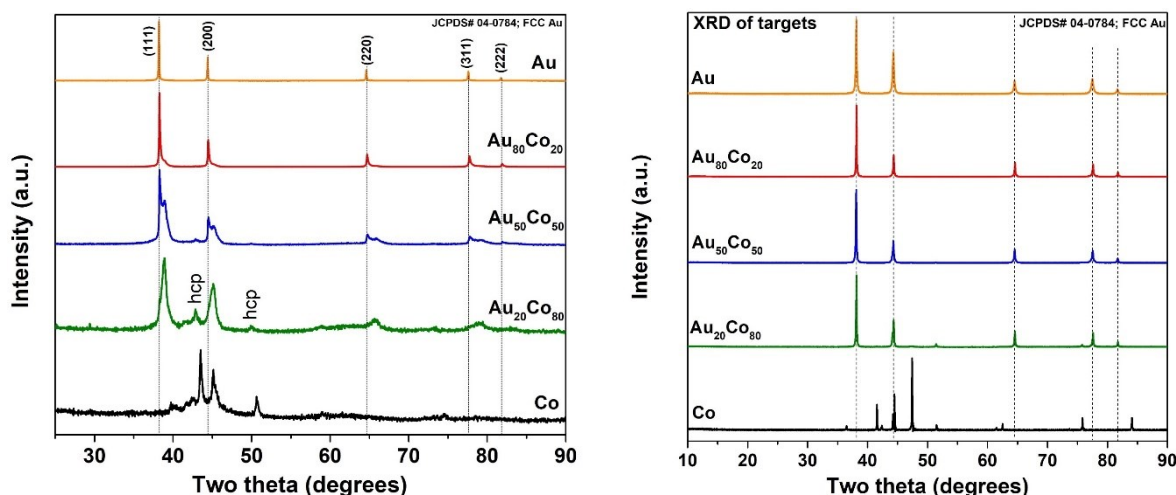


Figure S24: XRD analysis of crystal phase for AuCo with a) XRD patterns of Au, Au₈₀Co₂₀, Au₅₀Co₅₀ and Au₂₀Co₈₀ and Co NPs generated by PLAL showing two FCC structure for the bi-metallic NPs b) XRD patterns of Au, Au₈₀Co₂₀, Au₅₀Co₅₀ and Au₂₀Co₈₀ and Co targets used for laser ablation showing a structure close to FCC-Au for the bi-metallic targets

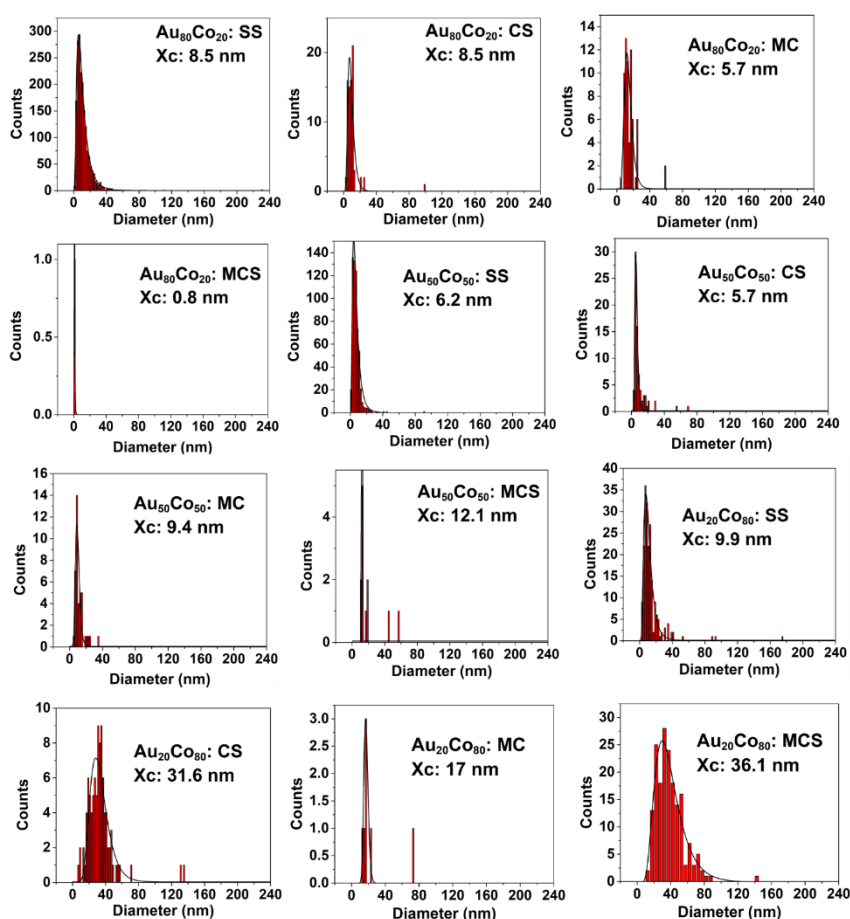


Figure S25: Particle statistics for solid solution (SS), core-shell (CS), multi core-shell (MCS) and multi core (MC) structures for Au₈₀Co₂₀, Au₅₀Co₅₀ and Au₂₀Co₈₀ compositions generated by LAL. The mean diameter is calculated by fitting the distribution with a log-normal function

7.3 Material and Methods

7.3.1 Nanoparticles synthesis and characterization

AuCo target preparation

3 different compositions of gold cobalt targets ($\text{Au}_{20}\text{Co}_{80}$, $\text{Au}_{50}\text{Co}_{50}$ and $\text{Au}_{80}\text{Co}_{20}$) were prepared by pressing micro powders of Au (Chempur, 0.3-3 micron, 99.9+%) and Co (Chempur, 2-4 micron, 99.5%) using a hydraulic press. To obtain homogenous mixture respective ratios were in a mortar. Au foil targets was used to generated Au nanoparticles, whereas Co NPs were synthesized from the powder. Two hours sinteration at 800°C of pressed targets occurred under the presence of a reductive atmosphere (95% N_2 ; 5% H_2) to avoid Co oxidation. After sinteration process, all targets were polished with help of sand paper to remove any surface contaminations.

AuFe targets

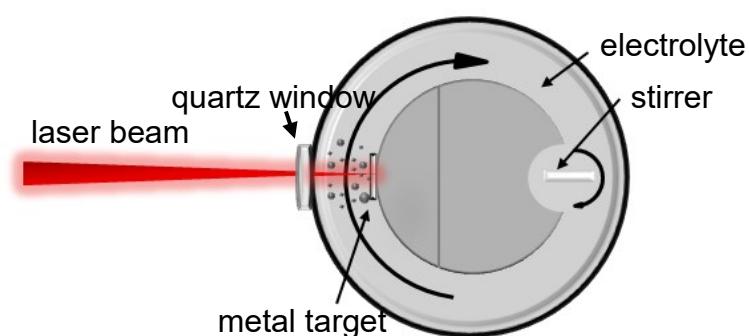
Au-Fe bulk alloy targets with different Au:Fe atomic % ratio (10:90,20:80,50:50,81.5:18.5 and 90:10) were bought from fem Institut für Edelmetalle und Metallchemie, Schwäbisch Gmünd company.

7.3.2 Pulsed laser ablation in liquids (LAL)

For all studies Au-Fe alloy targets (fem Institut für Edelmetalle und Metallchemie, Schwäbisch Gmünd) with different Au:Fe atomic % ratio (10:90,20:80,50:50,81.5:18.5 and 90:10) were ablated in Acetone 99,8% (from Carl-Roth GmbH, Karlsruhe). LAL was performed with 10 ns Nd:YAG laser (Rofin Sinar Technologies, Plymouth) at 1064nm with a repetition rate of 15kHz and a fluence 3.85mJ/cm². A lens with a focal length of 100mm was used to focus the beam through a glass window into a batch reactor containing the Au-Fe alloy target emerged in 30ml acetone. The alloy target was placed vertically to the bottom of the batch-chamber. Additionally, an electrical motor was mounted at the back of the chamber to assure a constant flow of the ablated material, avoiding absorption of the laser energy from already generated NPs. The

amount of ablated mass was determined gravimetrically by weighting the target before and after laser ablation using a microbalance.

Parameter [unit]	ps-laser	ns-laser
Power [W]	15.6	5.5
Pulse energy [mJ]	0.156	0.36
Wavelength [nm]	1064	1064
Spiral diameter [mm]	6	6
Repetition rate [kHz]	100	15
Focal length [mm]	100.1	100
Distance (f lens to target) [cm]	12	12
Fluence [$J\ cm^{-2}$]	3.12	3.78



Threshold fluence for Au $0,6\ J/cm^2$ (ps)

Threshold fluence for Fe $1,15\ J/cm^2$ (ps) $1,3\ J/cm^2$ (ns?)

7.3.3 Single pulse laser ablation

Six different targets were ablated in 2 ml Acetone (HiperSolChroma) and 2 ml water (Mili). AuFe multilayers on glass films were prepared by Prof. Cattaruzza.

Description of Au-Fe films on glass (4 sets packaged under vacuum): # 363: Au/Fe/glass, total thickness ca. 80 nm, relative thickness Fe/Au=1.10, # 364: Au/Fe/Au/Fe/glass, total thickness ca. 80 nm, relative thickness Fe/Au=1.13, # 365: Fe/Au/glass, total thickness ca. 80 nm, relative thickness Fe/Au=1.03, # 366: Au+Fe/glass (AuFe alloy on glass), total thickness ca. 80 nm, relative thickness Fe/Au=0.90, # 367: Au/glass, total thickness ca. 100 nm, # 369: Fe/glass, total thickness ca. 70 nm.

New material was ablated for each pulse to avoid target modification and melting. Laser parameters are as follow: 10 ps laser Pulse energy 0.156 mJ, Repetition rate 100kHz and Fluence 1,8J/cm². Experiments were performed at Duisburg Essen University in Germany. Ablation using 10 ns laser was performed at Padova University in Italy. Laser parameters are as follow Pulse energy (22.6 mJ/pulse, 10ns, 1064nm)

7.3.4 UV-Vis Spectroscopy (UV-Vis)

UV/Vis extinction spectroscopy is a spectroscopic technique in which a sample is irradiated with light of different wavelengths in the ultraviolet-visible spectral region. A Specific absorbance is an result of the induced electronic transitions. For this the transmitted light is detected in correlation to the incident light. To the set up of Spectrophotometer belong a sample holder, a light source, a monochromator and a detector. Based on the Beer-Lambert Law, the absorbance of a solution is in direct correlation to the concentration of the absorbing species and the path length. Therefore, this method can be used as tool to quantify absorbing species.

Quartzcuvette with d=10 mm were used for all measrments. UV-Vis Spectrum were analyse between 200-1000 nm. To avoid agglomeration each AuFe colloid were placed for 10 min in ultrasonic bath before each measurment.

7.3.5 High-angle annular dark-field scanning transmission electron microscopy (STEM-HAADF) and EDX analysis

Analysis with help of STEM has similar properties to detection via TEM, The difference lies in the electron beam, which scans the sample in a raster, whereas the electron beam is focused on a small spot. TEM, enables the direct imaging with a high-voltage, focuses electron-beam. While the electron beam passes through the sample, electrons are diffracted by atomic planes of the sample. This results in formation of the transmission electron diffraction patterns, then magnified image is created. The image contrast is determined by the thickness of the sample and the material-dependent absorption of electrons. Similarly to TEM, STEM uses the different ways of the interaction of the electron beam with the species in aim to create an image. Here the spot size cant exceed 1 nm, and therefore for this purpose Field Emission Gun is used. The biggest advantage of the STEM is the possibility of application of different imaging modes at once, which is not accessible during TEM measurements.

High Resolution Transmission Electron Microscopy, is an additional imaging mode, which allows the creation of higher resolution images (of 0.1 nm). The principle is based on the fact, that phase contrast is used and not the analysis of the difference in the intensity resulted due to absorption of the sample, used in bright field mode. The phase contrast, on the other side, evaluates the phase shifts of the electron waves. The electron wave interacts with the positive core of an atom leading to the phase shift. As a result an image with the plane of the electron waves interface is generated. This approach has many advantages towards crystalline material analysis.

Both of this approaches are enriched by the elemental analysis with Energy dispersive X-Ray spectroscopy. In this method, the high energy electron beam is focused on the sample, leading to removal of the electrons from the core shells into ionize atoms of the sample. An electron from the upper shell will take place its former position after the inner shell electron is removed. The electron from the upper shell is characteristic with the higher energy than the electron in the inner shell. The EDX detector measures the difference of the energy between both of them will be released as X-Rays. According to Pauli principle each element has a specific X-Rays and therefore it can be characterized. Finally the elemental structure of the analyzed sample can be established.

Size and the internal composition were determined using transmission electron microscopy STEM-HAADF (FEI Company, Tecnai F30, STWIN G). 10 μ L of the colloid dispersion were pipetted onto a carbon-coated copper microgrid and dried overnight. The ferret diameter was measured with the aid of a measuring tool in Digital micrograph by averaging 1000 nanoparticles. The results were plotted both as number and volume-weighted distribution and fitted using a log-normal function. The average particle size was obtained from the expected values X_c of this fit. Energy dispersive x-ray spectroscopy is a suitable method for quantitative elemental detection of iron gold system. Thus differentiation of the elements and corresponding oxide is distinct. EDX results are obtained by STEM-EDX measurements with Phillips XL 30 with EDAX DX-4. Therefore, different kind of EDX spectra are generated. The integration over a large number of nanoparticles confirms the coincidence of target and nanoparticle composition. Based on Z-contrast of STEM-HAADF imaging mode, a distinct hint of the ultrastructure is possible. CS nanoparticles can be identified, but EDX mapping and line scans are sufficient to prove the existence of the CS ultrastructure in each

sample. Furthermore, the absence of oxidation especially in the iron core of Fe@Au nanoparticles can be proved.

7.3.6 Selected area diffraction (SEAD)

SEAD is powerful technique, frequently used to study crystal structure of materials. The sample is irradiated with an electron beam by an incident parallel beam. A diffraction pattern appearing, contains electrons from the whole range of the illuminated area. A first diffraction pattern appears in the focal plane of the objective lens, whereas the image is show in the plane of this lens. Thank to magnification lens intermediate image or the diffraction pattern is generated.

7.3.7 X-Ray Diffraction (XRD)

By means of X-ray powder diffraction (XRD) using a Bruker D8 Advance diffractometer (Cu K α radiation, $\lambda = 1.54 \text{ \AA}$; 40 kV, 40 mA) a phase composition of all targets and produced FeAu NPs was determined. Comparing to the bulk materials just positioned in sample holder, all nanoparticles from a high-concentrated colloid were homogenously distributed on a silicon single crystal to minimize scattering. To determine the phase ratios, lattice parameters and percentage of the Fe/Au substitution in the FCC and BCC structures as well as to estimate AuFe. The average crystallite sizes from diffraction peak broadening reflections (using the Scherrer equation), the Rietveld refinement was performed with the Bruker software TOPAS 4.2. The patterns of cubic Au-FCC (#004-0784) and Fe-BCC (#006-0696) phases from the ICDD database were used as reference for the qualitative phase analysis, which was done with a Diffrac.Suite EVA V1.2 from Bruker.

7.4 Curriculum Vitae

Der Lebenslauf ist in der Online-Version aus Gründen des Datenschutzes nicht enthalten.

7.5 List of Authored and Co-author Publications

Peer-Reviewed Publications

1.) Anna Tymoczko, Marius Kamp, Oleg Prymak, Christoph Rehbock, Jurij Jakobi, Ulrich Schürmann, Lorenz Kienle and Stephan Barcikowski. How the crystal structure and phase segregation of Au–Fe alloy nanoparticles are ruled by the molar fraction and size. **Nanoscale**, 2018,**10**, 16434-16437

2.) Anna Tymoczko, Marius Kamp, Christoph Rehbock, Lorenz Kienle, Elti Cattaruzza, Stephan Barcikowski and Vincenzo Amendola. One-step synthesis of Fe–Au core–shell magnetic-plasmonic nanoparticles driven by interface energy minimization. **Nanoscale Horiz.**, 2019,**4**, 1326-1332

3.) Marius Kamp, Anna Tymoczko, Ulrich Schürmann, Jurij Jakobi, Christoph Rehbock Klaus Rätzke, Stephan Barcikowski, Lorenz Kienle. Temperature-Dependent Ultrastructure Transformation of Au–Fe Nanoparticles Investigated by in Situ Scanning Transmission Electron Microscopy. *Cryst. Growth Des.* 2018, 18, 9, 5434-5440.

4.) Marius Kamp, Anna Tymoczko, Ulrich Schürmann, Jurij Jakobi, Christoph Rehbock Klaus Rätzke, Stephan Barcikowski, Lorenz Kienle. Temperature-Dependent Ultrastructure Transformation of Au–Fe Nanoparticles Investigated by in Situ Scanning Transmission Electron Microscopy. *Cryst. Growth Des.* 2018, 18, 9, 5434-5440.

Oral presentation (presenting author*)

1.) Anna Tymoczko, Marius Kamp, Christoph Rehbock, Lorenz Kienle, Stephan Barcikowski Laser generated magneto-plasmonic Au-Fe Nanoparticles: Formation mechanism, Real Structure and properties, 6th EuCheMS Chemistry Congress, September 2016, Seville (Spain).

2.) Anna Tymoczko, Marius Kamp, Oleg Prymak, Christoph Rehbock, Jurij Jakobi, Ulrich Schürmann, Lorenz Kienle and Stephan Barcikowski Modeling the formation mechanism for magneto-plasmonic Au@Fe NPs generated via laser ablation. 7. Junges Chemie Symposium Ruhr, October 2016, Dortmund.

3.) A. Tymoczko, M. Kamp, C. Rehbock, J. Jakobi, U. Schürmann, S. Barcikowski, L. Kienlei. The formation mechanism and internal phase structure of AuFe alloy

nanoparticle generated via laser ablation in liquids. XXVI International Materials Research Congress (IMRC August 2017) in Cancun, Mexico.

4.) Anna Tymoczko*, Marius Kamp, Christoph Rehbock, Ulrich Schürmann, Oleg Prymak, Lorenz Kienle, Stephan Barcikowski. How does the crystal structure influence the final composition of the Au-Fe alloy nanoparticles generated via pulsed laser ablation in liquids? 26th Annual Meeting of the German Crystallographic Society (DGK) March 2018, Essen.

5.) Anna Tymoczko*, Marius Kamp, Christoph Rehbock, Ulrich Schürmann, Oleg Prymak, Lorenz Kienle, Stephan Barcikowski High yield one step laser synthesis of core-shell Fe-Au nanoparticles is influenced by target composition and nanoparticle size. The 2019 Spring Meeting of the European Materials Research Society, May 2019, in Nice, France

Poster Presentation

1.) Anna Tymoczko, Marius Kamp, Oleg Prymak, Christoph Rehbock, Jurij Jakobi, Ulrich Schürmann, Lorenz Kienle and Stephan Barcikowski. Formation mechanism of AuFe nanoparticles via laser ablation. CENIDE, NanoBioPhotonics-Symposium, 2016, Duisburg

2.) Anna Tymoczko, Marius Kamp, Oleg Prymak, Christoph Rehbock, Jurij Jakobi, Ulrich Schürmann, Lorenz Kienle and Stephan Barcikowski. Understanding the formation mechanism of magneto-plasmonic Au-Fe Nanoparticles (NPs) generated by pulse laser ablation in liquid (PLAL). 7. NRW Nano-Konferenz - NMWP, December 2016, Münster

3.) Anna Tymoczko, Marius Kamp, Oleg Prymak, Christoph Rehbock, Jurij Jakobi, Ulrich Schürmann, Lorenz Kienle and Stephan Barcikowski. How does the crystal structure influence the final composition of the Au-Fe alloy nanoparticles generated via pulsed laser ablation in liquids? 26th Annual Meeting of the German Crystallographic Society (DGK) March 2018, Essen.

7.6 Declarations

Experimental contribution:

- 1.) STEM, TEM, EDX line scans / mapping and SEAD patterns experiments and data interpretation (chapter 4.3), size distribution statistics (chapter 4.2.2) were carried out by Marius Kamp, Faculty of Engineering, CAU Kiel
- 2.) X-Ray powder diffraction (XRD) for AuFe and AuCo was executed by Dr. Oleg Prymak, Institute of Inorganic Chemistry, UDE Essen,
- 3.) Single pulse laser ablation with 10 ns laser, SERS, Raman Spectra was carried out by Dr. Vincenzo Amendola, Dep. of Chemical Sciences 1, University of Padova
- 4.) Laser ablation of AuFe in various liquids was performed by Roger Aumuller, UDE, Essen
- 5.) Laser ablation of AuCo was conducted by Dr. Jacob Johny, UDE, Essen

Publication contribution:

Results on the target composition and size of the particles impact on the Core-Shell Yield have been published in the scientific journal *Nanoscale*:

*Anna Tymoczko, Marius Kamp, Oleg Prymak, Christoph Rehbock, Jurij Jakobi, Ulrich Schürmann, Lorenz Kienle and Stephan Barcikowski. How the crystal structure and phase segregation of Au–Fe alloy nanoparticles are ruled by the molar fraction and size. *Nanoscale*, 2018,10, 16434-16437*

The authors gave the following contributions: The experimental design was given by SB, AT and CR. Experiments were conducted by AT, MK and OP. Data analysis and interpretation were performed by AT, CR, MK, US, OP, JJ, LK and SB. The first draft was written by AT under the guidance of SB. All authors revised the manuscript.

Results on the target geometry and pulse duration of the particles impact on the Core-Shell Yield have been published in the scientific journal *Nanoscale Horizons*:

*Anna Tymoczko, Marius Kamp, Christoph Rehbock, Lorenz Kienle, Elti Cattaruzza, Stephan Barcikowski and Vincenzo Amendola. One-step synthesis of Fe–Au core–shell magnetic-plasmonic nanoparticles driven by interface energy minimization. *Nanoscale Horiz.*, 2019,4, 1326-1332*

The authors gave the following contributions: The experimental design was given by SB, AT, CR and VA. Experiments were conducted by AT, MK, EC and VA. Data analysis and interpretation were performed by AT, CR, MK, VA, EC, LK and SB. The first draft was written by AT under the guidance of VA and SB. All authors revised the manuscript.

Results on the temperature on the particles ultrastructure have been published in the scientific journal Nanoscale Horizons:

Marius Kamp, Anna Tymoczko, Ulrich Schürmann, Jurij Jakobi, Christoph Rehbock, Klaus Rätzke, Stephan Barcikowski, Lorenz Kienle. Temperature-Dependent Ultrastructure Transformation of Au–Fe Nanoparticles Investigated by in Situ Scanning Transmission Electron Microscopy. Cryst. Growth Des. 2018, 18, 9, 5434-5440.

The authors gave the following contributions: The experimental design was given by MK, US and LK. Experiments were conducted by AT, KR and MK. Data analysis and interpretation were performed by AT, CR, MK, US, KR, JJ, LK and SB. The first draft was written by MK under the guidance of LK. All authors revised the manuscript.

Results on the etching on the particles ultrastructure stability have been published in the scientific journal Nanoscale Horizons:

Marius Kamp, Anna Tymoczko, Ulrich Schürmann, Jurij Jakobi, Christoph Rehbock Stephan Barcikowski, Lorenz Kienle. Templated dealloying: designing novel ultrastructures by memory effect. Cryst. Growth Des. 2019, 19, 9, 4957-4963.

The authors gave the following contributions: The experimental design was given by MK, US and LK. Experiments were conducted by AT and MK. Data analysis and interpretation were performed by AT, CR, MK, US, JJ, LK and SB. The first draft was written by MK under the guidance of LK. All authors revised the manuscript.

The following student works have been completed under my co-supervision:

Laura Theimann, Master Thesis, Lehramt, October 2016-Mai 2017: "Aufarbeitung von Fe@Au-Nanopartikeln und deren Charakterisierung mittels Cyclovoltammetrie"

Roger Aumüller, Bachelor Thesis, March 2017- June 2017 "Auswirkungen von Lösemittel auf die Kern-Schale-Strukturen von Gold-/Eisennanopartikel."

Jarno Banas, Analytic Practical, Study of laser generated Fe@Au core-shell nanoparticles via Cyclic Voltammetry.

Johny Jacob, Guest Researcher, September 2018-March 2019 "Evaluation of the mechanistic AuFe model with another binary system, AuCo"

I hereby state that I have not received the opportunity to take part in the present doctoral proceedings via commercial channels. In particular, I have not engaged the services of any organization which will, for a fee, recruit supervisors for the process of preparing doctoral dissertations. Nor have I engaged the services of any such organization to carry out, either totally or in part, the tasks which I am obliged to perform as part of the examination requirements. I have received assistance, and will in the future receive assistance, from third parties only to an extent which is commensurate with good scholarly practice and permitted by the laws on examinations.

I am aware that making any false declarations in this statement can cause me to be excluded from the doctoral proceedings or, at a later date, result in termination of the proceedings or revocation of an already awarded doctoral title.

7.7 Acknowledgment

I would like to thank my PhD supervisor Prof. Dr.-Ing. Stephan Barcikowski for providing me this interesting and challenging research topic, the very good scientific supervision with many stimulating discussions and the seemingly unlimited number of ideas. I would also like to thank him for making it possible for me to attend numerous conferences to present many of our research results. But I would also like to thank for the numerous activities besides working hours, which have created a phenomenal working atmosphere in the TCI group.

I would like to thank Prof. Dr. Lorenz Kienle for helpful tips and discussions, and for enabling a successful cooperation with his research group.

In addition to the thanks to both professors, my sincere thanks go to Dr. Christoph Rehbock for his constant readiness for discussions and his extraordinary motivation to achieve the project goals. Many thanks for the numerous fruitful discussions and meetings.

I would like to thank Dr. Vincenzo Amendola for his willingness to conduct single pulse experiments and for stimulating discussions during our collaboration.

I would like to thank Marius Kamp for the pleasant cooperation and his support. In particular, I thank him for the nanoparticle characterization with electron microscopy methods and his refreshing ideas during project meetings.

I thank my hard-working students Laura Theimann, Roger Aumuller, Jarno Banas for their productive cooperation. Especially many thanks to Dr. Jacob Johnny, for many interesting discussions during his stay in Germany.

For the constant support and the many advices, the great working atmosphere and the wonderful time, I would like to thank all employees of TC I: Carmen, Sebastian, René, Jurij, Alex H., Alex L., Anna Z., Bilal, Christoph, Claudine, Dieter, Elisabeth, Frank, Friedrich, Galina, Ina, Lisa, Marcus, Mark, Nina, Philipp, Stephan, Sven K., Sven R. and Tim. Especially, Sandra, Ruksan and Jacob for very memorable moments, support, motivation and friendship.

Special appreciation for my husband Christian, for his support, motivation and his patience.

Last but not least, I would like to thank my family, and my brother, people who were always there for me and made me the person I am today. In this way I would like to thank them for the beautiful childhood and youth, in which you taught me the most important values.